NTNU
Norwegian University of
Science and Technology

Influence of impurity elements on the precipitation behaviour of dispersoids and their hardening effects in aluminium alloys

Marit Onsøien

Materials Science and Engineering
Submission date: June 2017
Supervisor: Yanjun Li, IMA

Norwegian University of Science and Technology
Department of Materials Science and Engineering

Preface

This work is the conclusion to five great years of studying at the Norwegian University of Science and Technology. The objective of the thesis was to study the influence of impurity elements on the precipitation behaviour of several aluminium alloys. This has been done by experimental work carried out at the Institute of Materials Science, with great help from the technical staff, whom I wish to thank very much. I would also like to express my gratitude towards my supervisor Professor Yanjun Li and Dr Feng Qian for their invaluable help and guidance throughout the project work, both with fruitful discussions and help carrying out experiments. At last, I would like to thank Magnus A. Krokstad for his patience, proofreading and feedback.

Trondheim, June 2016.

Marit Eline Onsøien

Abstract

The hardness of five Al-Zr(-Cd) alloys with varying levels of alloying elements were investigated during heat treatment. Two of these, the Al-0.23Zr and Al-0.26Zr-0.29Cd alloys, were also examined with a TEM and tensile strength measurements. When examining samples at the peak hardness achieved at 400 ℃ - 550 ℃, it was found that additions of Cd to an Al-Zr alloy both enhances the volume fraction of precipitates, and accelerates the precipitation kinetics. If a faster heat treatment is chosen, additions of Cd are also very beneficial to the yield strength, but when using the most efficient heat treatment, no clear strengthening effect is seen. Additions of Cd allows the Al-Zr alloys to have another, lower peak in hardness at 200 ℃. The precipitates at this temperatures also seem to be more effective at strengthening the Al-Zr-Cd alloys, as this is the temperature at which both maximum YS and UTS have been achieved.

AA3003-Mo-Cd and AA3003-Mo-Cd-Cr alloys were heat treated and compared to the base alloy, as well as an AA3003-Cd alloy. The heat treatment used was continuous heating with a rate of 50 ℃/h up to 600 ℃ for all alloys, as well as an isothermal treatment of the Cr-containing alloy. α-Al(Mn,Fe,Mo)Si dispersoids starts precipitating after 300 ℃, growing from five nm to almost 80 nm at 600 ℃, and reach maximum hardness contribution at 450 ℃. Cd-additions creates an additional hardness peak at roughly 200 ℃ due to a fine dispersion of Cd particles. Additions of Mo gave a significantly increased hardness compared to both the base alloy and the Cd-containing alloy. Cr increases the hardness up to 400 ℃, but seems to decrease it above this. The highest yield strength in the AA3003-Mo-Cd alloy was reached at 450 ℃, meaning that the strength contribution from the dispersoids is greater than that of the Cd-precipitates at 200 ℃ which is in line with the hardness results.

An AA7050 alloy with and without addition of 0.28% Cd was hardened. Both a one-step hardening at 120 ℃ and a two-step hardening at 120 ℃ and 165 ℃ were tried. The results from these experiments showed that the addition of Cd failed in hardening the alloy additionally, no further investigations were performed.

Sammendrag

Hardheten til fem Al-Zr(-Cd) legeringer med forskjellige mengder legeringselement har blitt undersøkt med hensyn på presipitatherding under varmebehandling. To av disse, Al-0.23Zr og Al-0.26Zr-0.29Cd, har også blitt undersøkt med TEM og strekkfasthetsmålinger. Ved å undersøke prøvene som hadde oppnådd maksimum hardhet ved 400 ℃ - 550 ℃, ble det funnet at tilsetning av Cd til en Al-Zr legering både øker volumfraksjonen av presipitater og akselererer utfellingskinetikken til presipitatene. Hvis en rask varmebehandling benyttes vil tilsetning av Cd være gunstig for flytegrensen. Dersom den mest effektive varmebehandlingen, som er tregere, benyttes, vil derimot ingen ekstra styrkeeffekt fra Cd observeres. En ekstra, lavere hardhetstopp er tilstede ved 200 ℃ i legeringene med Cd. Presipitatene som utfelles ved denne temperaturen ser ut til å være mer effektiv på å styrke Al-Zr-Cd legeringene, ettersom det er ved denne temperaturen maksimum flytegrense og strekkfasthet er funnet.

AA3003-Mo-Cd og AA3003-Mo-Cd-Cr legeringer har blitt varmebehandlet og sammenlignet med en ren AA3003 legering, og en AA3003-Cd legering. Alle ble varmet opp til 600 ℃ med 50 ℃/time, i tillegg ble en isoterm varmebehandling av AA3003-Mo-Cd-Cr legeringen gjennomført. α-Al(Mn,Fe,Mo)Si dispersoider begynner å presipitere etter 300 ℃. Disse vokser fra rundt fem nm til nesten 80 nm ved 600 ℃, og når maksimalt hardhetsbidrag ved 450 ℃. Tilsetning av Cd i en AA3003 legering gir en ekstra topp i hardhet ved 200 ℃, på grunn av en fin dispersjon av Cd-presipitater. Tilsetning av Mo gir en betydelig økt hardhet sammenlignet med både den rene AA3003 legeringen og AA3003-Cd legeringen. Cr øker hardheten i legeringen opp til 400 ℃, men på temperaturer over dette virker det som om Cr senker hardheten. Maks flytespenning i AA3003-Mo-Cd legeringen nås ved 450 ℃, som betyr at styrkebidraget fra dispersoidene er større enn fra Cd-presipitatene ved 200 ℃. Dette stemmer også med hardhetsresultatene.

En AA7050 legering med og uten tilsetning av 0.28% Cd ble varmebehandlet. En kontinuerlig varmebehandling på 120 ℃ og en to-stegs varmebehandling på 120 ℃ og 165 ℃ ble benyttet. Hardhetsresultatene fra disse eksperimentene viser at tilsetningen av Cd mislyktes i å herde materialet videre. Ingen videre undersøkelser ble gjort.

Contents

Abbreviations

Abbreviation	Meaning
at	Atomic
CCD	charge-coupled device
DC	Direct chilled
DP	Diffraction pattern
EC	Electrical conductivity
EDS	Energy-dispersive x-ray spectroscopy
EELS	Electron energy loss spectroscopy
GP-zone	Guinier Preston-zone
HV	Vickers hardness
ND	Number density
PFZ	Precipitate free one
ppi	Particles per inch
RT	Room temperature
SEM	Scanning electron microscope
SHT	Solid solution heat treatment
TEM	Transmission electron microscope
UTS	Ultimate tensile strength
wt	Weight
XRF	X-ray fluorescence
YS	Yield strength

Equations

Number	Equation	Name
(2.1)	$\sigma_p = \frac{MF}{b\lambda}$	
(2.2)	$\lambda = r(\frac{2\pi}{3f})^{1/2}$	
(2.3)	$f = ND * \frac{\frac{4}{3} * \pi * r^3}{1.38}$	
(2.4)	$F = 2\beta G b^2(\frac{r}{r_c})$	
(2.5)	$F = 2\beta G b^2$	
(2.6)	$\sigma_D = \frac{0.84MGb}{2\pi(1-\nu)^{1/2}\lambda} ln\frac{r}{b}$	Ashby-Orowan equation
(2.7)	$\frac{1}{\sigma} = 0.0267 + 0.032Fe_{SS} + 0.033Mn_{SS} + 0.0068Si_{SS}$	
(2.8)	$2dsin(\Theta) = n\lambda'$	Braggs law
(2.9)	$Rd = \lambda' L$	
(2.10)	$t = mfp * \ln(\frac{I}{I_0})$	
(2.11)	$ND = \frac{\#Precipitates}{A * (t + \bar{D})}$	

Symbols

Symbol	Meaning
σ_p	Strength contribution from precipitates with looping or cutting mechanisms
M	Taylor factor
F	The sum of interaction forces between dislocation and precipitate.
B	Burgers vector
λ	Mean particle spacing
R	Mean radius
F	Volume fraction
ND	Number density
β	Constant ~0.5
G	Shear modulus
r_c	Critical radius for cutting a precipitate
σ_D	Strength contribution from precipitates with only the cutting mechanism
ν	Poissons ratio
σ	Electrical conductivity
d	Distance between diffracting planes
Θ	The Bragg angle
N	Integer
mfp	Mean free path of electrons
R	The distance between diffraction spots
λ'	Electrons wavelength
L	The camera length
T	The thickness of the TEM thinfoil
I	Integral below complete EELS spectrum
I_0	Integral below zero-loss peak
A	Area with observed precipitates
$\overline{D}$	Mean diameter of the precipitates

Chapter 1: Introduction

The use of aluminium and other light metals is rapidly growing in the world today, because of its many advantages compared to steel, its biggest competitor. Aluminium has a much higher specific strength than steel, making it vital in aerospace and automotive industry, as well as making it an important structural material. This, combined with its good corrosion resistance, high formability and good electrical conductivity makes aluminium one of the most diverse and applicable materials there is. It is also an environmentally friendly metal, as its light weight means that less energy will be used during transport. With only 5% of the energy used to produce it is needed to recycle it, it is also very easy and economical to recycle. During the recycling process only 3% of the metal is lost, and about 75% of all produced Aluminium is still in use today (1).

Aluminium does, however, face some challenges. One of the most important ones is that it often loses its strength at elevated temperatures. Another is that not all alloys are hardenable, making them too soft for several applications. Some alloys also need additions of rare or expensive elements to achieve their desired properties. To overcome these challenges, research must be performed on new heat treatments and alloying elements. Cadmium has already been shown to improve precipitation hardening behaviour in Al-Cu alloys, and in this master thesis we want to see if additions of Cd and other impurity elements has a positive effect on the precipitation hardening behavior in certain Al-Zr, 3xxx and 7xxx alloys as well. This is done through three desired objectives.

Al-Zr alloys are promising with respect to developing a thermally stable Al-alloy that can be dispersoid strengthened, as additions of Zr effectively inhibits recrystallization in the material when exposed to heat. As Zr has a very low diffusivity, other elements with higher diffusivity should be added to enhance the nucleation of Al_3Zr precipitates and thereby the strength of the alloy. This has usually been done by adding Sc, but as Sc is extremely expensive, a lot of research has been done to find a substitute. The first objective of the thesis is to find out if additions of Cd can improve the strength in Al-Zr alloys by enhancing the precipitation of Al_3Zr precipitates.

The second objective is to study the precipitation of an AA3003 alloy with additions of Mo and Cd, and with additions of Mo, Cd and Cr. The AA3003 alloy is usually not heat treatable, but with these additions one is able to get strengthening dispersoids that are stable at elevated temperatures, due to the low diffusivity of Mo and Cr. The dispersoids will be investigated by SEM and TEM, and other properties of the alloys, such as hardness, electrical conductivity and strength, will be tested.

The third objective is to find out if the precipitation of age hardening precipitates in an AA7050 alloy can be enhanced by the addition of Cd to improve hardness and strength. This is one of the strongest aluminium alloys on the market, and by further strengthening it, new applications can be found in areas where high performance materials are demanded. Additions of Cd have been proven to be efficient at enhancing the precipitation hardening behaviour in Al-Cu alloys, and the same effect is hoped to be achieved in the AA7050 alloy, as it contains Cu.

Chapter 2: Literature review

2.1 Precipitation hardening

Precipitation hardening, or age hardening, is a heat treatment that produces an increase in yield strength in certain aluminium alloys through the formation of precipitates. To get the wanted effect the alloys must be malleable, which means that they can deform to a high degree under compressing stresses such as rolling or forging. The alloys contain solutes, and the solid solubility of these differs at different temperatures, which is taken advantage of in this heat treatment. The goal is to produce a dispersion of nano-sized particles, called precipitates, throughout the material. These usually grow along specific hkl lattice planes and restrict movement of dislocations and lattice defects, leading to a harder and stronger material. These precipitates will precipitate out coherently, meaning that the atomic planes of the precipitates will be related to, or even continuous with, the atomic planes of the matrix. If they are allowed to grow, they will, however, become incoherent with the structure of the matrix and less efficient at stopping dislocation movement(2-5). Figure 2.1 shows examples of coherent and incoherent precipitates.

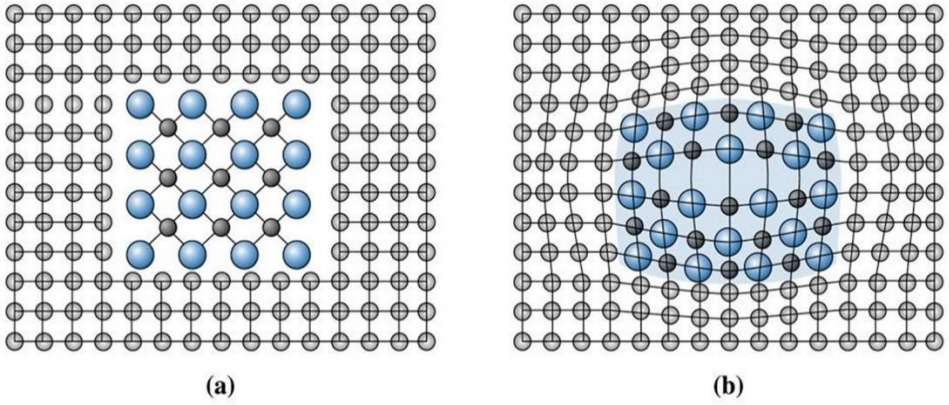

Figure 2.1: a) A precipitate that is incoherent. It has no relationship with the crystal structure of the matrix. b) A coherent precipitate with a clear relationship with the matrix. This figure is figure 12-8 from Askeland and Phulé (2)

.

There are two strengthening mechanisms for precipitation hardening. Either, the dislocations will have to cut through the precipitates, or they will bow around them, the latter being called Orowan strengthening or looping. Both mechanisms are illustrated in Figure 2.2. When the dislocation bows around the precipitate, it might encounter itself on the opposite side of the particle, forming a loop around it. When this happens, the dislocation will annihilate itself where it meets, causing the loop to separate from the original dislocation. If the precipitate is

small enough, the dislocation will cut through it instead of bowing around. The strain fields of the dislocation and precipitate will then interact and repulse each other, causing the dislocation to require additional energy for cutting through the precipitate (4, 5).

By assuming that the precipitates are spherical, the strength contributions from looping and cutting can be expressed by the following equation:

$$\sigma_p = \frac{MF}{b\lambda} \tag{2.1}$$

Where M is the Taylor factor, F is the sum of the mean interaction forces between the precipitates and dislocations, b is the burgers vector and λ is the mean particle spacing of the precipitates, which can be found from the following equation:

$$\lambda = r\left(\frac{2\pi}{3f}\right)^{1/2} \tag{2.2}$$

f is the volume fraction of the precipitates, and can be found by the following equation which utilizes the number density (ND), of which the equations are given in the TEM-section of the literature review:

$$f = ND * \frac{\frac{4}{3}*\pi*r^3}{1.38} \tag{2.3}$$

The interaction forces between the precipitates and dislocations will differ depending on which mechanism is followed. If the dislocation cuts through the precipitate, the interaction force F can be expressed as:

$$F = 2\beta G b^2\left(\frac{r}{r_c}\right) \tag{2.4}$$

Whereas if the dislocation bypasses the precipitate by looping, the mean interaction force can be assumed to be constant and independent of the particle size:

$$F = 2\beta G b^2 \tag{2.5}$$

In equation 2.2 and 2.3 β is a constant close to 0.5, G is the shear modulus of the aluminium matrix, r is the radius of the precipitate and r_c is the critical radius for cutting of a precipitate (4, 6, 7)

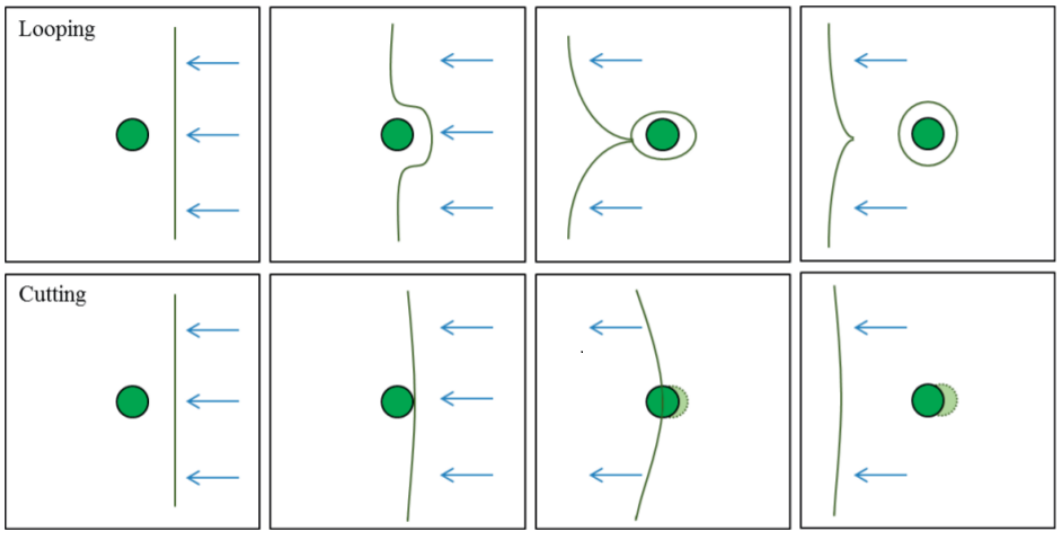

Figure 2.2: An illustration of dislocations bypassing a precipitate by either Looping or Cutting. Figure 2.5 from E. A. Mørtsell (4).

The cutting mechanism will dominate when the precipitates are small, and the Orowan strengthening mechanism dominates when they are larger. Therefore, it can be assumed that just the Orowan mechanism is happening when looking at dispersoid strengthening, as the dispersoids are larger precipitates. With this assumption, one can calculate the dispersoids contribution to the yield strength, σ_d, by using the Ashby-Orowan equation:

$$\sigma_D = \frac{0.84MGb}{2\pi(1-\nu)^{1/2}\lambda} ln\frac{r}{b} \tag{2.6}$$

Where ν is the poisons ratio. For Al-alloys the values M = 2, G = 27.4GPa, b = 0.286 nm and ν = 0.33 can be used (6, 7).

In practice, the precipitation hardening process consists of two heat treatments, which can be seen in Figure 2.3. The first is a solution heat treatment, where the alloy is heated to a certain temperature, usually just below the eutectic temperature. Here, most of the solute elements will dissolve to form a single-phase solution. Some stable intermetallic phases will, however, still be present. This temperature is held until the material is completely homogenized. Then, the alloy is quenched, and as the diffusion kinetics do not allow for particles to precipitate, the result is an alloy supersaturated with solute elements
(2, 3).

The second heat treatment is the precipitation heating, also known as the aging process. This heat treatment happens at a lower temperature than the homogenization. The temperature should be just high enough to allow sufficient diffusion to let the solute elements start to cluster together and form coherent precipitated zones that strengthen the material, called GP zones. For some alloys containing solutes with a high diffusivity at low temperatures, this can happen at room temperature, but most alloys need to be heated to get the desired effect. The GP zones are not particles, as they do not have a crystal structure of their own, but are coherent with the original aluminium lattice. These zones are very small, smaller than nucleates of new particles, which results in a large number of them appearing in the alloy. From these GP-zones, precipitates with a higher strengthening contribution nucleates. When the optimal hardness is reached, heat treatment condition T6 is reached. To find condition T6 the right temperature and the right holding time must be found empirically. If the temperature is too high, the impurity elements will start to form particles on the grain boundaries. If the alloy is heated for too long, known as over-aging, the precipitates will start to coarsen, which leads to a lower number density and, therefore, a lower hardness. In both cases, the hardening effect will drop significantly (2, 3).

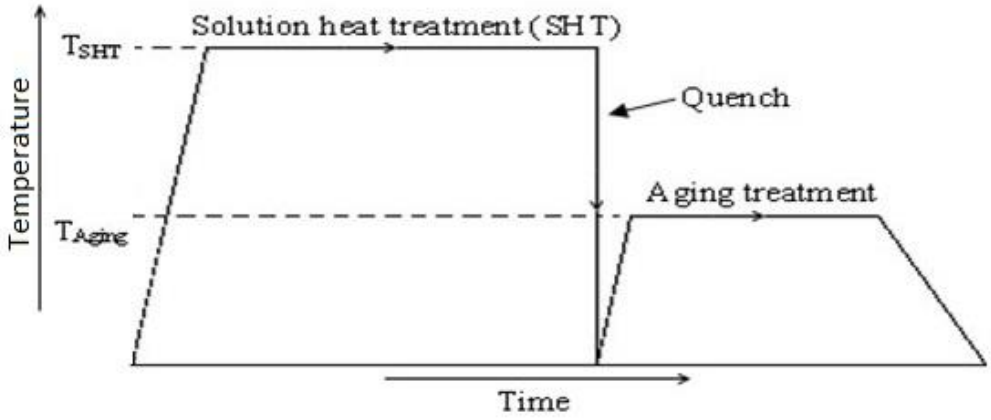

Figure 2.3: A schematic temperature-time plot showing the precipitation hardening process. The figure is adapted from figure 11.22 in Callister (3).

As the precipitates will influence the electrical conductivity of the hardened alloy, conductivity measurements are often used to indicate the volume fraction of precipitates. In general, the solutes in solid solution is the highest contribution to resistance in the alloy, so when the solutes start to precipitate out, the conductivity rises. The electrical conductivity will reach a peak when most of the solutes have precipitated out, but it will decrease when the precipitates start to

dissolve. Different elements contribute differently to the resistivity of the material. Zr will, for example, cause the alloy to have a higher resistivity than the equal amount of Cd. The relationship between the electrical conductivity σ and the concentration of Fe, Mn and Si in solid solution can be expressed as:

$$\frac{1}{\sigma} = 0.0267 + 0.032Fe_{SS} + 0.033Mn_{SS} + 0.0068Si_{SS} \quad (2.7)$$

Where the concentrations of the solute elements are in wt% (8-10). This equation shows that Fe and Mn have approximately the same contribution to the resistivity of the material, and that the contribution from the Si concentration is an order of magnitude smaller. Y. Zeng et al. (11) have also investigated the relative effects of several chemical elements on the electrical conductivity of Al alloys, and classified Cd as an element with a low effect on the electrical conductivity. Cr, Zr and Cu, on the other hand, have been found to have high effect on the electrical conductivity in Al in the same study.

2.1.1 Precipitation hardening in Al-Zr alloys

Additions of Zr effectively inhibit recrystallization at exposure to heat, which makes Al-Zr alloys promising for developing thermally stable Al-alloys that can be dispersoid strengthened (12). In Al-Zr alloys, the alloy is supersaturated with Zirconium in solid solution after the first heating and quenching. During ageing, the Zr precipitates out as Al_3Zr dispersoids to strengthen the alloy. However, it will not precipitate out with the $D0_{23}$ crystal structure these particles have in their equilibrium state. Instead, it will start to form metastable precipitates in a nano-meter scale $L1_2$ structure that is coherent with the matrix of the α-Al (13). Zr has a very low diffusion rate, which makes it coarsening resistant at temperatures up to 475 °C. The precipitates will, however, not be homogeneously distributed. During solidification, there will be a dendritic microsegregation of the Zr atoms, which leads to interdendritic channels being depleted of precipitates. This will have a harmful effect on the mechanical properties of the finished product (14).

When two elements are added to an alloy, they often have a synergetic effect. Both Zr and Sc are efficient precipitate hardeners, but their combined effect is much larger than the sum of the effect of each of them. Therefore, Sc is often added to the Al-Zr alloys (15). When this is the case, $Al_3(Sc_{1-x}Zr_x)$ precipitates will be formed under the hardening process. Here, x is smaller than 0.5, meaning that it will always be more Sc aluminides than Zr aluminides (14). The

concentration of Zr in the precipitates will, however, be much smaller than 50%, as it has a much lower diffusivity than Sc in α-Al. One will often find a Zr-rich shell outside a Sc-rich core, as Zr segregates at the α-Al/AlSc interface, which can be seen in Figure 2.4. Sc is thermodynamically stable in the $L1_2$ structure, but because of its faster diffusivity it is only coarsening resistant up to around 300 °C (13-17). The combination of the two elements is, however, more coarsening resistant, and leads to a higher density of smaller precipitates(15). Another benefit of using these two elements in combination is that by changing the Zr/Sc ratio, the mismatch in the lattice parameters of the precipitate and aluminium matrix can be tailored. An increase in Zr will decrease the lattice parameter mismatch, while additions of Sc will increase it (18). In later years, it has been a major focus on finding other elements that can substitute Sc, as it is very expensive.

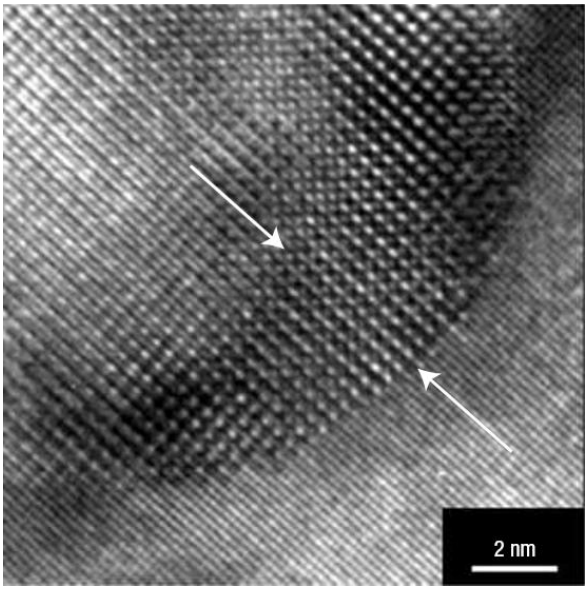

Figure 2.4: An $Al_3(Sc_{1-x}Zr_x)$ precipitate observed in an aluminium alloy containing 0.09at% Sc and 0.03at% Zr aged at 450 °C for 32 hours. The darker edge show that there is an increase in heavier Zr-atoms near the edge of the precipitate. The image is Figure 3 in Clouet et al. (15)

2.1.2 Precipitation hardening in a 7xxx alloy

The 7000-series of aluminium alloys contains additions of Zn, Mg and Cu, and is used extensively as structural material in airplanes and in military equipment due to their high strength/density ratio. The alloys in the 7000-series can reach a yield strength of 500-630 MPa, an ultimate tensile strength of 570-680 MPa and an elongation of 9% - 11%. The corrosion resistance of the alloys is, however, usually not sufficient, so the alloy is often covered with a layer of pure aluminium (19). The 7050 alloy contains 5.7-6.7wt% zinc, 2-2.6wt% copper and 1.9-2.6wt% Mg, which makes it very easy to be strengthened by precipitation.

The general precipitation sequence in these types of alloys is in four steps: supersaturated α-Al → GP → M' → $MgZn_2$. The phases will contain copper which will contribute to the precipitation hardening of the alloy, but most of the hardening effect from the copper comes from it being in solid solution. The GP-zones are coherent spheres that have a very low surface energy, making it possible to form several small zones at low temperatures (20-120 ℃). As they are both coherent and so closely dispersed, they are very efficient at hardening by stopping dislocation movement. The M' particles are monocline, partly coherent plates in the [111]-planes of the aluminium. These are even more efficient at hardening than the GP-zones, but they may lead to precipitate free zones and thereby intercrystalline fractures or corrosion. The $MgZn_2$ particles are incoherent and will not contribute to the hardening. They will however coarsen the structure, making it more brittle (19).

In practice, the 7000 series is often aged in one of three ways. Either 100 ℃ for 4 hours + 157 ℃ for 8 hours, 120 ℃ for 3 hours and 175 ℃ for 3 hours, or a one-step aging at 120 ℃. The two-step treatments should give a high density of small GP-zones at the lowest temperature that will grow at the highest temperature, resulting in a high density of larger GP-zones throughout the material. During the one-step treatment, the precipitates grow at a lower temperature, making the treatment more time consuming. Overageing the material leads to the development of M' and $MgZn_2$ particles, which are larger and therefore coarsen the structure (19).

2.1.3 Dispersion hardening in a AA3xxx alloy

The AA3003 alloy is a wrought aluminium alloy where manganese is a main alloying element. It has generally been strengthened by work hardening, and has therefore not been classified as heat treatable. However, later studies have shown that these alloys can precipitate strengthening dispersoids during heat treatment(7, 10, 20). Due to the good thermal stability of the strengthening dispersoids, the 3xxx alloys have good properties at elevated temperatures (250 ℃ - 350 ℃), such as good creep properties, and a relatively high yield strength of 78 MPa at 300 ℃ (21). By adding different solute elements these properties could be further increased. Some solute elements make the alloy able to be strengthened with the help of dispersoids. These elements often have a low diffusivity, which makes the alloy have excellent thermal stability at elevated temperatures. This is one of the benefits of dispersoid-strengthening as opposed to precipitation-strengthening, where the precipitates often coarsen at such temperatures (22).

The manganese in the alloy is dissolved in the aluminium matrix after solidification, leaving a supersaturated solid solution. During heat treatment of binary Al-Mn alloys the super saturated solid solution is decomposed to form dispersoids at a slow pace. Additions of other alloying elements will, however, have a major impact on the kinetics of the precipitation. Small additions of Si and Fe will increase the precipitation rate, as they decrease the solubility of Mn in the alloy. Fe generally favours the precipitation of $Al_6(Mn,Fe)$ dispersoids, but when both Fe and Si are present, the precipitation of $Al_{12}(MnFe)_3Si$ dispersoids are favoured (10, 22). Hansen et al. investigated a strip-cast AA3003 alloy, and found that after a short time of annealing at 400 ℃, an icosahedral quasicrystal phase was present in the alloy, together with the α-Al(MnFe)Si and $Al_6(Mn,Fe)$ dispersoids. This icosahedral quasicrystal phase is thought to be the first stage of the α-Al(MnFe)Si and $Al_6(Mn,Fe)$ dispersoids. Li and Arnberg (10) investigated a DC-cast AA3003 alloy, and found that dispersoids started to precipitate at 300 ℃ when the alloy was subjected to a heating rate of 50 ℃/h. At initial stages of the precipitation, they found an icosahedral, quasicrystal phase, confirming the work of Hansen et al. At higher temperatures, they found most of the dispersoids to be single cubic α-Al(MnFe)Si, which are coherent or semi-coherent to the matrix. They also found that the dispersoid number density was highest at 400 ℃. As the size of the dispersoids increase with higher temperatures, the number density of them will decrease.

Molybdenum is often added to this alloy because of its low diffusivity in Al, making it restrict the coarsening of the dispersoids at higher temperatures. At very small additions of Mo, Mo-containing dispersoids will form. As well as restricting coarsening and thereby improving mechanical properties at elevated temperatures, the Mo-containing dispersoids increase the creep resistance in the alloy. According to K. Liu et al. an addition of 0.3wt% of Mo will also produce finer dispersoids with a higher volume fraction, and reduce precipitate free zones compared to the base alloy (22).

2.1.4 The effect of Cadmium on precipitation hardening behaviour

The ageing behaviour of different alloys has been shown to change with small additions of Cd. In Al-Cu alloys, the usual precipitation sequence contains four steps: GP(I) → GP(II) → θ’ → θ. An addition of Cd to an Al-Cu alloy will lead to a reduction in the formation of GP-zones, and a higher rate of precipitation of θ’. Because of the increased rate of θ’ precipitation, much finer and more densely dispersed precipitates are observed in the alloy, as well as an increase

in hardness (23). The reduction in the formation of GP-zones is thought to be because trace elements, like cadmium, work as traps for vacancies by forming Cd-vacancy clusters or Cd-Cu-vacancy clusters. Thus, the vacancies used for diffusion will be eliminated, making diffusion in the alloy slower, thereby slowing down copper atoms going to the GP zones (24, 25). The increase in the precipitation rate of θ' precipitates is most likely a result of the nucleation of them happening at the coalescence of mobile Cd-Cu-vacancy clusters, or on dislocation loops, which Al-Cu alloys tend to form a fine distribution of in the presence of impurity elements when quenched (25). According to Noble (26), the precipitates also grow by movement of these clusters at temperatures up to 200 °C. At higher temperatures, the growth rate of the precipitates is controlled by normal diffusion of copper to the θ' precipitates. It has been proposed by Kanno et al. that Cd works as heterogeneous nucleation sites at elevated temperatures, which facilitates the growth of θ' precipitates (27). This theory has later been supported by Ringer et al., who have proposed that the Cd atoms rapidly form clusters during and right after quenching. Cd-particles are then thought to be formed uniformly at these clusters, and then work as heterogeneous nucleation sites (28). Both Kanno et al. and Ringer et al. did, however, only work with Sn, and assumed that the results would also be valid for Cd. According to Hardy, additions of 0.05-0.1 wt% Cd is enough to improve precipitation hardening in Al-Cu alloys significantly (29). During ageing, the Cd will precipitate out on the [111]-planes of the aluminium matrix, first forming preliminary precipitates termed Cd' at ageing temperatures up to 220 °C. At higher temperatures, up to around 400 °C, a more stable precipitate is formed (30, 31).

The boiling point of cadmium is quite low at 765 °C, leading to an unavoidable loss of cadmium during melting and solution heat treatment (25). Therefore, one should add Cd at a temperature below 765 °C, making it important to add it before adding other elements that may increase the melting point of the alloy, like Mo or Cr.

2.2 Scanning electron microscopy (SEM)

In the SEM, several signals are generated when the primary electrons from the incident electron beam hits the sample, as seen in Figure 2.5. Therefore, the SEM contains several detectors that can detect some of the different signals. The easiest one to use is the one that detects secondary electrons, the Everhart-Thornley detector. Secondary electrons are electrons that have escaped

from the metal in the sample because a primary electron collided with it. This signal will give a good view of the topography as the detector detects electrons diagonally from the sample (32).

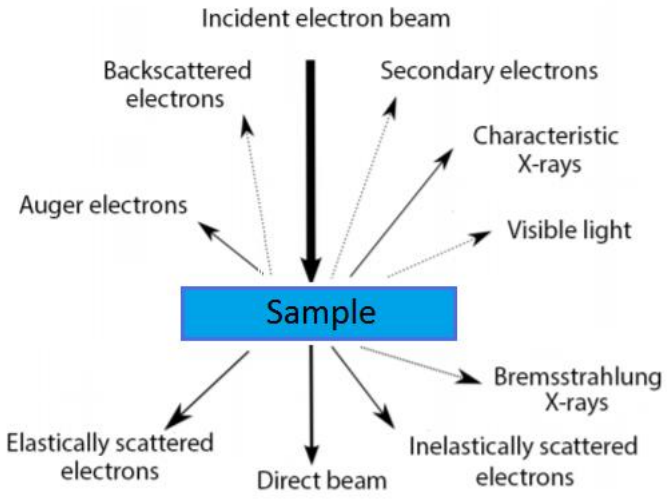

Figure 2.5: The different signals generated when primary electrons from the incident beam encounter the nuclei and electrons in the sample.

For identifying different phases, the backscattered electron signal is usually used. These images are obtained by the collection of primary electrons that scatter back from the sample after they have collided elastically with the nuclei. Heavy elements scatter the electrons more efficiently, making the signal stronger and thus making them appear brighter in the image. Because of this effect, one can easily determine which phase is which if the chemical composition of the different phases are known (32). There is also less topography shown when this signal is used, which makes it easier to measure the size of particles and area fractions of phases. This signal picks up the diffraction contrast well, which makes it easier to see grain boundaries and measure grain size.

To determine the chemical composition of the different particles and phases in the SEM images, energy-dispersive x-ray spectroscopy (EDS) is used. This technique allows a quantitative analysis of the chemical composition at a specific point on the sample. The electron beam is concentrated on this point, and some of the electrons on the lower energy levels will get excited to a higher level. When they fall back to their original energy level, a photon is emitted. As the energy levels of the electrons are quantified and specific for each individual element, the photon is characteristic for the element, and a chemical composition can be determined (32).

2.3 Transmission electron microscopy (TEM)

In a TEM the electrons transmit through the sample, instead of being reflected of it. Therefore, it is important to have samples that are thin enough to let electrons pass through. To achieve the correct thickness, multiple methods can be utilised, like crushing, electro polishing, ionic etching and ultramicrotomy. Electro polishing is most widely used, and can be used on all samples that are electrically conducting. The sample is first ground mechanically down to a thin film with a thickness of less than 100 µm, before small, circular disks are stamped from it. The disks are then electropolished until a hole has appeared on the sample. The areas close to the hole are now thin enough to be examined in the TEM (23).

The TEM is a series of components stacked in a column that is maintained at high vacuum. The different components are an electron gun, electromagnetic lenses, a sample holder, a viewing screen, and various detectors. The electron gun, usually a W, LaB_6, or a field emission gun (FEG), is located on top of the column. Here, electrons are bombarded from the tip of the gun due to an anode providing high voltage. Another anode accelerates the electrons to a high energy, typically 200keV. From here, the electrons pass through a series of lenses. First through the condenser lenses which are located below the electron gun, and converges the electrons to the desired spot size onto the sample. The electrons transmit through the sample, where they interact with the atoms they encounter. The objective lens is located beneath the sample, as can be seen in Figure 2.6. Here an image of the sample is produced, which later is magnified by the intermediate lenses and projected onto a fluorescent screen by the projector lens. The electrons are absorbed by the fluorescent screen, and it produces visible light that can be observed by the human eye. Alternatively, digital images can be captured by using an electron-sensitive charge-coupled device camera, a CCD camera. The CCD camera is located in one of the intermediate image planes. When the microscope is in image mode, a 2D projection image of the sample can be observed either with the CCD camera or on the fluorescent screen. This is because the objective lens converges all electrons from one point in the sample to one point in an image plane. The contrast in the projection image is a result from the interactions the electrons have had with the nuclei and electrons of the sample (23).

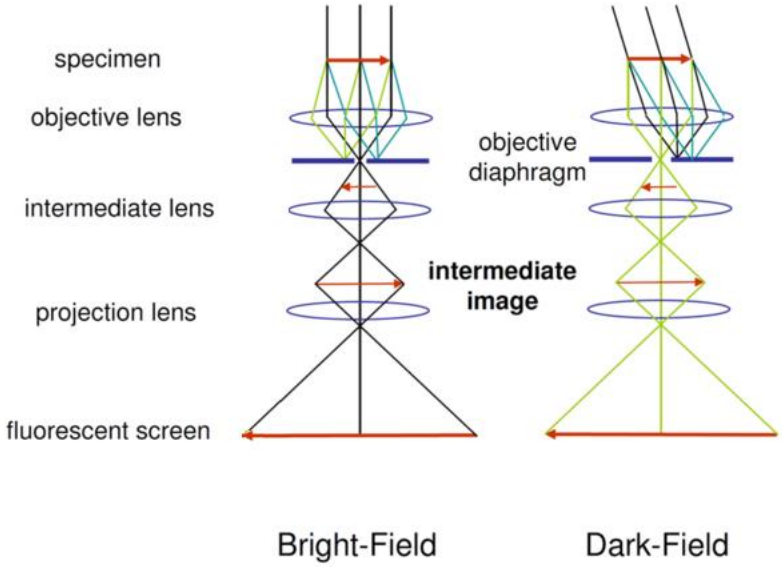

Figure 2.6: An illustration of the beam path through the microscope for bright field and dark field imaging (33).

The primary electrons from the incident beam are scattered via elastic and inelastic scattering processes in the same way as in a SEM, which can be seen in Figure 2.5. This is referred to as electron diffraction. The electrons that create viewable signals are the ones that are scattered elastically. These are scattered in all directions, but for certain scattering angles, they may interfere constructively due to their wave property. This constructive interference is called Bragg diffraction, and it happens at the atomic planes in crystalline materials when Braggs law is fulfilled:

$$2dsin(\theta) = n\lambda' \tag{2.8}$$

d is the distance between the diffracting planes, θ is the Bragg angle (the diffraction angle for constructive interference), λ' is the electron's wavelength, and n is an integer. When Braggs law is fulfilled, the path distance between two electrons scattered by parallel is an integer number of electron wavelengths for a certain angle, which is the reason why constructive interference occurs for exactly that angle. All electrons that are spread by the sample into a given angle are converged to one point in the objective lens' back focal plane, which is also called the diffraction plane. By changing the current in the electromagnetic lenses, the resulting diffraction pattern can be projected onto the viewing screen or the CCD camera. As the diffraction pattern is a Fourier transform of the sample image, it exists in reciprocal space, where the units are length^{-1}. Each reflection spot in this pattern is the result of elastic scattering from a set of atomic planes that fulfils Braggs law. From the diffraction pattern, it can be

determined which crystal planes the spots are from by indexing them. To index the diffraction spots, one needs to know the camera length of the microscope when the diffraction pattern was acquired, as well as the structure factor of the sample material, the structure factor being a mathematical description of what reflections are possible from a specific crystal system. The relation between the camera length, the distance between the diffraction spots, and the Bragg angle can be observed in Figure 2.7. From this figure, Braggs law and the assumption that sin θ = tan θ as θ is very small, the following relation arrives:

$$Rd = \lambda' L \tag{2.9}$$

R is the distance between the diffraction spots and L is the camera length (23).

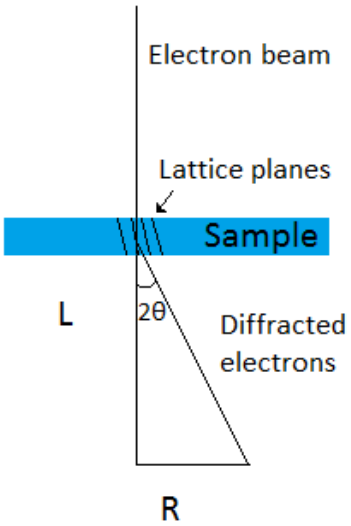

Figure 2.7: Schematic figure of the relation between the camera length (L), Bragg angle (θ) and the distance between the diffraction spots (R).

The TEM can be operated in many different modes. Two of these are bright field and dark field imaging. A bright field image is obtained when the objective aperture only lets the direct beam go through the objective diaphragm. If one of the Bragg reflected beams go through the objective aperture, a dark field image can be obtained, as we can see from Figure 2.6. This leads to a bad resolution of the areas in the samples that causes a large scattering of the electrons in bright field mode, as all the electrons that are scattered are filtered out. In both modes, the contrasts in the image come from some areas on the sample scattering the incoming beam more than others. Therefore, the contrast is called a diffraction contrast. The contrasts most often come from bend in the sample, from dislocations and from particles or precipitates (23).

Electron energy loss spectroscopy (EELS) can also be performed using a TEM. The electron beam has electrons with a known, narrow range of kinetic energies. These electrons are directed towards the sample, go through it, and the energy loss of the electrons is detected on the other side with an electron spectrometer, which will also interpret what caused the energy loss. Using this method, one can therefore determine what elements are present in the sample. The method also allows for measuring the local thickness in the sample by measuring the energy loss spectrum. This spectrum will have a zero-loss peak, which is a peak from electrons who have not lost any energy. To calculate the thickness this peak is extracted, and the integral below it is calculated, as well as the integral underneath the whole spectrum. The thickness t can then be calculated by the following equation:

$$t = mfp * \ln(\frac{I}{I_0}) \tag{2.10}$$

Where I is the integral below the whole spectrum, I_0 is the integral below the zero-loss peak and mfp is the total mean free path of electron inelastic scattering, which is tabulated for most metals. For Al this value is tabulated as 88 nm when an acceleration voltage of 200keV is used. This is a relatively efficient way of measuring the thickness, giving accurate and reliable results (34-36). Equation (2.10) is also used in combination with the following equation to calculate the number density of precipitates:

$$ND = \frac{\#Precipitates}{A*(t+\bar{D})} \tag{2.11}$$

Where A is the area where the precipitates are observed, t is the thickness of that area and $\bar{D}$ is the mean diameter of the precipitates. The unit of the number density is precipitates per μm^3.

2.4 Tensile testing

Uni-axial tensile testing is one of the most fundamental material quality tests. The aim of the test is to measure the resistance of a material to static or slowly applied force, which is why the strain rates in a tensile test are very small. A test specimen is placed in a test machine, and a uniaxial force is applied along the axis of it, as can be seen in Figure 2.8. An extensometer is mounted so that it measures the elongation of the specimen throughout the test. The tensile force is gradually adjusted so that the strain rate is constant, gradually increasing the true stress until fracture (2, 3, 37).

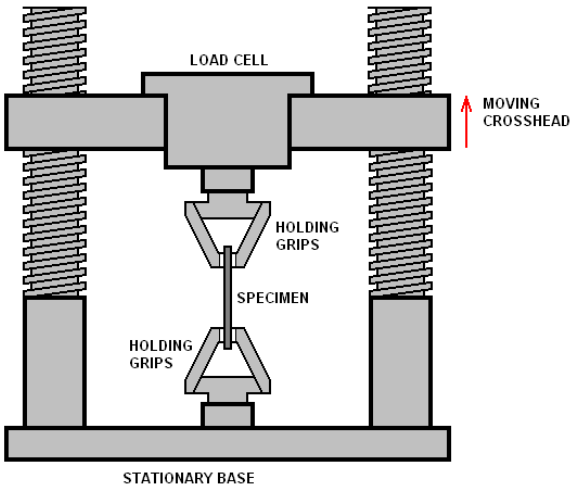

Figure 2.8: Schematic drawing of a tensile test machine from The Engineering Archives (38).

When the test is finished, one can immediately find maximum elongation and reduction in the cross-section area of the sample. The test machines software will create a stress-strain curve for the material, from which one can find information about the strength and ductility of the material, such as the ultimate tensile strength (UTS), yield strength(YS) and Young's modulus. One can also find the amount of work hardening by finding the increase of stress from the yield strength to the ultimate tensile strength, which is the strengthening during plastic deformation (2, 3, 37). An example of a typical stress strain curve for a metal is found in Figure 2.9. Here, the ultimate tensile strength and yield strength are shown, and the Young's modulus can be found by taking the slope of the elastic area, which is the linear part of the curve.

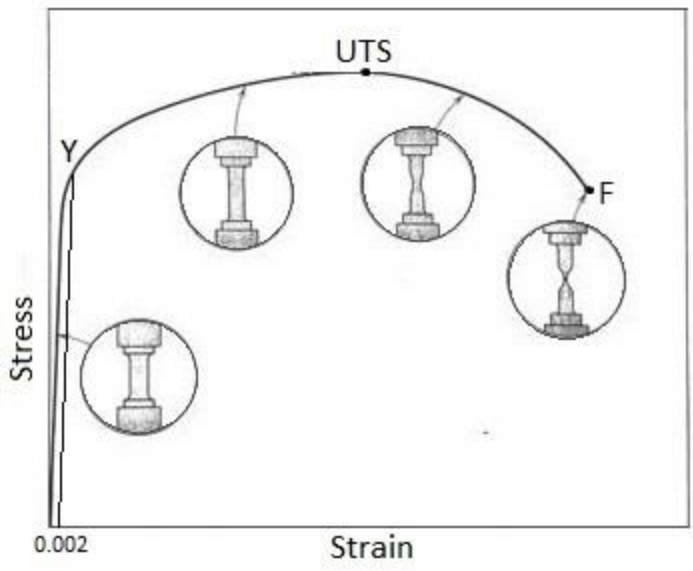

Figure 2.9: A typical engineering stress-strain behaviour to fracture point F. The ultimate tensile strength (UTS) and yield strength (Y) is indicated, and geometry of the specimen at various points along the curve is showed. The figure is adapted from Figure 6.11 in Callister (3)

Chapter 3: Experimental work

3.1 Making the alloys

Nine different alloys were manufactured from three base alloys: Commercially pure aluminium (99.7%), AA3003 and AA7050. Before all castings, 1% of the grain refiner Al-5Ti-1B was added to the melt, which dissolved in about a minute. To avoid porosity in the samples, all melts were degassed by bubbling argon for approximately 2 minutes. During this time hydrogen and oxide films are being removed, a process that is sketched in Figure 3.1. The slag was then scraped off using a ladle, and the melts were cast. After casting, all ingots were cooled using water.

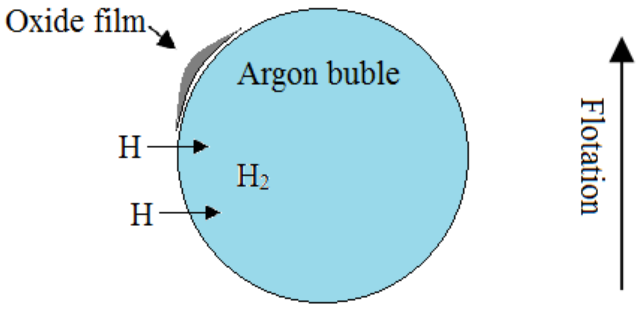

Figure 3.1: Sketch of the mechanism of degassing by bubbling with Argon.

3.1.1 Al-Zr(-Cd)

Table 3.1: Chemical contents of samples 1-4.

Alloy name	Alloy
Al-Zr 1	Al-0.16Zr
Al-Zr 2	Al-0.18Zr
Al-Zr 3	Al-0.23Zr
Al-Zr-Cd 1	Al-0.26Zr-0.23Cd
Al-Zr-Cd 2	Al-0.12Zr-0.29Cd

The first Al-Zr alloy was made by melting commercially pure Al in a crucible at 750 °C before pure Zr was added to the melt. It was cast after a holding time of about two and a half hours. The second alloy was made in the same way, but as the melting point of Zr is very high

(1855 °C), a holding time of approximately 16 hours was used. In both cases, only half of the melt was cast. The remaining melts, Al-Zr 1 and Al-Zr 2, were used to make Al-Zr-Cd 1 and Al-Zr-Cd 2, respectively. Cadmium was added to a content of approximately 4wt% in both melts, but as the Cd has a low boiling point, some of it was lost by evaporation. The Al-Zr 3 alloy was made at a later time, by combining Al-Zr 1, Al-Zr 2 and an Al-30Zr master alloy. After casting, it was left in the mould to cool down for about 30 minutes before being further cooled using water.

To check the contents of the alloys, small samples were cut and prepared from the cast ingots. They were ground and polished to 3 μm using the steps 1-6 in Table 3.2, washed thoroughly using an ultra-sonic cleaner and examined with XRF.

3.1.2 AA3003-Mo-Cd(-Cr)

The alloys were made by first melting an AA3003 ingot at 750 °C, then adding pure Cd after the temperature had decreased to 700 °C to keep it from evaporating. Cd was added to the melt before Mo to avoid evaporation, as the Mo raises the melting point of the melt. When the cadmium dissolved, an Al-40Mo master alloy was added. The temperature was increased to 900 °C as the melting point of Mo is very high (2623 °C). To make sure the master alloy dissolved, the melt was left over night for approximately 17 hours before half of the melt was cast.

To make the AA3003-Mo-Cd-Cr alloy, an Al-20%Cr master alloy was added to the remaining melt, with a holding time of approximately 2 hours before casting. Small samples were cut from both ingots. These were ground and polished down to 3 μm using step 1-6 in Table 3.2 and washed using an ultra-sonic cleaner, before examination in XRF.

3.1.3 AA7050(-Cd)

The reference AA7050 sample was from a regular AA7050 ingot. The AA7050-Cd alloy was made by first melting the AA7050 ingot at 750 °C, then adding pure Cd after the temperature had decreased to 700 °C, to keep it from evaporating. When the Cd had dissolved, the melt was cast. Small samples were cut from both ingots. These were ground and polished down to 3μm using step 1-6 in Table 3.2 and washed using an ultra-sonic cleaner, before examination in XRF.

3.2 Hardening and hardness measurements

For the hardening experiments sample specimen of approximately 1.5cm x 1.5cm x 1cm were cut from the ingots, using a Struers Labotom-15 and a Struers Labotom-5. The Vickers hardness was measured in all heat-treated samples, using a Matsuzawa hardness tester with a load of 1kg. 8 indents were made on each sample, and the highest and lowest hardness values were filtered out. The 6 remaining values were averaged, and plotted against holding time or last ageing temperature.

When measuring electrical conductivity, a Foerster Sigmatest 2.069, which was calibrated using standards with a conductivity of 58.5MS/m and 4.415MS/m, was used. 6 measurements of electrical conductivity were done on each sample, and the results were averaged.

3.2.1 Al-Zr(-Cd)

13 sample specimens of each of the five alloys were made and 10 of them were solid solution heat treated at 640 ℃ for 24 hours before they were quenched in cold water. Hardness and chemical content were measured amongst the samples to ensure homogeneity.

The 10 solid solution heat treated samples were heated isochronally in a Nabertherm N15/65HA air circulation furnace with a heating rate of 50 ℃/h from room temperature to 600 ℃. With steps of 50 ℃ from 150 ℃ to 600 ℃ the samples were held on the same temperature for one hour before one was taken out. Thereby samples aged at the following temperatures were collected: 25 ℃ (RT), 150 ℃, 200 ℃, 250 ℃, 300 ℃, 350 ℃, 400 ℃, 450 ℃, 500 ℃, 550 ℃, 600 ℃. This will later be referred to as the fast heat treatment.

The as cast samples were subjected to another isochronal heat treatment, which was done using the same method and furnace, but with steps of 25 ℃, a heating rate of 25 ℃/h and a holding time of 3 hours at each step. Samples were collected, at 400 ℃, 450 ℃ and 500 ℃. This heat treatment was only performed on the two Cd-containing alloys, and the Al-Zr 2 alloy. Later, it was also performed on the Al-Zr 3 alloy together with tensile tests from the Al-Zr-Cd 1 alloy, and samples from these two alloys were also tested at 200 ℃. This will later be referred to as the slower heat treatment.

3.2.2 AA3003-Mo-Cd(-Cr)

12 sample specimens from each of the two alloys were made. Before heat treating, hardness measurements were made on 4 of the sample specimen from each alloy to ensure homogeneity among the samples, as well as finding the hardness of the as cast samples. In a Nabertherm N15/65HA air circulation furnace the samples were heated from 25 ℃ to 600 ℃ continuously at a rate of 50 ℃/h. One sample from each alloy was taken out and quenched in 50 ℃ intervals from 150 ℃ to 600 ℃.

As some of the hardness results from the AA3003-Mo-Cd-Cr alloy were unexpectedly high, XRF measurements were taken on four of the samples. As these showed that the Mo in the alloy was not homogeneous, the alloy was remelted, cut and heat treated the same way once more. After remelting, a homogeneous alloy was obtained.

An interesting peak in hardness was found at 200 ℃, so a sample from the remelted cast were aged in an oil bath at 185 ℃. They were taken out and water quenched after 10 minutes, 30 minutes, 1 hour, 2 hours, 4 hours, 6 hours, 8 hours, 12 hours, 24 hours, 48 hours and 100 hours. Hardness and electrical conductivity was measured before further ageing was continued.

3.2.3 AA7050(-Cd)

4 sample specimens from both the AA7050 alloy and the AA7050-Cd alloy underwent solid solution heat treatment for 4 hours at 475 ℃. Two aging methods were then preformed. First, a one-step aging, where the samples were held in an oil bath at 120 ℃ until peak hardness was seen. The samples were taken out of the oil bath, water quenched, and hardness- and conductivity tested after 10 minutes, 30 minutes, 1 hour, 2 hours, 4 hours, 6 hours, 8 hours, 10 hours, 12 hours, 24 hours, 48 hours and 96 hours.
A two-step aging method was also tried. The samples were held in an oil bath at 120 ℃ for 6 hours, before being moved to an oil bath at 160 ℃, were it was held until peak hardness was seen. The samples were taken out of the oil bath, water quenched, and hardness- and conductivity tested after 10 minutes, 30 minutes, 1 hour, 2 hours, 4 hours, 6 hours, 8 hours, 10 hours, 12 hours, 24 hours and 48 hours.

3.3 Microstructural analysis

For the AA3003-Mo-Cd alloy, the isochronally heated samples to 350 ℃, 450 ℃ and 550 ℃ were examined in SEM, as well as an as cast sample. The samples heated to 300 ℃ - 600 ℃ were examined in a TEM, as well as the sample heated to 200 ℃. Two samples collected from the Al-0.26Zr-0.23Cd alloy, heated to 200 ℃ by the fast heat treatment and 450 ℃ by the slow heat treatment were examined in a TEM. The as cast structure of the five Al-Zr(-Cd) alloys were also examined using a SEM.

3.3.1 SEM samples

The samples were mounted in EpoFix^{TM}, ground and polished using the steps in Table 3.2, down to 0.04μm. As the sample needs to be electrically conducting in the SEM, the ends of the samples were not covered with epoxy. For examination, a Zeiss Supra 55VP SEM was used, with secondary electron imaging, backscattered electron imaging and Energy-dispersive X-ray spectroscopy (EDS).

Table 3.2: Grinding and polishing of samples for examination in a SEM.

Step number	Grinding/polishing medium	Roughness	Time
1	SiC-paper	500 particles per cm^3	-
2	SiC-paper	800 particles per cm^3	-
3	SiC-paper	1200 particles per cm^3	-
4	SiC-paper	2400 particles per cm^3	-
5	DiaPro Allegro	9 μm	4 minutes
6	DiaPro Dac	3 μm	4 minutes
7	DiaPro Nap	1 μm	2 minutes
8	OPS	0.04 μm	1 minute

3.3.2 TEM samples

TEM samples were made by cutting 1.5 mm thick slices from the sample specimens using a Struers Minitom. These were ground to a thickness of 80-100μm, by first grinding one side with 800ppi, 1200ppi and 2400ppi grinding paper, taping it to a piece of epoxy and then grinding the other side using the same papers. To remove the thin film from the epoxy without bending it, the samples were submerged in liquid nitrogen for 15 minutes before the films were removed using a scalpel. 5-6 TEM 3 mm sample disks were stamped out of the films using a

Gatan 659 Disc Punch. To achieve the correct thickness, these were electropolished at -25 °C, with a voltage of 20 V, using 1/3 HNO_3 and 2/3 methanol as electrolyte in a Struers TenuPol-5 until a small hole was present. The samples were cleaned with ethanol quickly after electropolishing. These were then examined in a JEOL JEM-2010 TEM. The obtained TEM images were analyzed using the software iSolution DT, in which the size distributions of the dispersoids can easily be found. To make the size distributions, the measurement of the equal circle diameter was chosen. From these data, number density and mean size was calculated, as well as the theoretical strengthening contribution from the dispersoids.

3.4 Tensile testing

From the AA3003-Mo-Cd alloy, samples with the last ageing temperature of 200 °C, 450 °C and 600 °C, as well as an as cast sample, were tensile tested. These were heated from room temperature to 600 °C with 50 °C/h, and the 600 °C samples were held at that temperature for 24 hours to be solid solution heat treated. Test specimens from this alloy were machined using the measurements in Figure 3.2. Two parallel samples were tested for each heat treatment.

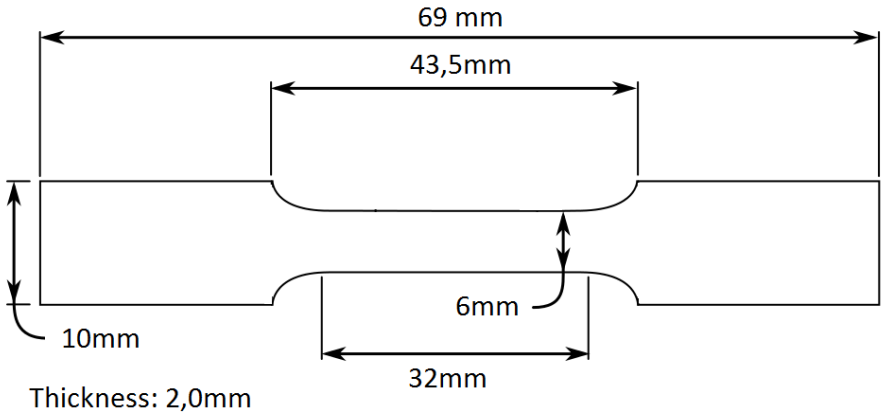

Figure 3.2: A sketch showing the measurements of the tensile test specimen for the AA3003-Mo-Cd samples.

The strength of the Al-0.23Zr and the Al-0.26Zr-0.23Cd alloys were tested after several heat treatments, as can be seen in Table 3.3. For the Al-Zr-Cd alloy, samples from both the first and the second hardness peaks in each heat treatment were tensile tested, while for the Al-Zr alloy only the second peak in both treatments were tested. As cast samples and solid solution heat treated samples were also tensile tested for both alloys. Test specimens from this alloy were machined using the measurements in Figure 3.3. Two parallel samples were tested for each heat treatment.

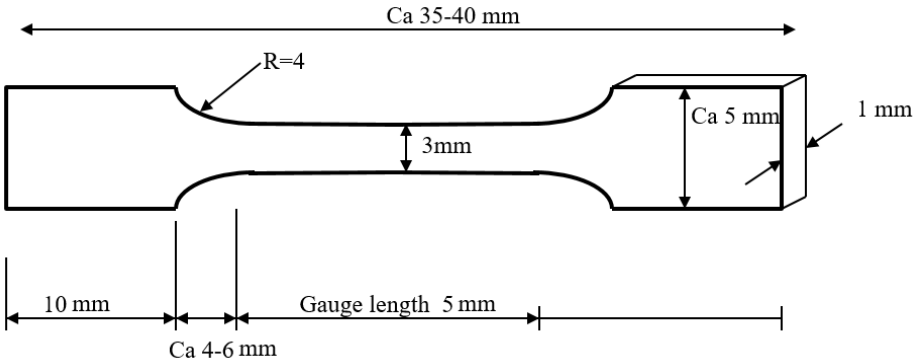

Figure 3.3: A sketch showing the measurements of the tensile test specimen for the Al-Zr and Al-Zr-Cd samples.

Table 3.3: an overview of which samples have been tensile tested. Here, 50 °C/h and 25 °C/h refers to the heat treatments using those heating rates, respectively.

Heat treatment	**Al-Zr**	**Al-Zr-Cd**
As cast	X	X
640 °C, 24h	X	X
200 °C, 50 °C/h		X
200 °C, 25 °C/h		X
450 °C, 25 °C/h	X	X
500 °C, 50 °C/h		X
550 °C, 50 °C/h	X	

Chapter 4: Results

4.1 Compositions

Results from the XRF analysis can be found in Table 4.1. These are averaged from the full results found in Appendix A. For the first two Al-Zr alloys the Zr levels were approximately the same after 2 and 17 hours holding time when adding pure Zr to pure Al. However, after adding Cd to the melts, the amount of Zr increased by 0.1% in the Al-Zr 1 alloy, which had the shortest holding time, while the Zr content in the Al-Zr 2 alloy decreased by 0.04%. This could indicate that there was some undissolved Zr in the Al-Zr 1 alloy, and that it dissolved after the ingot was remelted. The explanation for the decrease in Zr content with the addition of Cd in the second alloy can be explained by Zr oxidizing and being removed with the slag. When Cd was added, the total amount of metal also increased, making the percentage of Zr smaller. This will be the reason for a small part of the decrease in the amount of Zr in the Al-Zr 2 alloy.

Table 4.1: Results from XRF investigations. The results are averaged based two to three measurements. The AA3003-Mo-Cd alloy is referred to as AA3003, and the AA3003-Mo-Cd-Cr alloy is referred to as AA3003+Cr.

Alloy	Si	Mn	Mg	Zn	Fe	Ti	Cr	Zr	Cd	Cu	Mo
Al-Zr 1	0.024	0.006	<0.15	0.023	0.071	<0.004	0.009	0.16	-	-	-
Al-Zr 2	0.006	0.012	0.108	0.021	0.068	0.013	0.005	0.18	-	-	-
Al-Zr 3	0.003	<0.002	<<0.12	0.021	0.076	0.017	0.007	0.23	-	-	-
Al-Zr-Cd 1	0.029	0.007	<<0.14	0.11	0.11	0.021	0.007	0.26	0.23	-	-
Al-Zr-Cd 2	0.011	0.005	<<0.16	0.023	0.080	<0.004	0.008	0.12	0.29	-	-
AA3003	1.21	1.02	<0.099	0.017	0.55	0.024	0.007	0.014	0.17	0.064	0.15
AA3003+Cr	1.53	1.04	<0.098	0.017	0.56	0.011	0.20	0.015	0.15	0.60	0.19
AA7050	0.26	0.29	2.10	5.06	0.27	-	0.21	0.02	-	1.22	-
AA7050+Cd	0.14	0.27	2.02	5.08	0.34	0.11	0.16	0.02	0.28	1.34	-

4.2 Hardness and electrical conductivity after heat treatment in Al-Zr(-Cd) alloys

4.2.1 After solid solution heat treatment

The results from the hardness measurements after the SHT are found in Table 4.2, where one can see that both Cd-containing alloys are harder than the three alloys without.

Table 4.2: Hardness and electrical conductivity of the alloys after the SHT. The hardness and conductivity of each alloy is an averaged result of four samples with four tests per sample.

Alloy	Composition	Hardness[HV]	Electrical conductivity[MS/m]
Al-Zr 1	Al-0.16Zr	23.8	32.4
Al-Zr 2	Al-0.18Zr	23.5	32.2
Al-Zr 3	Al-0.23Zr	24.3	29.8
Al-Zr-Cd 1	Al-0.26Zr-0.23Cd	29.0	30.5
Al-Zr-Cd 2	Al-0.12Zr-0.29Cd	28.2	32.3

4.2.2 After isochronal heating

The samples were heated to isochronally to 600 degrees, and hardness and electrical conductivity was measured on steps of 50 ℃ degree from 150 ℃ to 600 ℃, from which the results can be found in Figure 4.1, Figure 4.2 and Table 4.3. The Cd-containing alloys are much harder than the alloys without Cd, and have hardness peaks at 200 ℃. The Al-0.26Zr-0.23Cd alloy has another a hardness peak at 500 ℃ as well, which is significantly higher than any of the other alloys. The Al-0.23Zr and Al-0.26Zr-0.23Cd alloys are comparable with respect to Zr content, and these show that an addition of 0.23 wt% Cd leads to a 6 HV larger increase from SHT to max hardness in this alloy.

Table 4.3: Increase in hardness from SHT to maximum hardness.

Alloy	**Increase in hardness**
Al-0.16Zr	2.5 HV
Al-0.18Zr	5.4 HV
Al-0.23Zr	7.0 HV
Al-0.26Zr-0.23Cd	13.0 HV
Al-0.12Zr-0.29Cd	15.9 HV

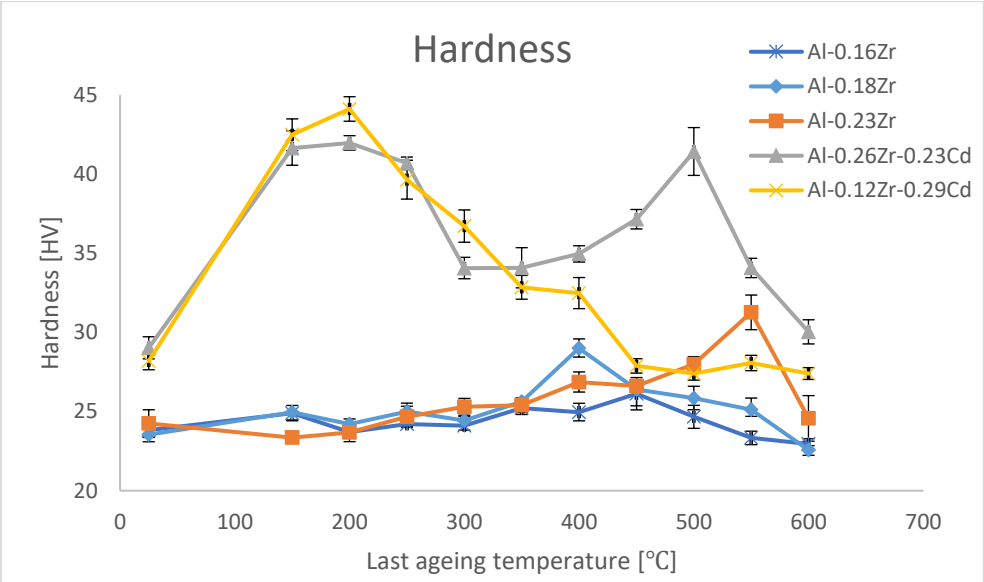

Figure 4.1: Hardness of the Al-Zr(-Cd) samples isochronally heated with 50 °C intervals and a holding time of one hour at each interval.

The electrical conductivity results from the fast heat treatment can be found in Figure 4.2. The two alloys with the highest Zr content, the Al-0.23Zr and Al-0.26Zr-0.23Cd alloys, have a much lower electrical conductivity before heat treatment than the others. The Al-0.12Zr-0.29Cd alloy has the highest conductivity of the alloys. This clearly shows the high impact Zr has on the EC. Comparing to the Al-0.16Zr and Al-0.23Zr alloys respectively, the Al-0.12Zr-0.29Cd and Al-0.26Zr-0.23Cd alloys have a much more rapid increase from the SHT samples to the maximum EC, as well as having achieved maximum EC at a lower temperature.

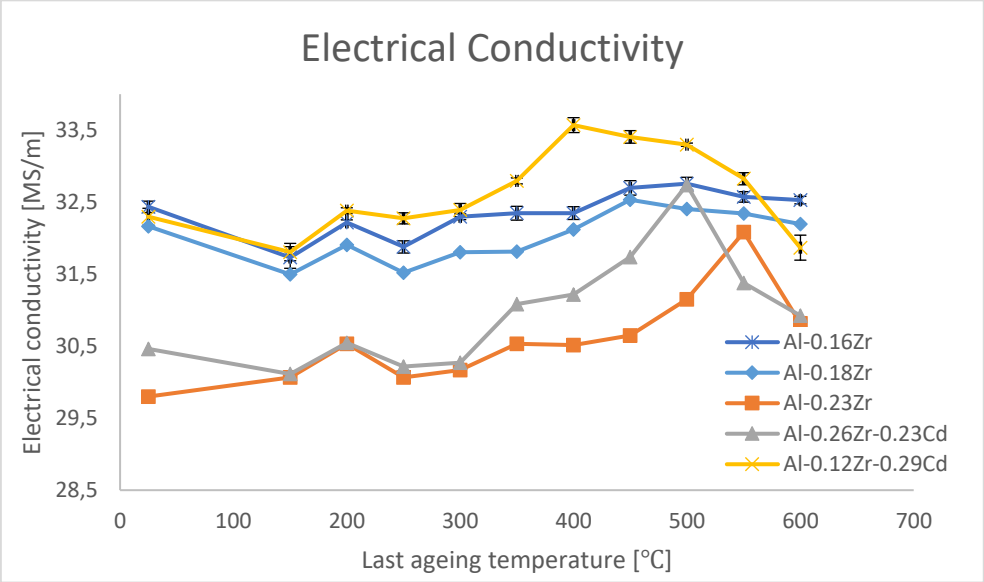

Figure 4.2: Electrical conductivity measurements from the four Al-Zr(-Cd)-alloys that were isochronally heated with 50 °C intervals and a holding time of one hour at each interval.

4.2.3 The effect of heating rate on dispersoid strengthening

The hardening experiment was repeated, but with steps of 25 ℃ from 150 ℃ to 600 ℃, 3 hours holding time at each step and with samples collected at 400 ℃, 450 ℃ and 500 ℃ for four of the alloys. For the Al-0.23Zr and Al-0.26Zr-0.23Cd alloys 200 ℃ samples were collected as well. The hardness results from this experiment can be found in Figure 4.3, Figure 4.4 and Table 4.4. We can see that with these heating parameters the Al-0.26Zr-0.23Cd alloy, which is the hardest alloy, has an increase in hardness of 20.1HV. When using the faster heat treatment, the same alloy had an increased hardness of only 13HV. The hardness peak also comes at a lower temperature using this method, at 450 ℃ instead of at 500 ℃. Comparing the Al-0.26Zr-0.23Cd and Al-0.23Zr alloys, the difference in hardness increase between these is smaller using this heat treatment, with only 2.7 HV as opposed to 6 HV in the faster heat treatment.

Table 4.4: The increase in hardness from as cast sample to the maximum hardness.

Alloy	**Increase in hardness**
Al-0.18Zr	3.2 HV
Al-0.23Zr	17.4 HV
Al-0.26Zr-0.23Cd	20.1 HV
Al-0.12Zr-0.29Cd	0.5 HV

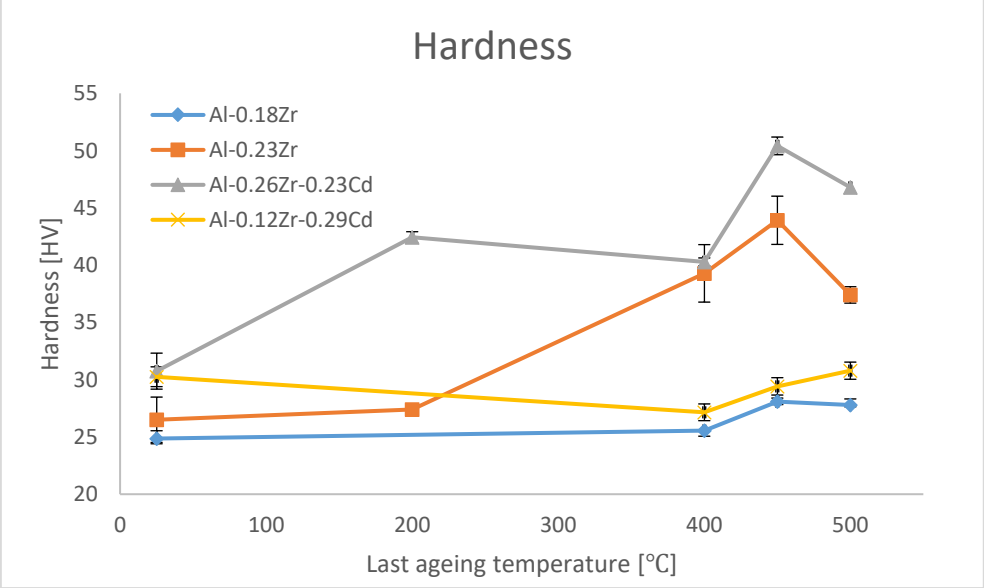

Figure 4.3: Hardness of the Al-Zr(-Cd) samples isochronally heated with 25 ℃/h in steps of 25 ℃, and a holding time of 3 hours at each step.

The electrical conductivity measurements from the slower heat treatment, which are found in Figure 4.4, show the same trends as in the fast heat treatment. The Al-0.12Zr-0.29Cd alloy, which is the alloy with the lowest Zr content, has the highest EC, even though it also has the highest Cd content. The two alloys with the highest Zr content have a much lower electrical conductivity before heat treatment than the two others, but the EC of the Al-0.26Zr-0.23Cd alloy is higher than of the Al-0.18Zr alloy at its peak at 450 °C. The Al-0.12Zr-0.29Cd and Al-0.26Zr-0.23Cd alloys achieve maximum EC at a lower temperature than the Al-0.16Zr and Al-0.23Zr alloys respectively.

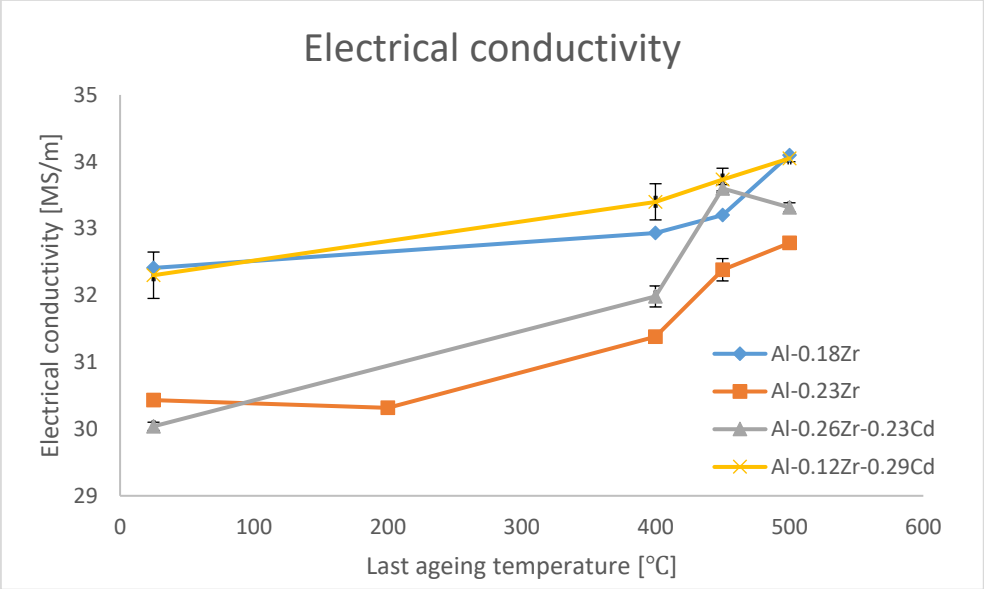

Figure 4.4: Electrical conductivity of the Al-Zr(-Cd) samples isochronally heated with 25 °C/h in steps of 25 °C, and a holding time of 3 hours at each step.

4.3 Microstructural analysis of the Al-Zr(-Cd) alloys

4.3.1 The solidification structures

Al-0.16Zr

SEM images and a selection of EDS results before heat treatment of the Al-0.16Zr alloy are shown in Figure 4.5, Figure 4.6 and Table 4.5. These show that the Zr in the alloy has precipitated out as small platelets of an $AlZr_x$-phase, and that iron-containing particles have formed clusters. Full EDS from all alloys results can be found in Appendix B: Full EDS results. According to the EDS results, the clusters contain 13-15wt% Fe, and the platelets contain 47.5wt% Zr. They also indicate that the matrix only contains Al. No Fe is detected in the spherical clusters of particles in EDS area 2 for this alloy, which is most likely because the magnification is not high enough, making the measurement too inaccurate.

a) 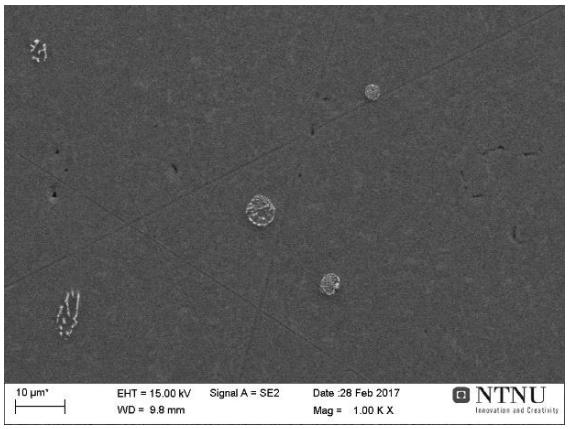

b) 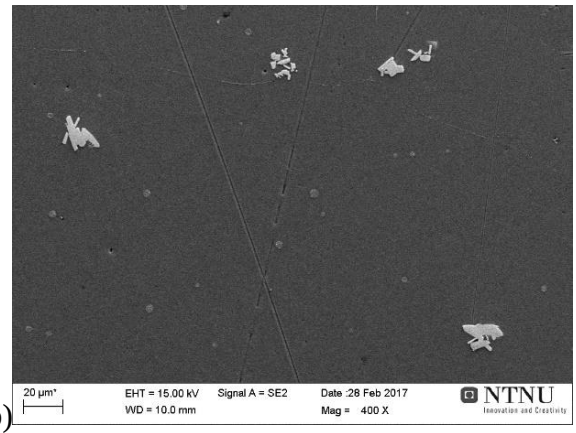

Figure 4.5: EDS analysis has shown that the circular spots clearly shown in a) are Fe impurities, while the platelets shown in b) are Al-20Zr.

a) 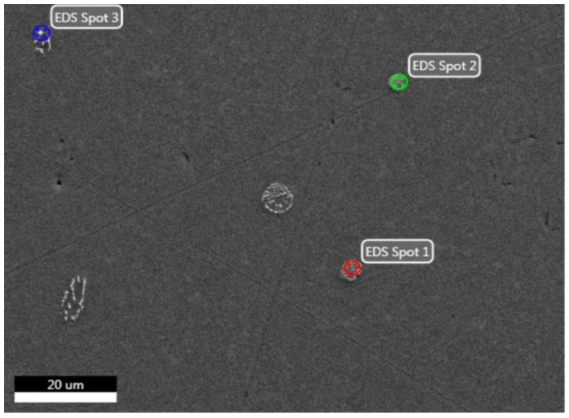

b) 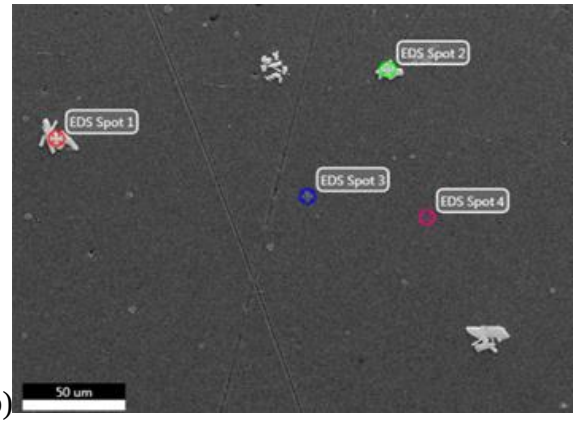

Figure 4.6: a) is EDS area 1 including the spherical cluster of Fe-containing particles, b) is EDS area 2 containing both the clusters and Zr-containing platelets.

Table 4.5: Results from the EDS analysis in the Al-0.16Zr alloy. Elements detected at the given spot are balanced with Al.

Spot	Fe [Wt%]	Fe [At%]	Zr[Wt%]	Zr[At%]
Area 1, spot 1	13.8	7.2	-	-
Area 1, spot 2	15.0	7.8	-	-
Area 1, spot 3	-	-	-	-
Area 2, spot 1	-	-	47.5	21.1
Area 2, spot 2	-	-	44.9	19.4
Area 2, spot 3	-	-	-	-
Area 2, spot 4	-	-	-	-

Al-0.18Zr

SEM images and a selection of EDS results from the Al-0.18Zr all 2 can be found in Figure 4.7 and Table 4.6. These images show approximately the same structure as the Al-0.16Zr alloy, with $AlZr_x$ platelets containing 46.8wt% Zr, clusters of impurity particles containing 10-20wt% Fe, and only Al detected in the matrix.

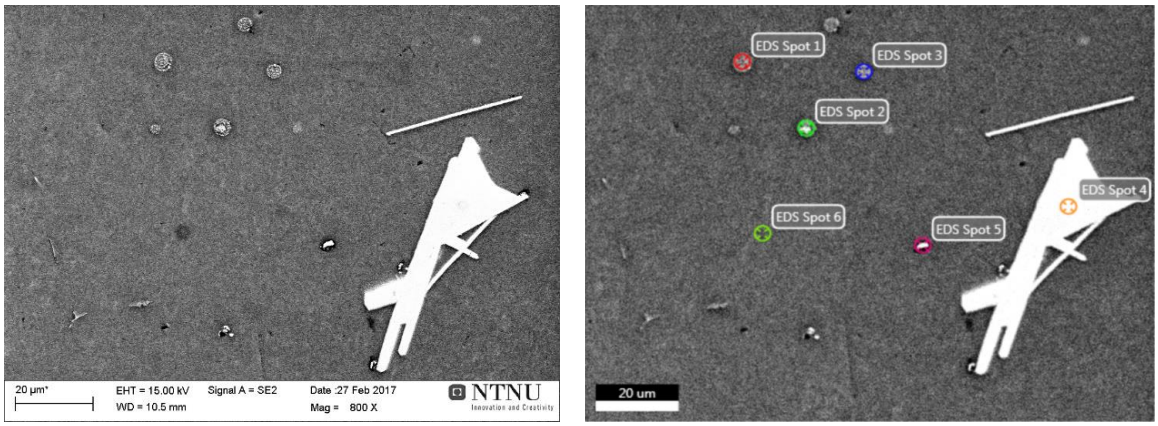

Figure 4.7: SEM images showing platelets containing Zr and circular clusters of Fe impurities.

Table 4.6: Results from the EDS analysis in the Al-0.18Zr alloy. The elements detected at the given spot are balanced by Al.

Spot	Fe [Wt%]	Fe [At%]	Zr[Wt%]	Zr[At%]
1	10.1	7.3	-	-
2	19.7	13.5	-	-
3	12.3	7.9	-	-
4	-	-	46.8	20.6
5	20.7	11.4	-	-
6	-	-	-	-

Al-0.23Zr

In Figure 4.8 it can be seen that the alloy has a dispersion of particle clusters throughout the material. From the EDS results in Figure 4.9 and Table 4.7 it is apparent that these particles contain 10-17wt% Fe, as well as small amounts of Si, meaning some Al(Mn,Fe)Si phase might be present. No platelets were observed in the structure, and only Al is detected in the matrix.

a) 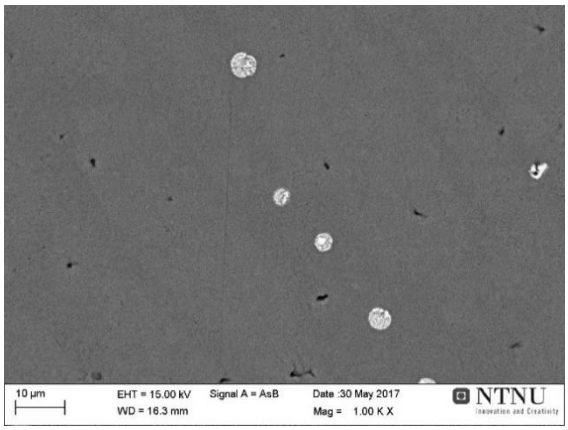

b) 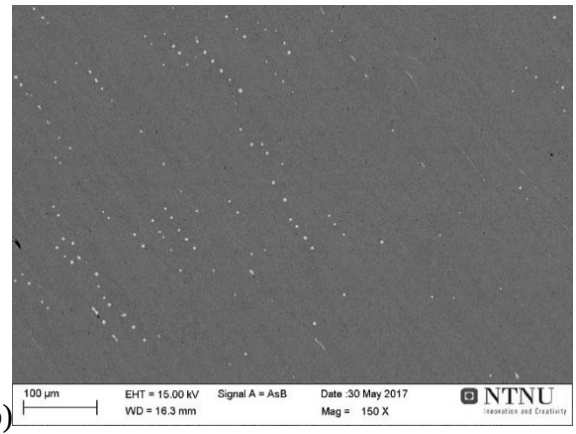

Figure 4.8: a) shows spherical clusters of particles similar to the Fe-particles in the previous alloys. In b) it is apparent that there is a high number of these in the material.

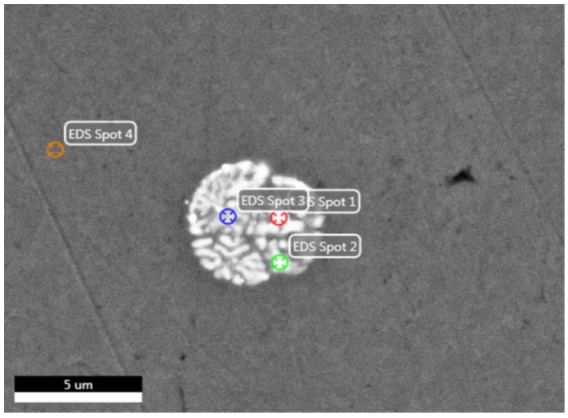

Figure 4.9: EDS area containing the spherical cluster of particles.

Table 4.7: Results from the EDS analysis in the Al-0.23Zr alloy. The elements detected are balanced with Al.

Spot	Fe [Wt%]	Fe [At%]	Zr[Wt%]	Zr[At%]	Si[Wt%]	Si[At%]
1	16.7	11.5	-	-	1.8	2.5
2	10.6	7.1	-	-	-	-
3	11.9	8.1	-	-	-	-
4	-	-	-	-	-	-

Al-0.26Zr-0.23Cd

Figure 4.10, Figure 4.11 and

Table *4.8* are images and EDS results from the as cast structure of the Al-0.26Zr-0.23Cd alloy. These shows precipitated, rectangular particles that contain 46.9wt% Zr, and Fe-containing particles along the grain boundaries where varying amounts of Fe is detected. The Fe-containing particles do, however, not look like the particles seen in the Al-Zr alloys without Cd. These could be an Al_3Fe-phase.

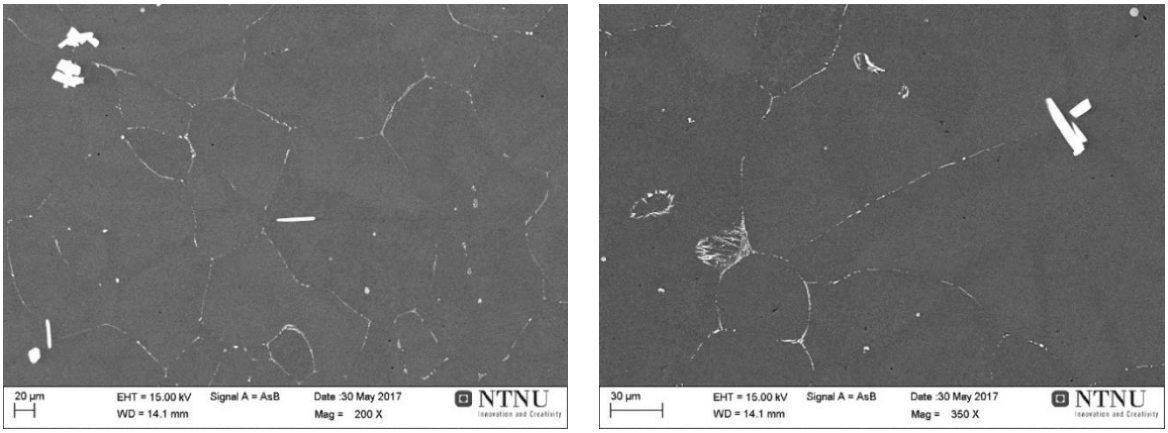

Figure 4.10: The solidification structure of the Al-0.26Zr-0.23Cd alloy.

a)

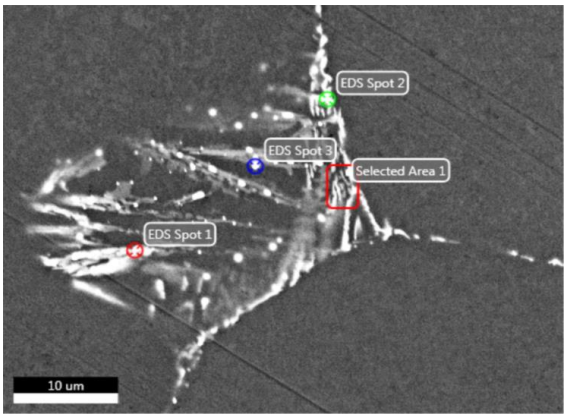

b)

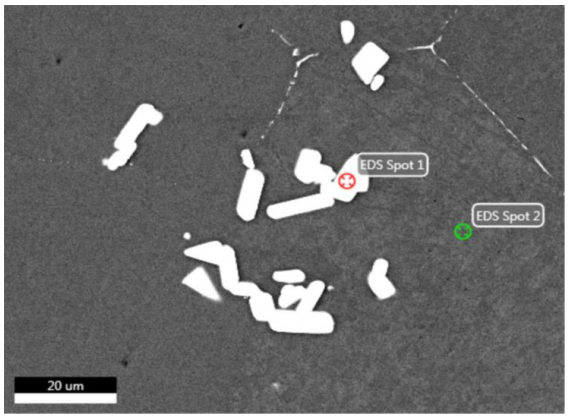

Figure 4.11: EDS area 1 (a), and EDS area 2 (b). EDS area 1 shows impurities on the grain boundaries, EDS area 2 contains precipitated particles.

Table 4.8: Results from the EDS analysis in the Al-0.26Zr-0.23Cd alloy. The elements are balanced with Al.

Spot	Fe [Wt%]	Fe [At%]	Zr[Wt%]	Zr[At%]
Area 1, spot 1	10.1	5.2	-	-
Area 1, spot 2	3.0	1.5	-	-
Area 1, spot 3	-	-	-	-
Area 1, SA 1	5.0	2.5	-	-
Area 2, spot 1	-	-	46.9	20.7
Area 2, spot 2	-	-	-	-

Al-0.12Zr-0.29Cd

The as cast structure contains $AlZr_x$ platelets with approximately 45-47wt% Zr, particles along the grain boundaries, and spherical clusters of particles containing 10.9wt% of Fe, as can be seen in Figure 4.12, Figure 4.13 and Table 4.9.

a) 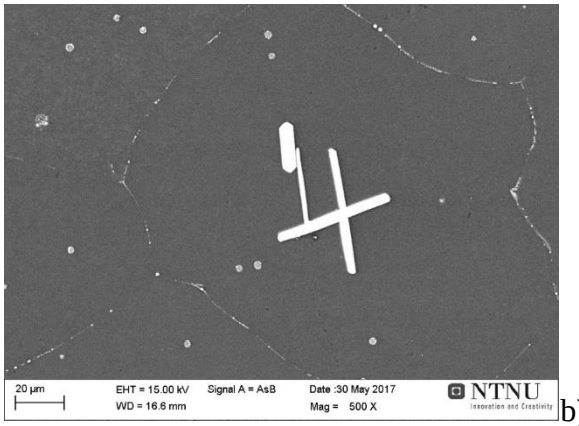

b) 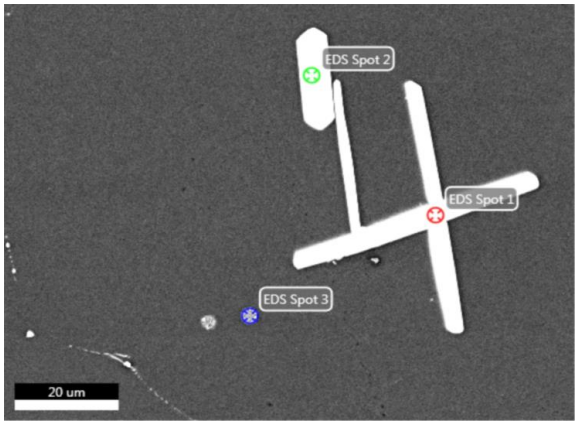

Figure 4.12: a) The as cast structure contains platelets of precipitated Zr-containing particles, particles along the grain boundaries and Fe-containing clusters of particles. b) shows the EDS spots for this alloy.

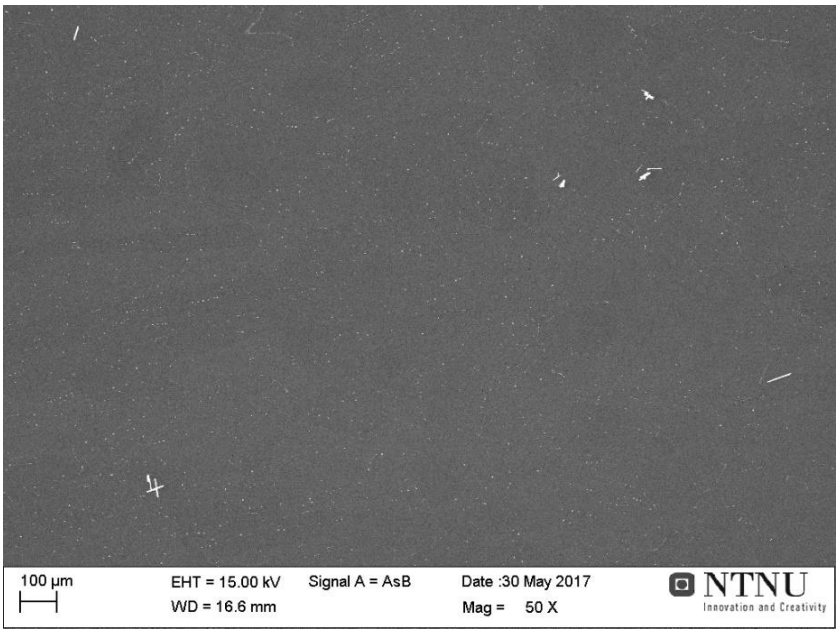

Figure 4.13: The clusters of iron-containing particles are dispersed evenly throughout the material, but the Zr-containing platelets are not.

Table 4.9: Results from the EDS analysis in the Al-0.12Zr-0.29Cd alloy. The elements detected at the given spot are balanced with Al.

Spot	Fe [Wt%]	Fe [At%]	Zr[Wt%]	Zr[At%]
1	-	-	45.7	20.0
2	-	-	47.1	20.1
3	10.9	5.6	-	-

4.3.2 Investigation of the hardening precipitates using TEM

The Al-0.26Zr-0.23Cd samples that was heated to 200 ℃ and 450 ℃ was investigated in a TEM, and micrographs from these samples can be found in Figure 4.14 and Figure 4.15 respectively. The mean size of the precipitates in the 450 ℃ sample and the particles from the 200 ℃ sample was calculated, of which the results can be found in Table 4.10. The diffraction pattern corresponding to the micrographs from the 450 ℃ sample that indicate that the precipitates have a $L1_2$ structure can be found in Figure 4.16.

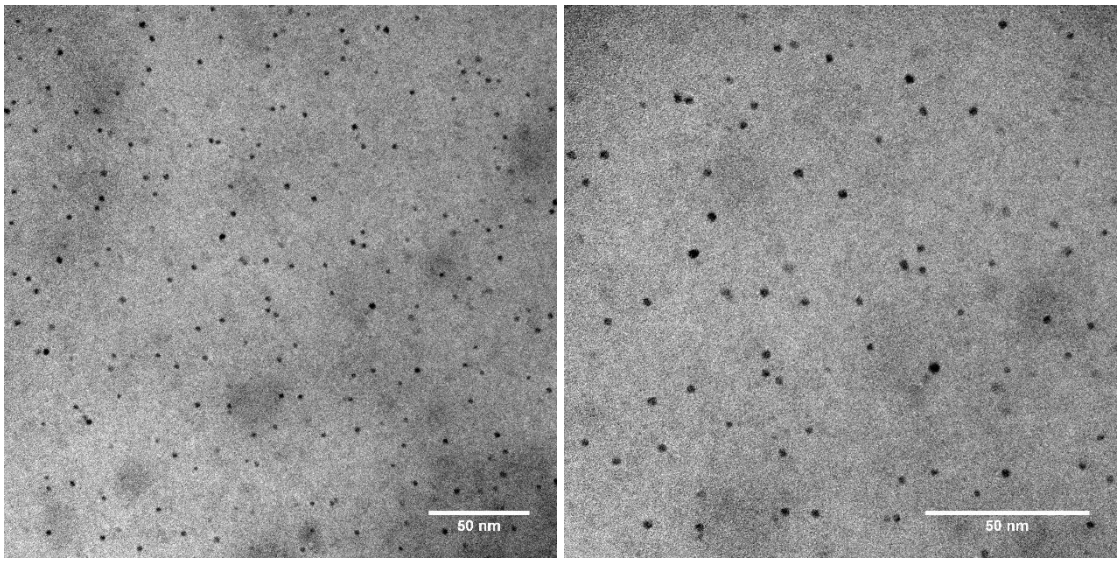

Figure 4.14: TEM micrographs of the Al-0.26Zr-0.23Cd sample heated to 200 ℃.

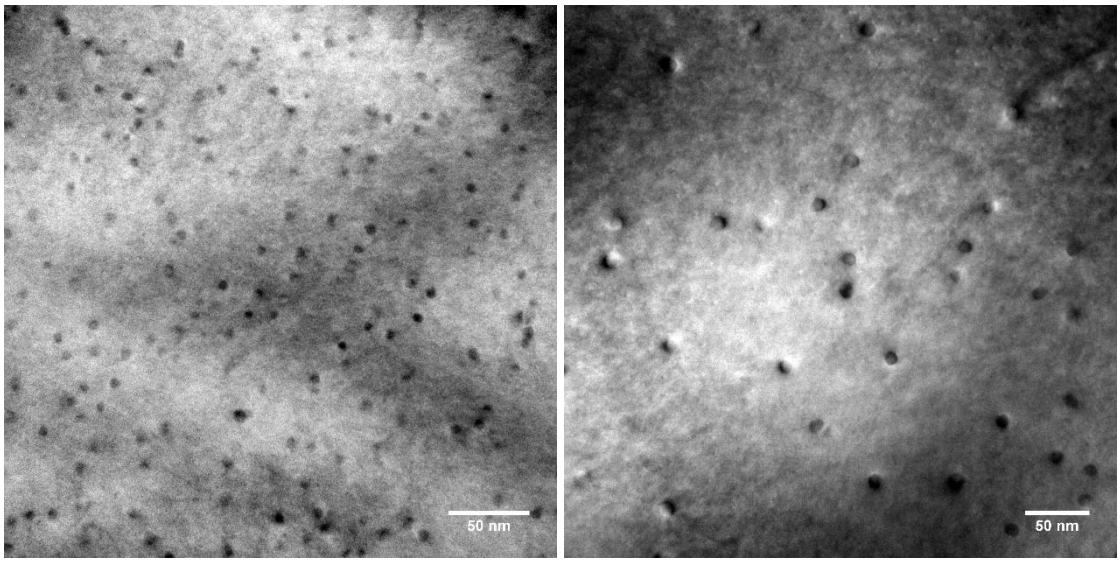

Figure 4.15: TEM micrographs of the Al-0.26Zr-0.23Cd sample heated to 450 ℃. The black spots are presumed to be $Al_3(Zr_xCd_{1-x})$ precipitates.

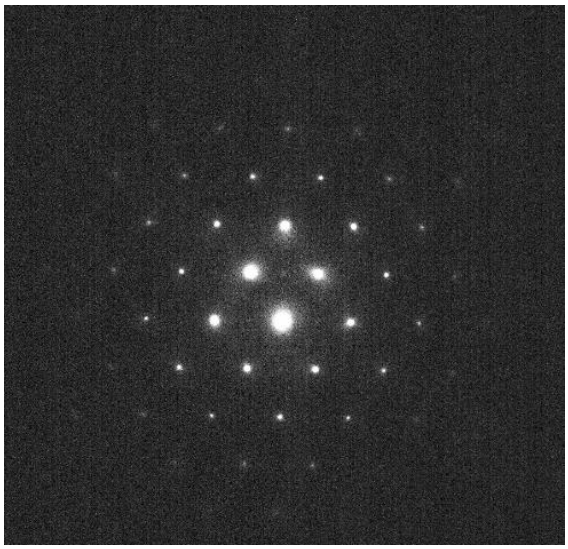

Figure 4.16: Diffraction pattern corresponding to the micrographs in Figure 4.15, with a [110]-zone axis. The DP indicates that the precipitates have a $L1_2$ structure.

Table 4.10: Mean sizes of the precipitates at different temperatures.

Temperature	Mean size
200 ℃	2.48 nm
450 ℃	5.72 nm

4.4 Strength of Al-Zr(Cd) alloys

The strength of the Al-0.23Zr and the Al-0.26Zr-0.23Cd alloys were tested after various heat treatments, and the yield- and ultimate tensile strength of these can be found in Figure 4.17 and Figure 4.18. Stress strain curves of the same specimens can be found in Figure 4.19 through Figure 4.22. These show that the maximum yield- and tensile strength in the Al-Zr alloy are obtained by ageing the sample to 450 ℃ using the slower heat treatment. For the Al-Zr-Cd alloy the maximum yield strength is obtained by ageing the sample to 200 ℃ using the slower heat treatment, while maximum tensile strength is achieved with ageing to the same temperature, but using the faster heat treatment. The samples denoted 25C/h have been subjected to the slower heat treatment, while the samples denoted 50C/h have been subjected to the faster heat treatment. The Al-0.26Zr-0.23Cd alloy has a higher maximum yield- and tensile strength than the Al-0.23Zr, but when comparing the 450 ℃ samples subjected to the slow heat treatment, the difference between them is very small.

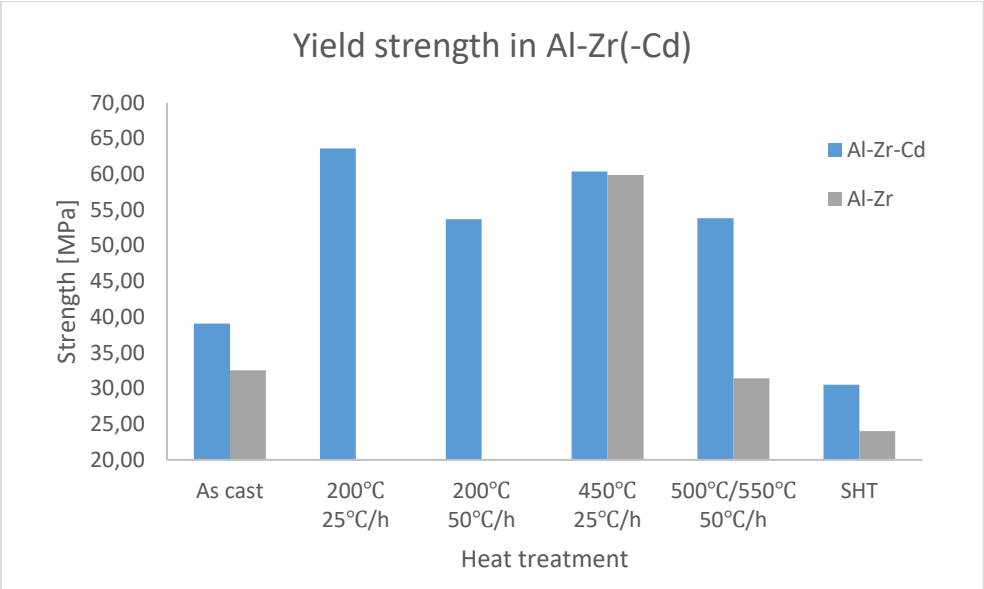

Figure 4.17: Yield strength of the samples from the Al-0.23Zr and Al-0.26Zr-0.23Cd alloys.

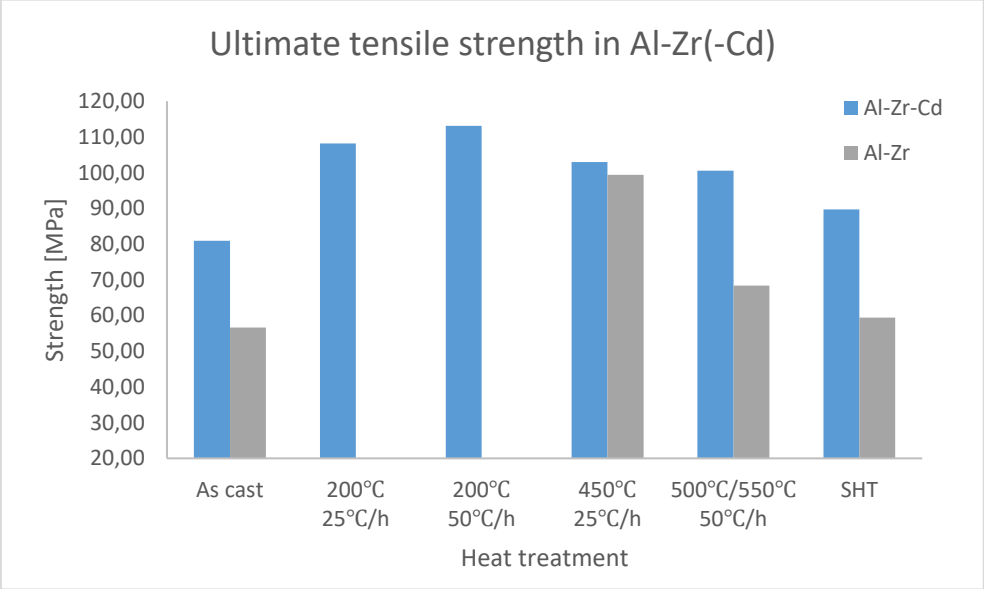

Figure 4.18: Ultimate tensile strength of the samples from the Al-0.23Zr and Al-0.26Zr-0.23Cd alloys.

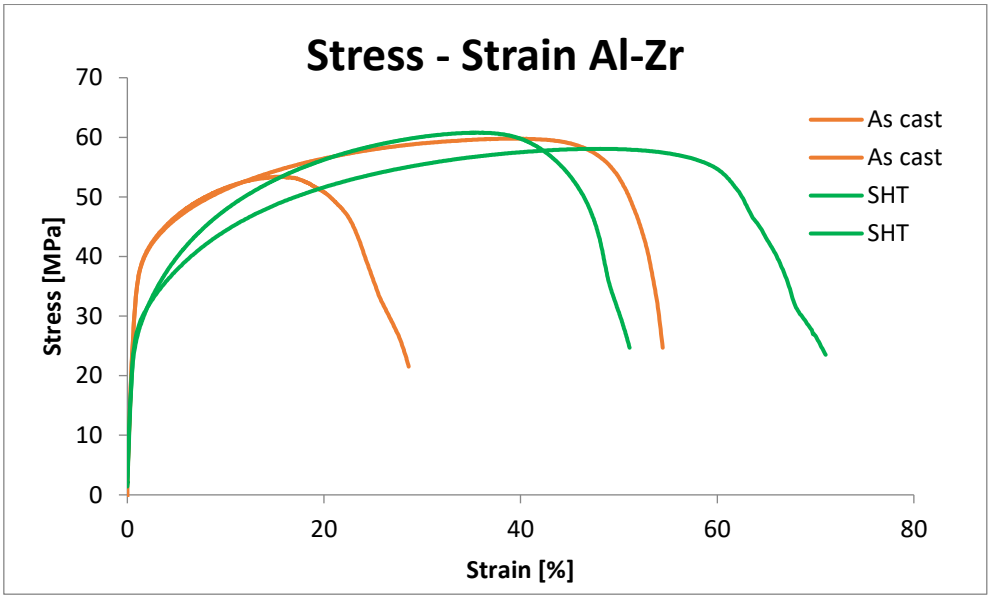

Figure 4.19: Stress-Strain curves for the solid solution heat treated and as cast samples of the Al-0.23Zr alloy.

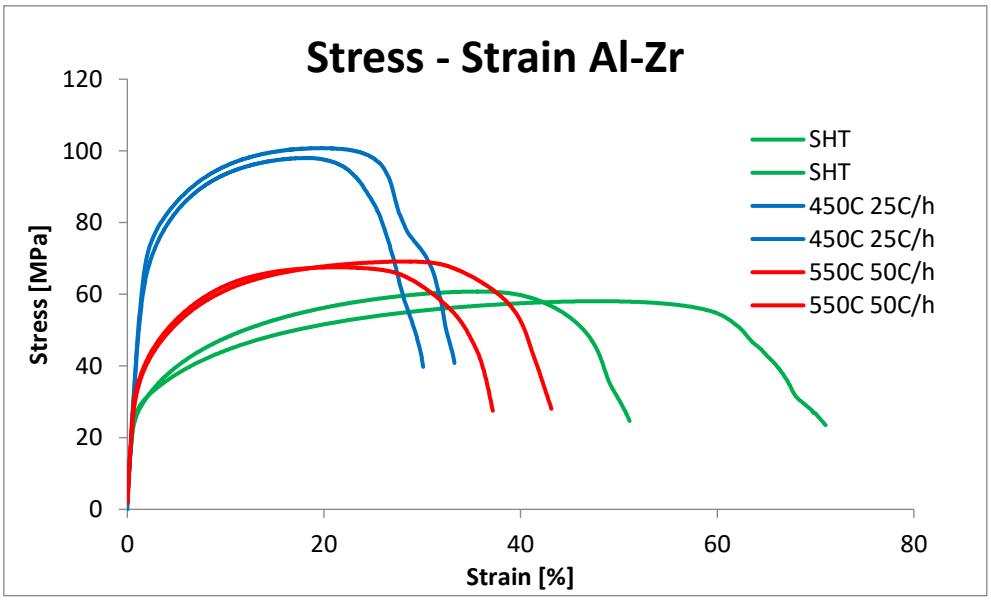

Figure 4.20: Stress-strain curves for the SHT sample of the Al-0.23Zr alloy, and the samples heated to 450 ℃ and 550 ℃ with different heat treatments.

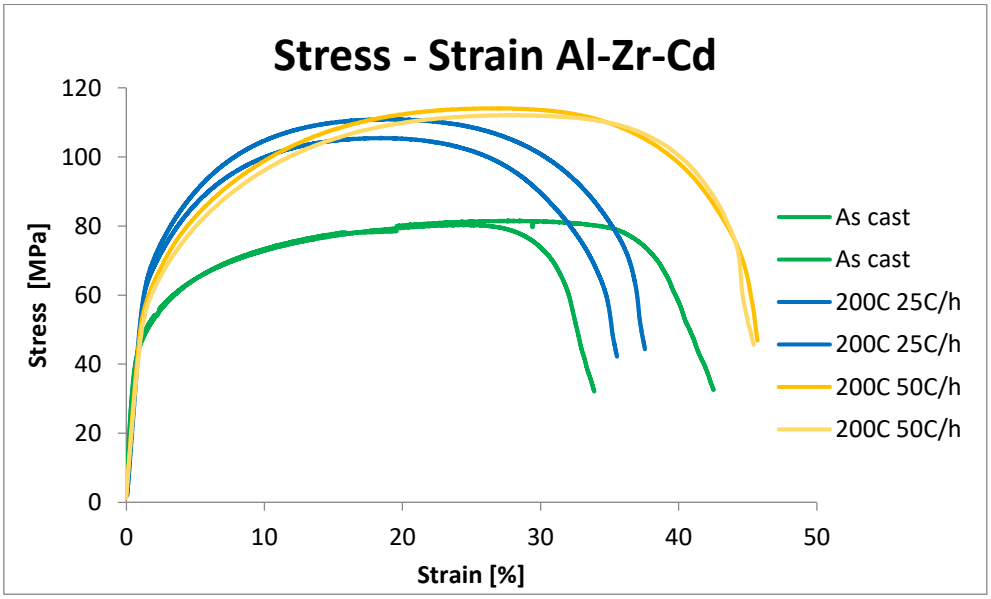

Figure 4.21: Stress-strain curves for the samples heated to 200 ℃ of the Al-0.26Zr-0.23Cd alloy, with the as cast sample as reference.

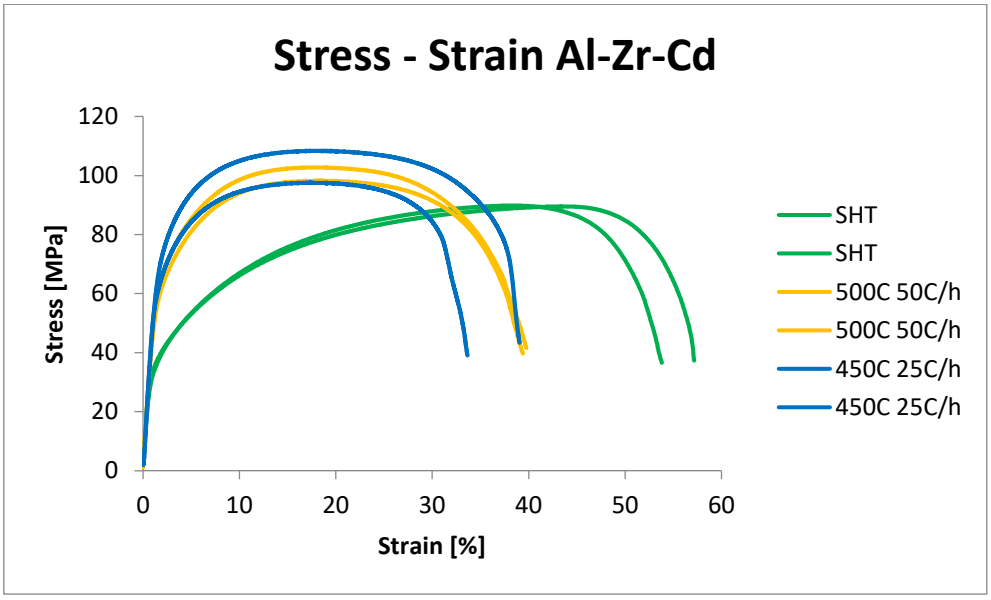

Figure 4.22: Stress-strain curves for the samples heated to 450 ℃ and 500 ℃ of the Al-0.26Zr-0.23Cd alloy, with the SHT sample as reference.

4.5 Hardness and electrical conductivity in AA3003-Mo-Cd(-Cr) alloys

4.5.1 After continuous heating

Both the AA3003-Mo-Cd-Cr and AA3003-Mo-Cd alloys were heated continuously with a heating rate of 50 °C/h. Hardness and electrical conductivity were measured in intervals of 50 °C, as can be seen in Figure 4.23 and Figure 4.24. The alloys have two hardness peaks, at 200 °C and 450 °C for the alloy with Cr and at 250 °C and 450 °C - 500 °C for the alloy without Cr. The first peak is highest for the alloy with Cr, and the last is highest for the alloy without Cr. Results from AA3003(-0.2Cd) alloys which have had the same heat treatment as the AA3003-Mo-Cd(-Cr) alloys is included for comparison. They can be found in Figure 4.25.

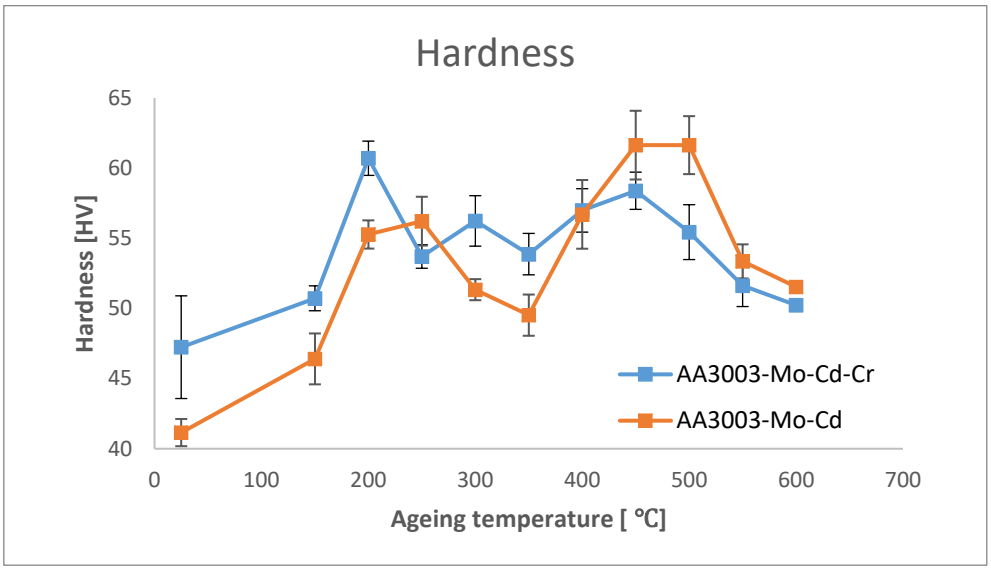

Figure 4.23: Hardness of the AA3003-Mo-Cd and AA3003-Mo-Cd-Cr alloys at different aging temperatures. These results are from the first casting of the AA3003-Mo-Cd-Cr alloy.

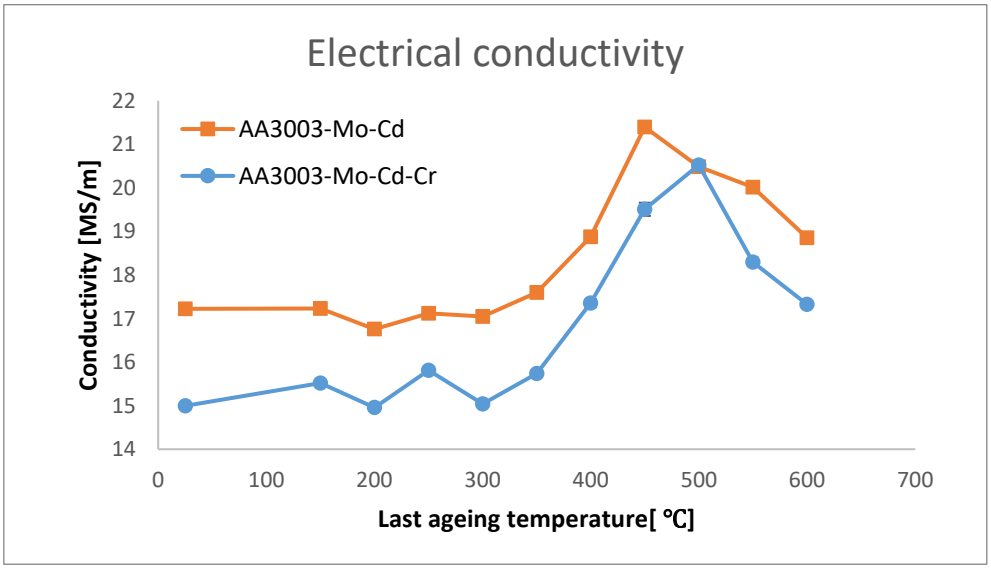

Figure 4.24: Electrical conductivity vs. last ageing temperature for the AA3003-Mo-Cd and AA3003-Mo-Cd-Cr alloys.

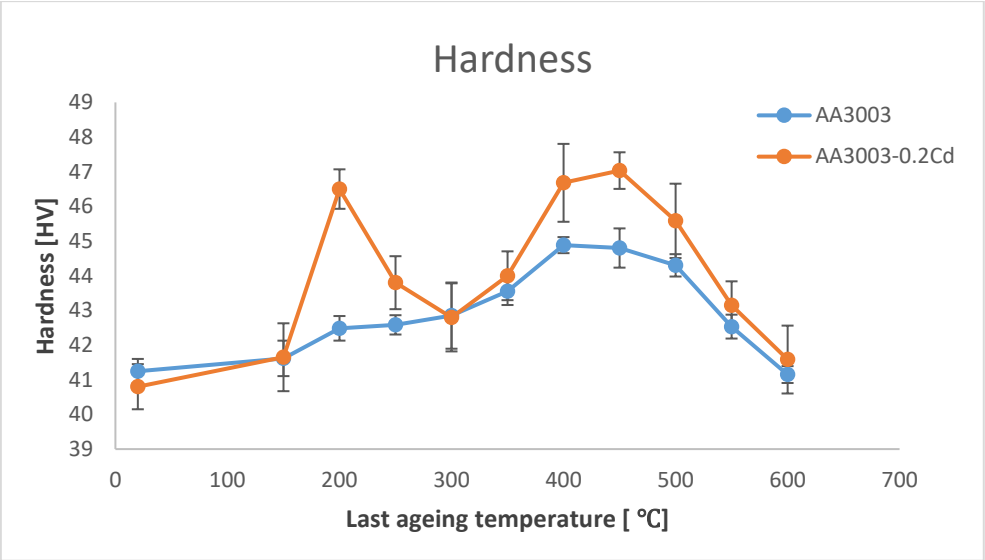

Figure 4.25: Hardness of an AA3003- and a AA3003-0.2Cd Alloy. Results are from an unpublished article by Feng Qian.

The samples from the two peaks at 200 ℃ and 450 ℃ seen in the hardening curve for the AA3003-alloy with Cr in Figure 4.23 were tested with XRF. The samples heat treated at 250 ℃ and 350 ℃ were also tested as reference, and the results from these tests can be found in Table 4.11. We can see that the Mo content varies a lot between the samples, which made the results unreliable. The alloy was therefore remelted, stirred thoroughly, bubbled with argon and cast again. It was also heat treated in the exact same way as the first cast.

Table 4.11: Chemical content of four of the samples from the first cast of the Cr containing AA3003 alloy. The results are averaged from three measurements on each sample.

Sample	Si	Mn	Cu	Mg	Zn	Fe	Ti	Cr	Zr	Cd	Mo
200	0.94	1.04	0.067	<0.096	0.02	0.58	0.025	0.22	0.014	0.16	0.18
250	0.98	1.15	0.06	<0.096	0.017	0.56	0.03	0.29	0.015	0.15	0.32
350	0.62	1.06	0.065	<0.096	0.021	0.58	0.027	0.24	0.014	0.16	0.19
450	0.94	1.12	0.061	<0.097	0.018	0.59	0.027	0.26	0.014	0.15	0.25

The chemical content of four samples heat treated at 200 ℃, 250 ℃, 350 ℃ and 450 ℃ were tested for the second cast of the AA3003-Mo-Cd alloy, from which the results are in Table 4.12. From this table, it is obvious that the second cast is more homogeneous than the first, in particularly when examining the Mo content. The Si content varies a lot, both between samples and casts, but these variations are probably due to SiC impurities from the grinding, and therefore not important with regard to hardness or electrical conductivity. It is also notable that the second cast has more Mg and Zr than the first. It also has generally less Mo.

Table 4.12: Chemical content of four of the samples from the second cast of the Cr containing AA3003 alloy. The results are averaged from three measurements on each sample

Sample	Si	Mn	Cu	Mg	Zn	Fe	Ti	Cr	Zr	Cd	Mo
200	0.22	1.05	0.065	<0.16	0.018	0.58	0.027	0.21	0.015	0.16	0.18
250	0.68	1.01	0.062	<0.16	0.02	0.55	0.029	0.21	0.016	0.15	0.18
350	1.77	1.03	0.067	<0.17	0.018	0.6	0.029	0.22	0.016	0.16	0.18
450	0.34	1.02	0.07	<0.16	0.02	0.56	0.03	0.21	0.020	0.15	0.18

In Figure 4.26 and Figure 4.27 the hardness and electrical conductivity of the isochronally heated samples can be seen compared to the same results from the first cast. The second cast is generally softer than the first, but the trends are the same, meaning that the inhomogeneity of the first cast seems to have an insignificant effect on the results.

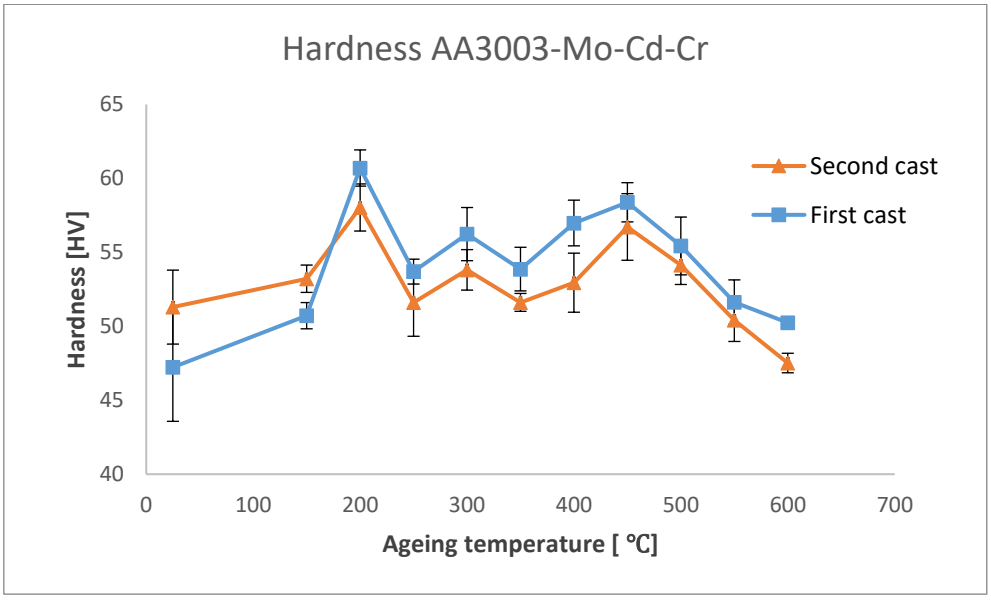

Figure 4.26: Hardness of the two casts of AA3003-Mo-Cd-Cr. The inhomogeneity of the first cast seems to have an insignificant effect on the hardness, as the results are similar.

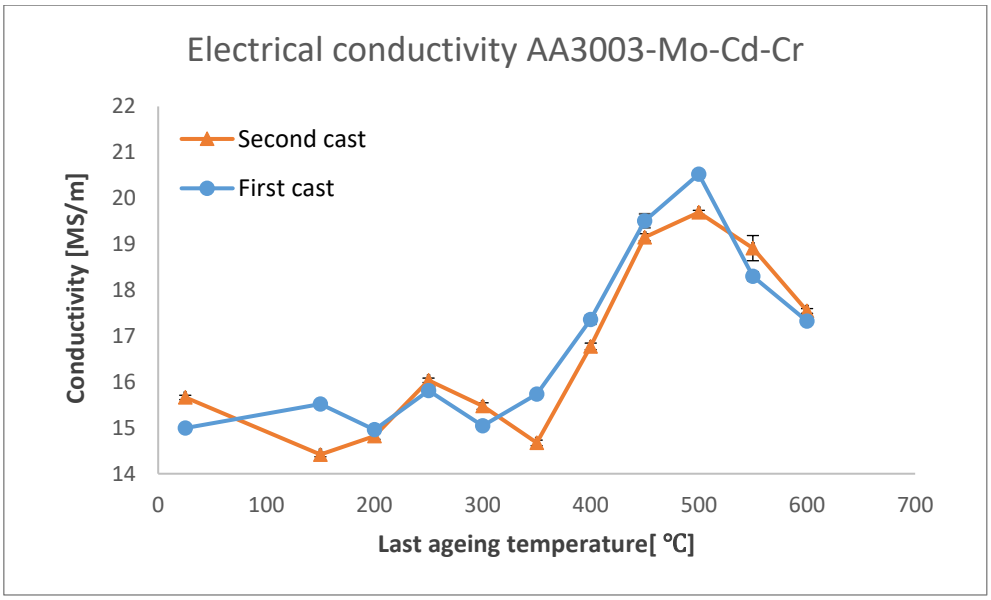

Figure 4.27: Electrical conductivity of the two casts of AA3003-Mo-Cd-Cr. The inhomogeneity of the first cast seems to have insignificant effect on the conductivity, as the results are similar.

4.5.2 After an isothermal heat treatment at 185 ℃

The AA3003-Mo-Cd-Cr alloy was aged at 185 ℃, and a hardness curve was made, which can be seen in Figure 4.28. The hardness did not reach the same peak as we can see at 200 ℃ in Figure 4.26, but it increases by around 10HV, and it keeps a stable hardness throughout the experiment to 100 hours. The conductivity is stable throughout the ageing process.

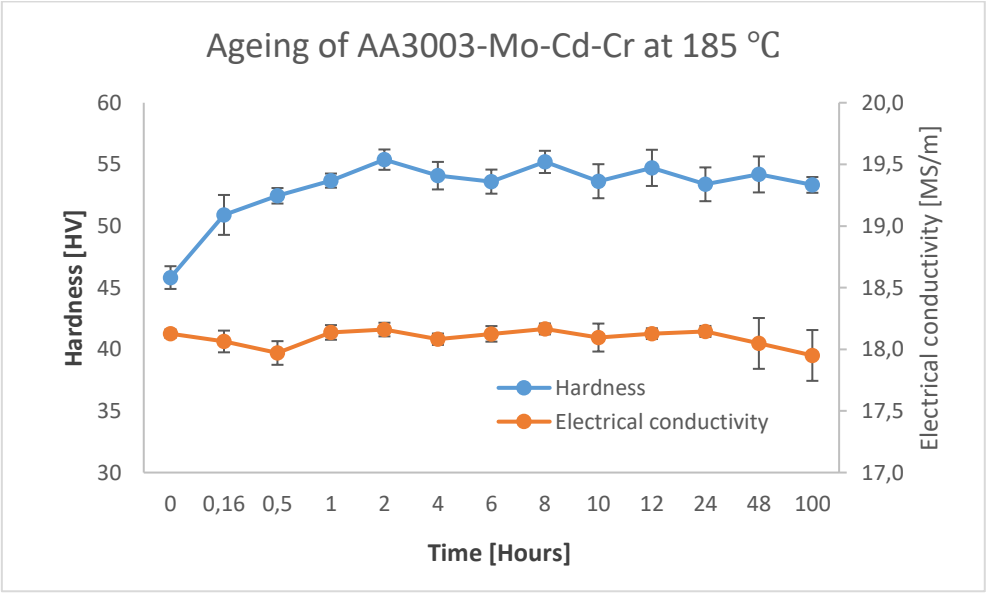

Figure 4.28: Isothermal hardening of the AA3003-Mo-Cd-Cr alloy at 185 ℃.

4.6 Microstructural analysis in an AA3003-Mo-Cd alloy

4.6.1 Solidification structure

Figure 4.29 is an overview image of the solidification structure, while Figure 4.30 provides more details and show the EDS spots, which, along with Table 4.13, gives the results of the EDS analysis, which suggests that the larger, brighter particles could be $Al_{12}(Mn,Mo)$, while the particles on the grain boundaries can be $Al_6(Fe,Mn)$ or Al(Mn,Fe)Si, depending on whether or not they contain Si. Full EDS results for both the as cast samples and the 450 °C sample van be found in Appendix B: Full EDS results.

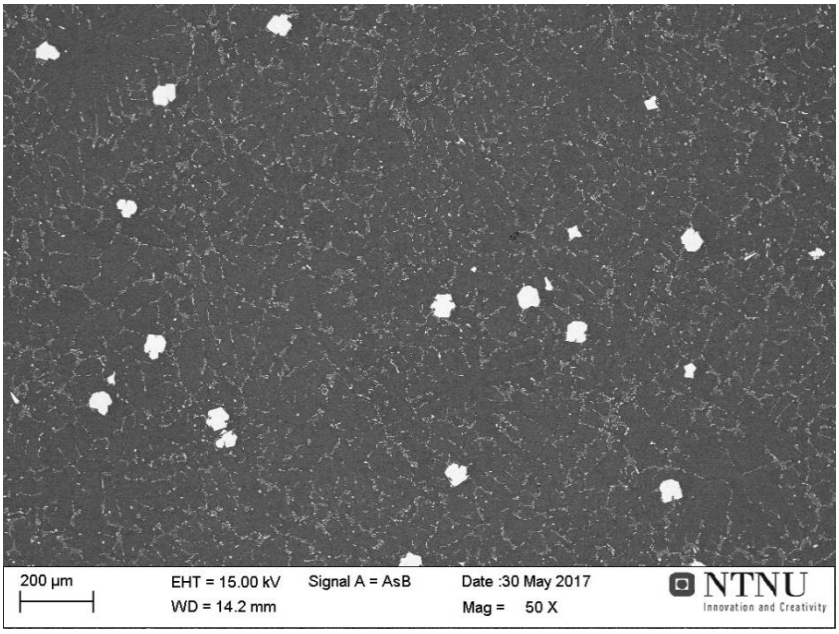

Figure 4.29: Overview image from the solidification structure of the AA3003-Mo-Cd sample showing larger, Mo-containing particles and Fe- and Mn-containing particles at the grain boundaries.

a) b)

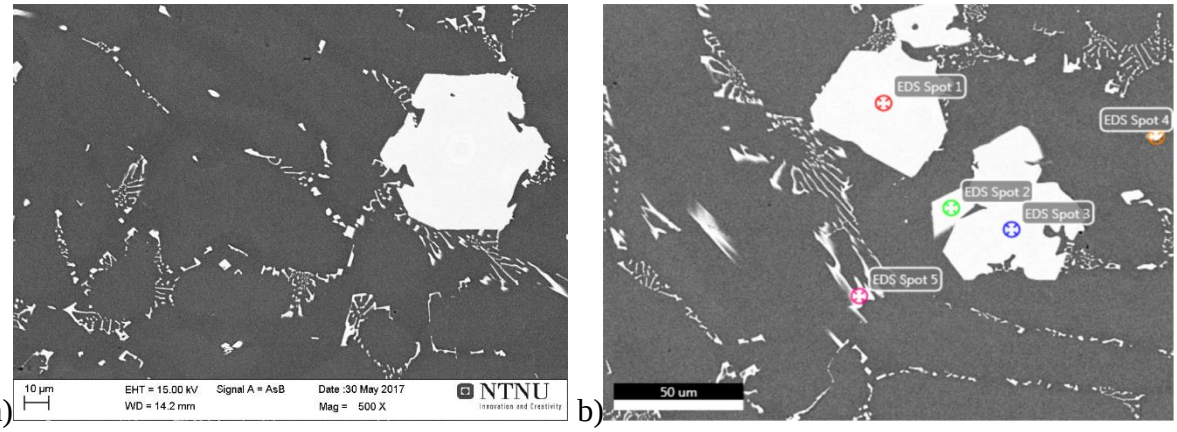

Figure 4.30: a) An image showing the details of the Fe- and Mn-containing particles on the grain boundaries. b) The EDS area for the as cast sample of the AA3003-Mo-Cd alloy.

Table 4.13 Results from the EDS analysis on the as cast sample of the AA3003-Mo-Cd alloy. The content is balanced with Al.

Spot	Mn [Wt %]	Mo [Wt %]	Fe [Wt %]	Si [Wt %]
1	6.0	9.7	-	-
2	6.7	8.7	-	-
3	7.2	8.2	-	-
4	8.7	-	21.4	14.0
5	8.9	-	14.9	-

4.6.2 After continuous heating

Figure 4.31 through Figure 4.33 show SEM images from the AA3003-Mo-Cd samples heated to 350 ℃, 450 ℃ and 550 ℃, respectively. These are obtained using the backscattered electron signal. In the as cast and 350 ℃ samples the presumed Al_{12}(Mn,Mo) particles are much larger than in the samples heated to 450 ℃ and 550 ℃. This might indicate that the Mo or other elements in the particle diffuses out in the matrix at these temperatures. The size of the particles is, however, similar in the 450 ℃ and 550 ℃ samples, making it reasonable to believe that the matrix and other particles are saturated with Mo before 450 ℃ is reached. The other particles seen are dispersed along the grain boundaries, and their size decreases with increasing temperature. They go from being coarse particles at 350 ℃ to being finely dispersed at 550 ℃.

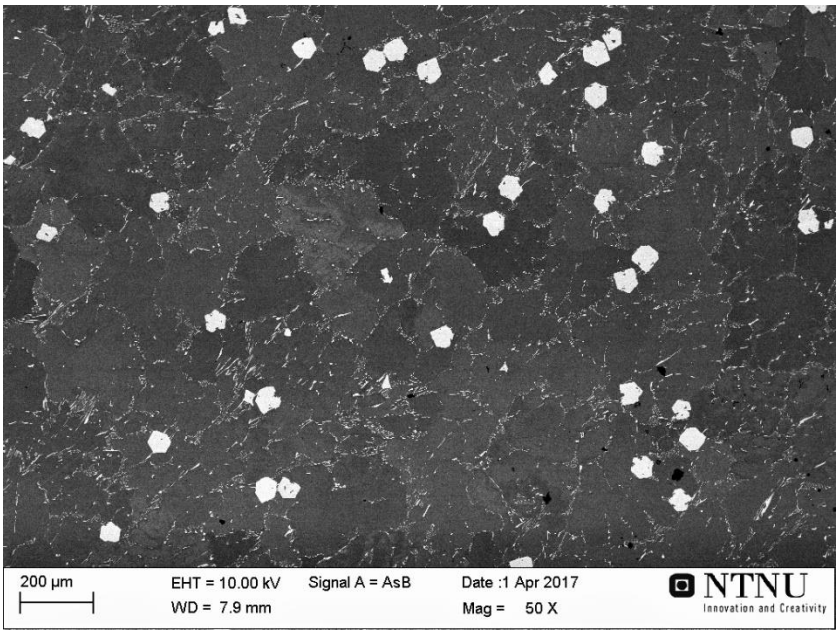

Figure 4.31: Overview image from the AA3003-Mo-Cd sample heated to 350 ℃ showing larger, Mo-containing particles and coarse Fe- and Mn-containing particles at the grain boundaries.

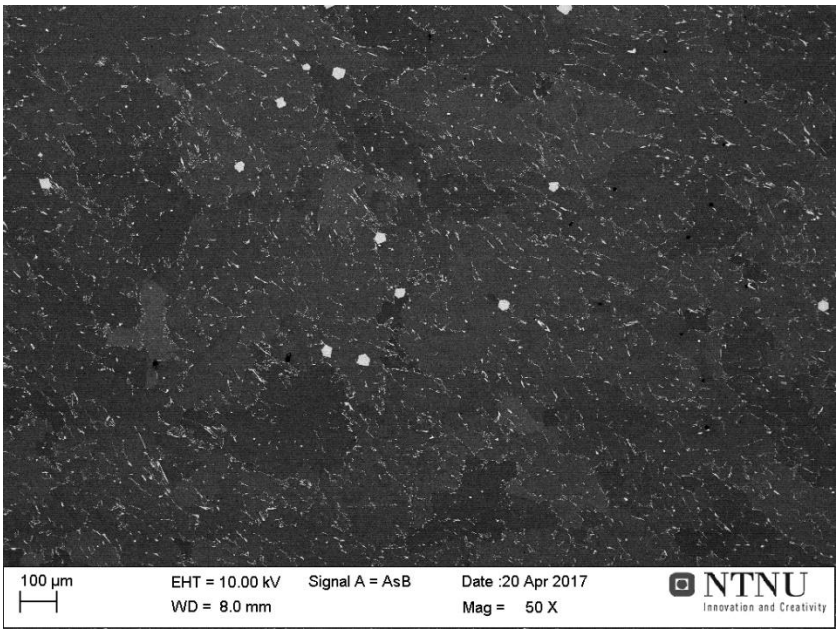

Figure 4.32: Overview image from the AA3003-Mo-Cd sample heated to 450 ℃ showing larger, Mo-containing particles and Fe- and Mn-containing particles at the grain boundaries.

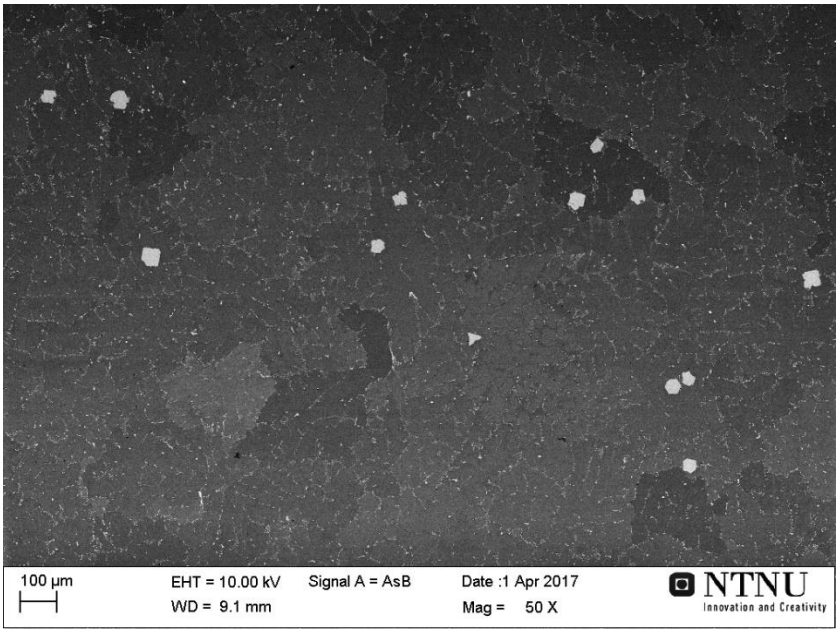

Figure 4.33: Overview image from the AA3003-Mo-Cd sample heated to 550 ℃ showing larger, Mo-containing particles and finely dispersed Fe- and Mn-containing particles at the grain boundaries.

Figure 4.34 and Table 4.14 show the EDS results from the sample heated to 450 ℃. The same large particles presumed to be $Al_{12}(Mn,Mo)$ can be seen in this sample as in the as-cast sample. The grain boundary particles here seem to contain more Fe and less Si than the as cast sample, and the Mn content varies more. Some Cd containing particles are also detected.

a) 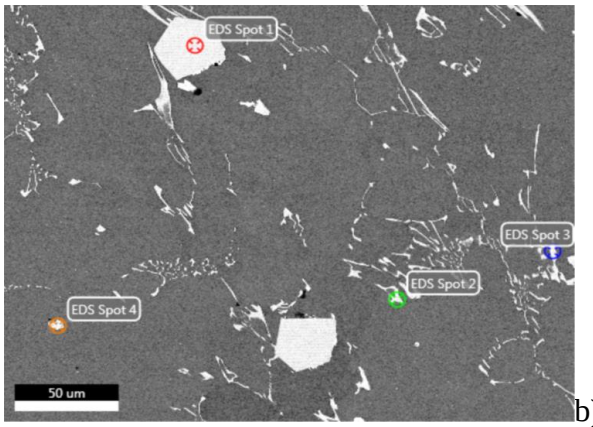

b) 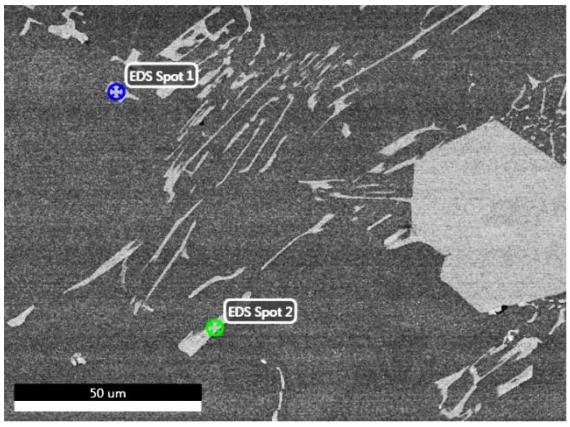

Figure 4.34: EDS area 1 (a) and 2 (b) for the AA3003-Mo-Cd sample aged at 450 ℃.

Table 4.14: Results from the EDS analysis on the sample heated to 450 ℃ of the AA3003-Mo-Cd alloy. The content is balanced with Al.

Spot	Mn[Wt %]	Mo[Wt %]	Fe[Wt %]	Si[Wt %]	Cd[Wt %]
Area 1, spot 1	7.8	8.9	-	-	-
Area 1, spot 2	11.0	-	9.1	2.1	-
Area 1, spot 3	10.6	-	8.6		-
Area 1, spot 4	-	-	7.6	4.3	-
Area 2, spot 1	5.8	-	11.7	-	-
Area 2, spot 2	4.1	-	9.6	2.1	8.8

4.6.3 Investigation of the dispersoids at the hardness peak using a SEM

Figure 4.35 to Figure 4.37 are images of the dispersoids in the AA3003-Mo-Cd sample heated to 450 ℃. These are obtained using the back scattered electron signal with a 20K magnification. In Figure 4.36 the Cd particles are seen as brighter spots, as they are a heavier element than the dispersoids. The dispersoids in this sample are dense and homogeneously dispersed, but a lower density is found near the constituent particles. Figure 4.38 shows an image of an AA3003-0.2Cd sample heated to 450 ℃, for reference. This has the same dispersoid-depleted zones around the constituent particles, and the dispersoids seem to be less homogeneously dispersed.

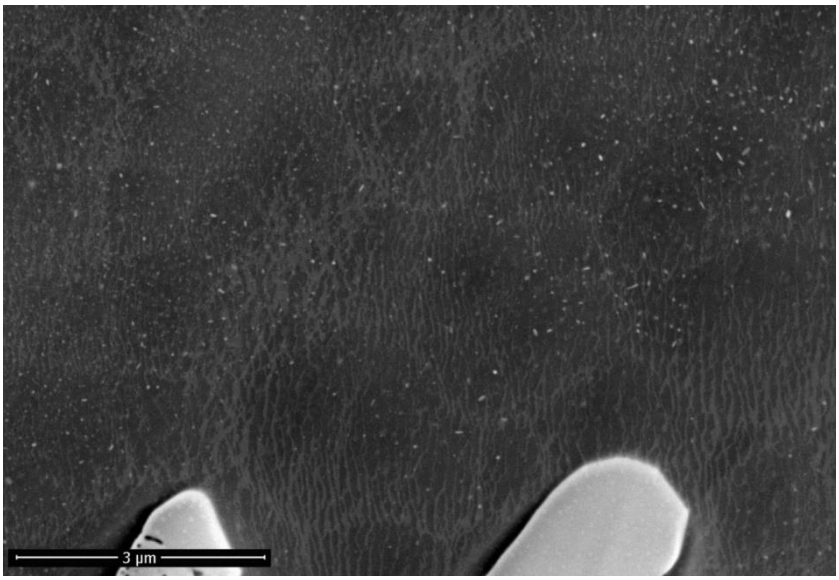

Figure 4.35: A micrograph from the AA3003-Mo-Cd sample heated to 450 °C showing the strengthening dispersoids and the large constituent particles.

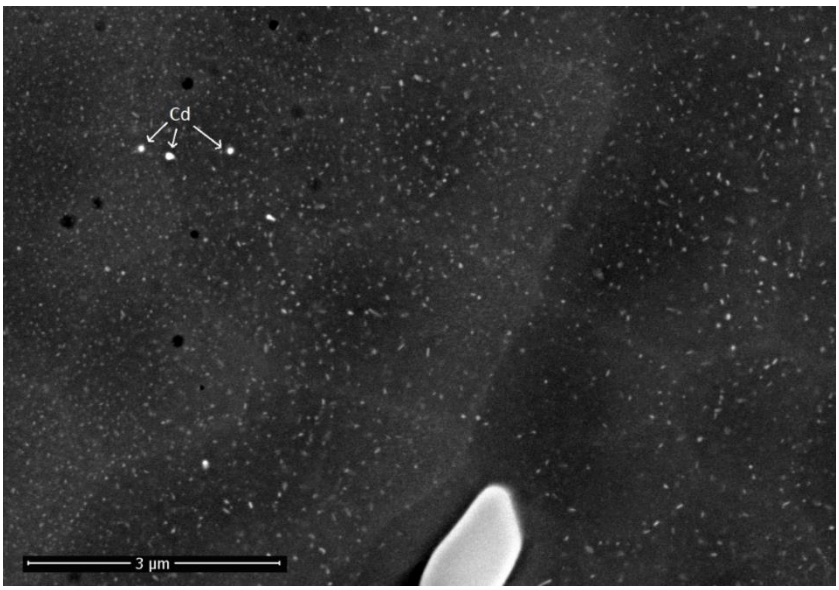

Figure 4.36: A micrograph from the AA3003-Mo-Cd sample heated to 450 °C showing Cd-particles, the strengthening dispersoids and the large constituent particles. The black circles are most likely pores.

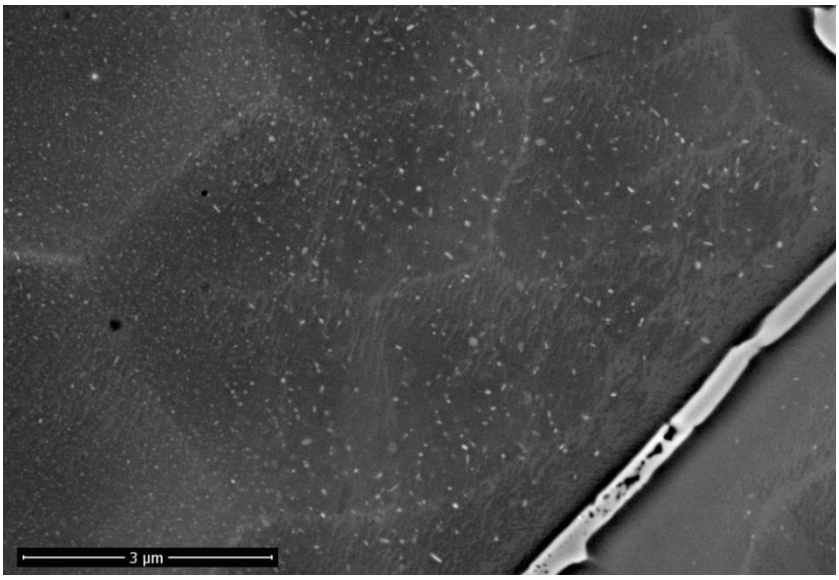

Figure 4.37: A micrograph from the AA3003-Mo-Cd sample heated to 450 °C showing the strengthening dispersoids and the large constituent particles. The black circle is most likely pores.

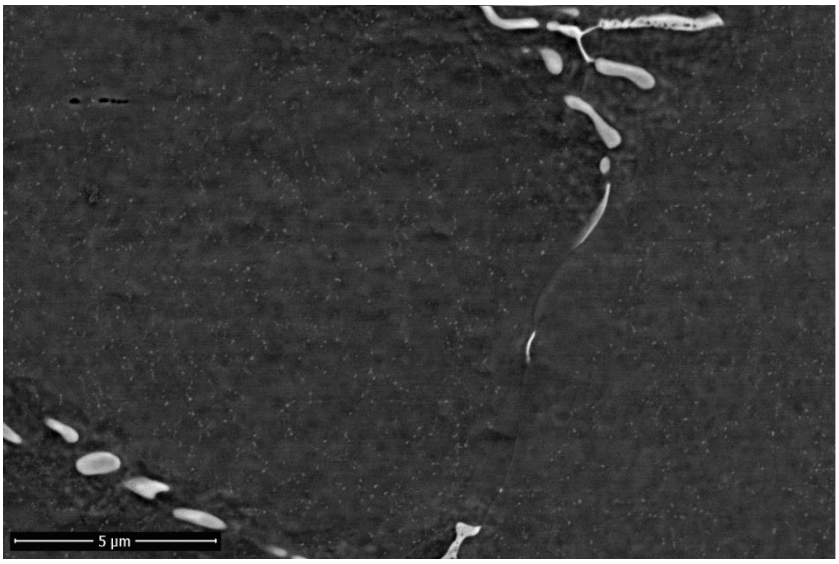

Figure 4.38: A sample of an AA3003-Cd alloy, heated to 450 °C showing the strengthening dispersoids and the large constituent particles.

4.6.4 Investigation of the dispersoids using TEM

The precipitation during heating in the AA3003-Mo-Cd alloy was studied using a TEM, and micrographs of the precipitated dispersoids can be seen in Figure 4.39. Note that different magnifications are used to obtain the images at the different temperatures. In Figure 4.39c a Cd particle can be seen among the dispersoids.

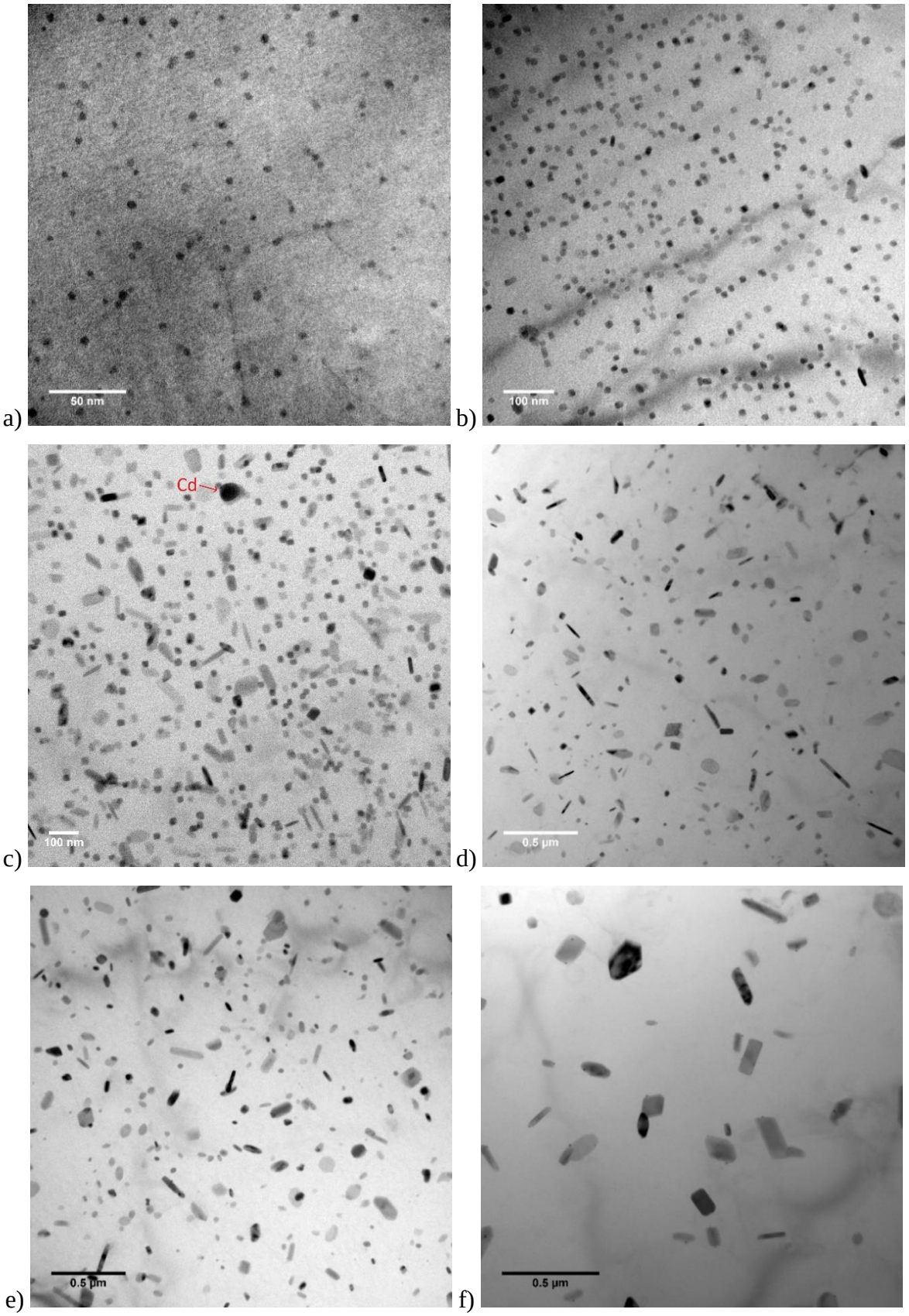

Figure 4.39: TEM morphology of precipitates during heating. a) 350 °C, b) 400 °C, c) 450 °C, d) 500 °C, e) 550 °C and f) 600 °C. Note that the images are obtained using different magnifications. In c) a Cd particle can be observed.

From Figure 4.39 it can be seen that the number density decreases and the size of the dispersoids increases with an increasing temperature. The obtained TEM images were analyzed using the software iSolution DT and the size distributions of the dispersoids in the samples can be found in Figure 4.40. The mean equal circle diameter and number density of them were calculated, and results can be found in Figure 4.41. The number density was calculated by using equation (2.10) and (2.11).

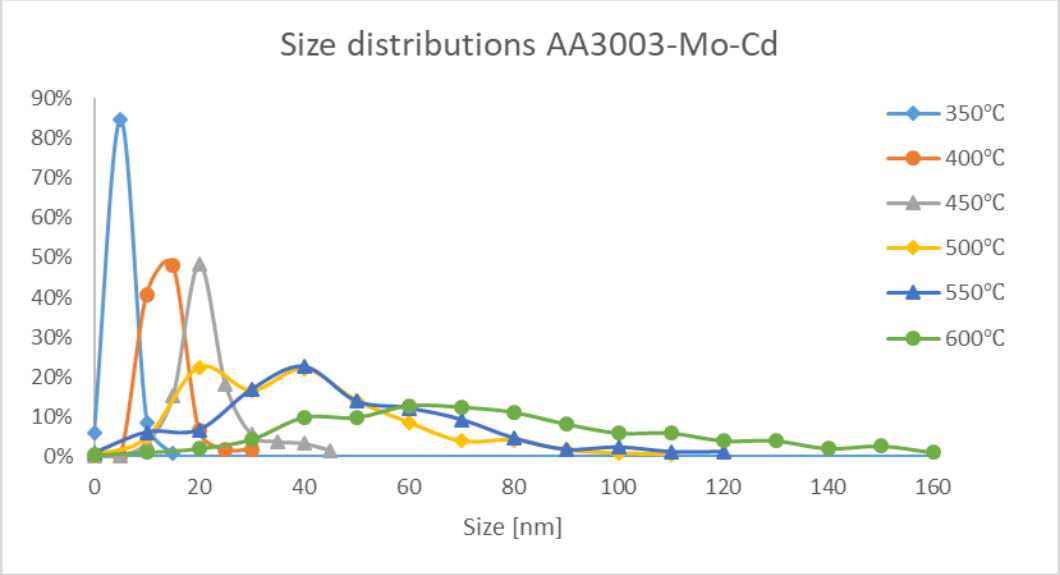

Figure 4.40: Size distributions of the dispersoids in the samples heated to different temperatures.

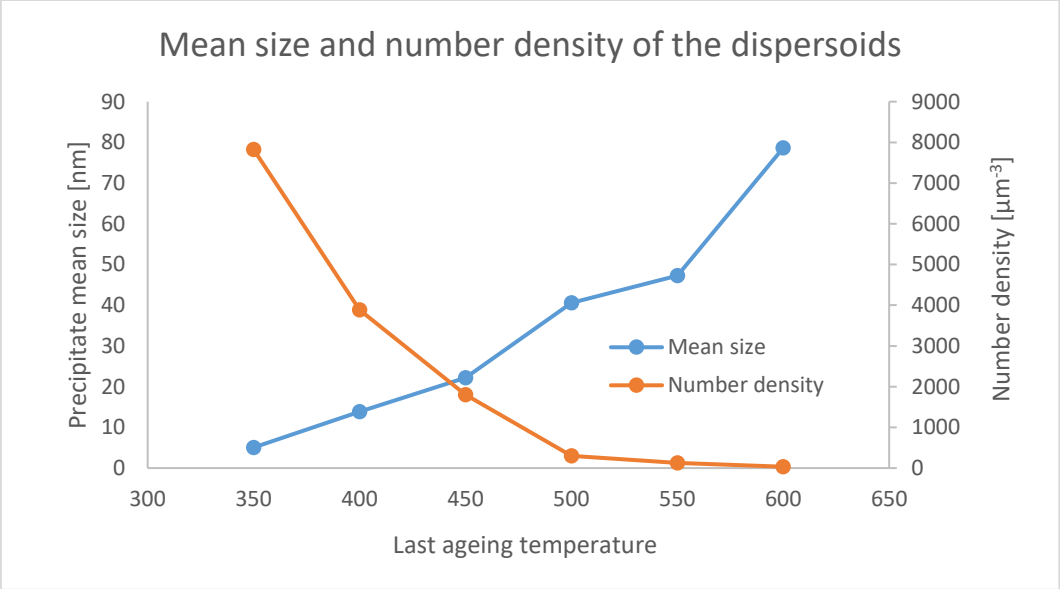

Figure 4.41: Mean equal circle diameter and number density of the strengthening dispersoids

The volume fractions of the dispersoids were calculated, and the results can be found in Table 4.15. It is, however, only calculated for samples heated up to 450 ℃, because at higher temperatures the dispersoids have lost their cubic shape, which is an assumption in the calculations.

Table 4.15: Volume fraction of dispersoids in the samples heated to 350 ℃. 400 ℃ and 450 ℃.

Temperature [℃]	**Volume fraction of dispersoids**
350	0.04 %
400	0.39 %
450	0.74 %

4.6.5 Investigation of Cd precipitates using a TEM

The results from the TEM investigations on the samples heated to 200 ℃ and 300 ℃ can be found in Figure 4.42 and Figure 4.43. It is apparent that the density of Cd precipitates is much higher at 200 ℃ than at 300 ℃, as they have coarsened at 300 ℃. Dispersoids could not be found at either of these temperatures. In Figure 4.44 Cd particles at 350 ℃, 400 ℃ and 450 ℃ can be seen together with the dispersoids. It is apparent that on temperatures of 350 ℃ or more, there is much more dispersoids than Cd particles. With increasing temperatures, the number density of the Cd particles decreases, and the size of them keep increasing. At 500 ℃, no Cd particles are found. The mean size and number density of the Cd precipitates and particles at temperatures from 200 ℃ to 450 ℃ can be seen in Table 4.16.

a) 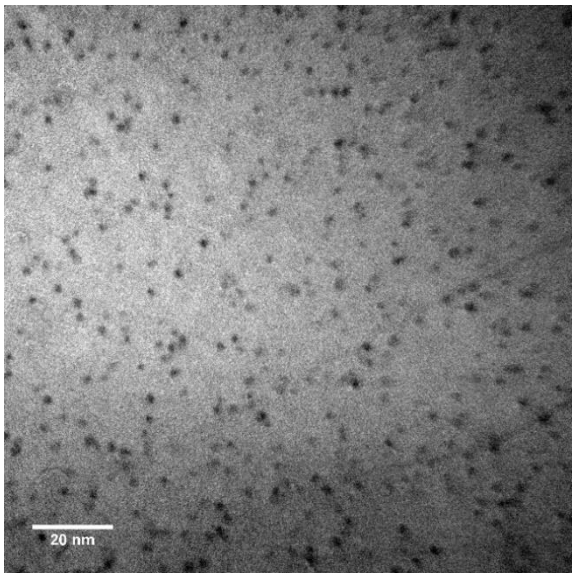

b) 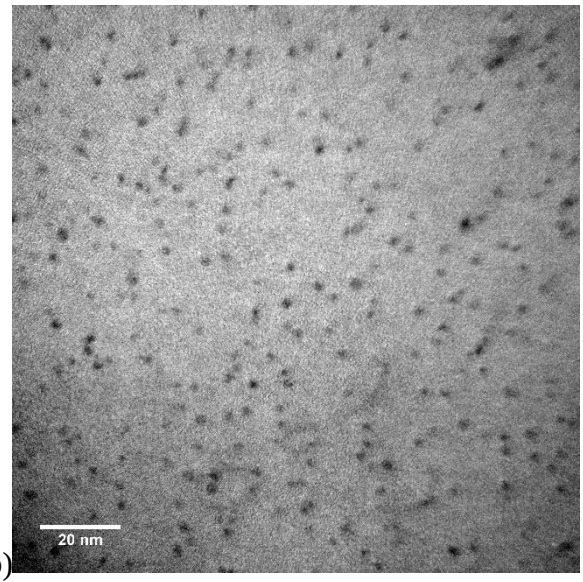

Figure 4.42: TEM micrographs of the AA3003-Mo-Cd alloy heated to 200 ℃ showing a fine dispersion of Cd-precipitates.

a) 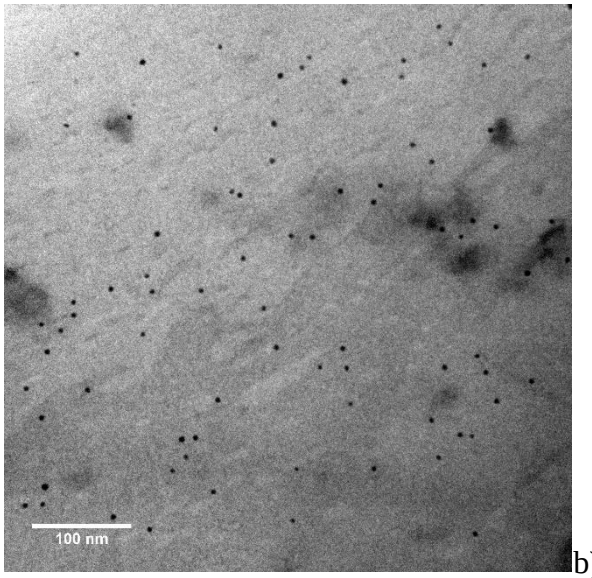

b) 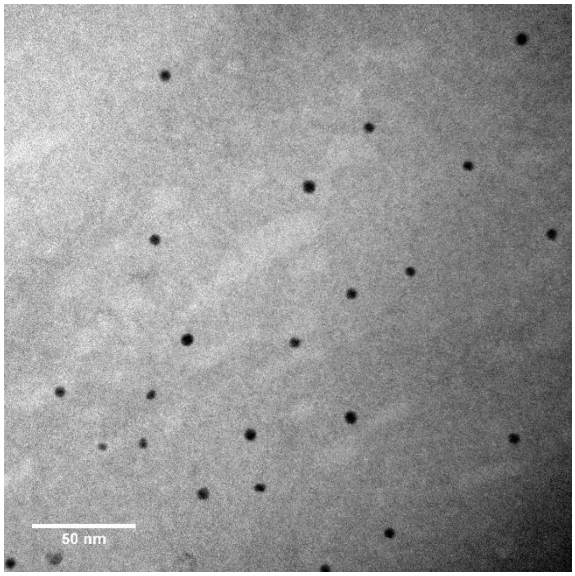

Figure 4.43: TEM micrographs of the AA3003-Mo-Cd alloy heated to 300 ℃.

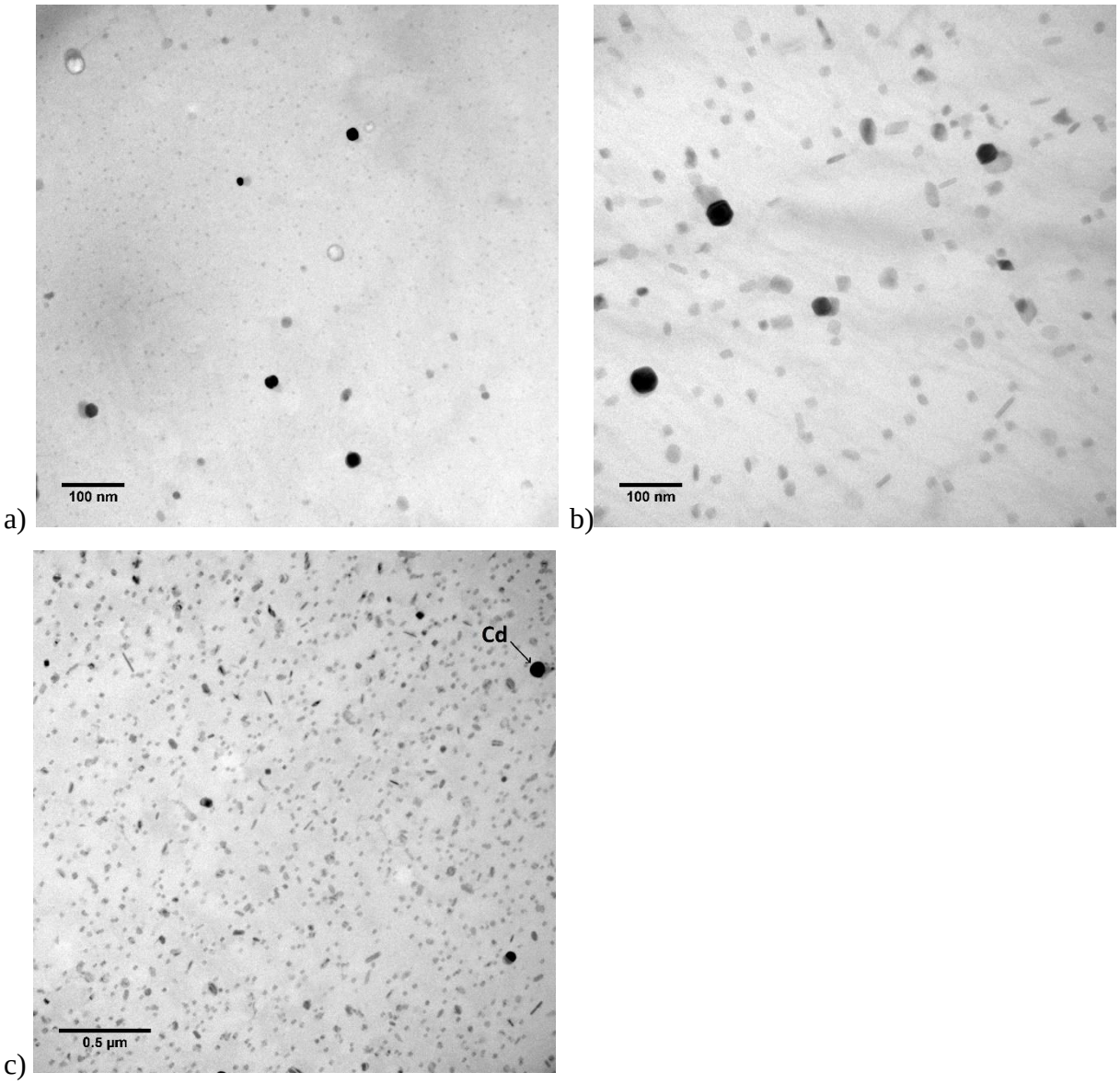

Figure 4.44: TEM micrographs of the samples heated to 350 ℃ (a), 400 ℃ (b) and 450 ℃ (c) from the AA3003-Mo-Cd alloy. These are obtained using different magnifications.

Table 4.16: Size and number density of the Cd particles in the AA3003-Mo-Cd alloy at different temperatures.

Temperature	**Mean diameter [nm]**	**Number Density[µm^{-3}]**
200 ℃	2.00	57 215.07
300 ℃	5.33	1977.64
350 ℃	19.82	56.23
400 ℃	40.70	13.87
450 ℃	70.14	< 9.11

4.7 Strength of the AA3003-Mo-Cd alloy

From the AA3003-Mo-Cd alloy, samples with the last ageing temperature of 200 ℃, 450 ℃ and 600 ℃ were tensile tested, as well as untreated samples. The sample heated to 600 ℃ was held at this temperature for 24 hours, and is to be considered solid solution heat treated. The results from the as cast sample and the 200 ℃ sample are found in Figure 4.45. These samples do not contain any dispersoids. The results from the dispersoid containing samples heated to 450 ℃ and the solid solution heat treated sample heated at 600 ℃ are found in Figure 4.46 along with the results from the as cast samples. Figure 4.47 is a summary of the ultimate tensile strength and yield strength at the different temperatures.

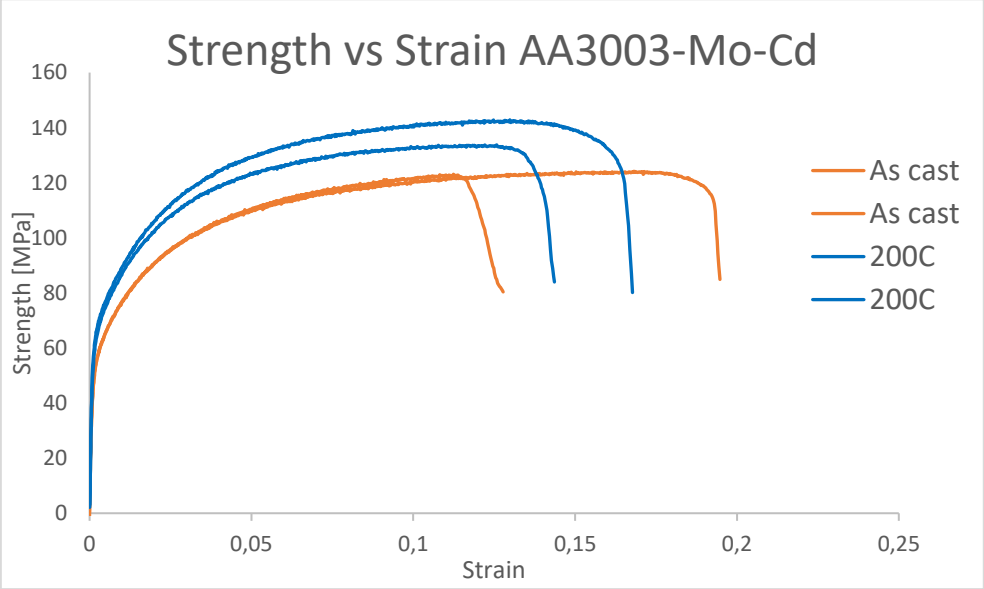

Figure 4.45: Tensile test results from the untreated sample and the sample heated to 200 ℃ from the AA3003-Mo-Cd alloy.

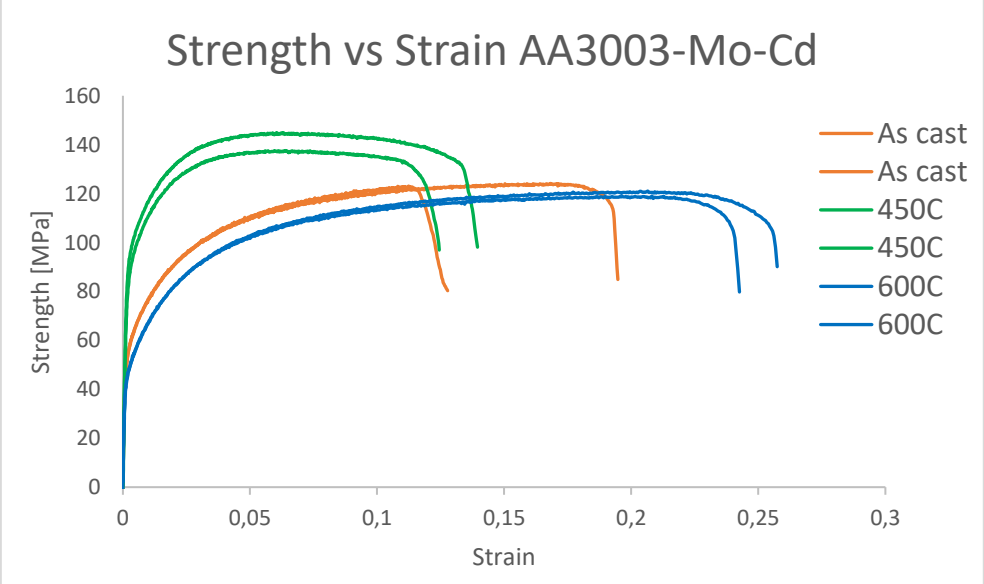

Figure 4.46: Tensile test results from the untreated-, 450 ℃- and 600 ℃ samples of the AA3003-Mo-Cd alloy.

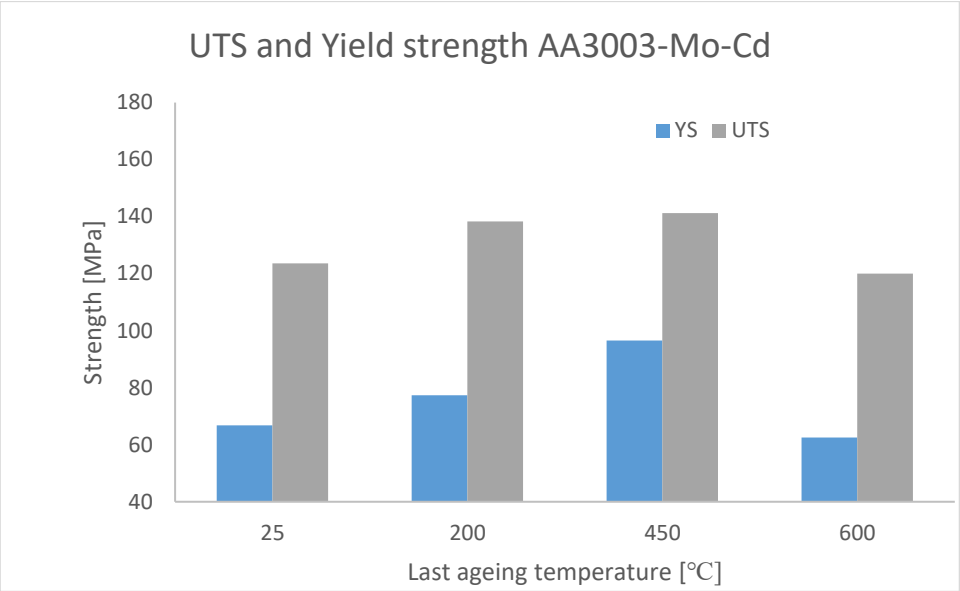

Figure 4.47: Ultimate tensile strength and yield strength at the tested temperatures in the AA3003-Mo-Cd alloy.

4.8 Hardness and electrical conductivity in an AA7050(-Cd) alloy

4.8.1 After a one-step hardening process at 120 °C

The results from the one-step hardening of the AA7050 and AA7050-0.28Cd alloys can be found in Figure 4.48. These show that the Cd has a minimal result on the hardness of the alloy.

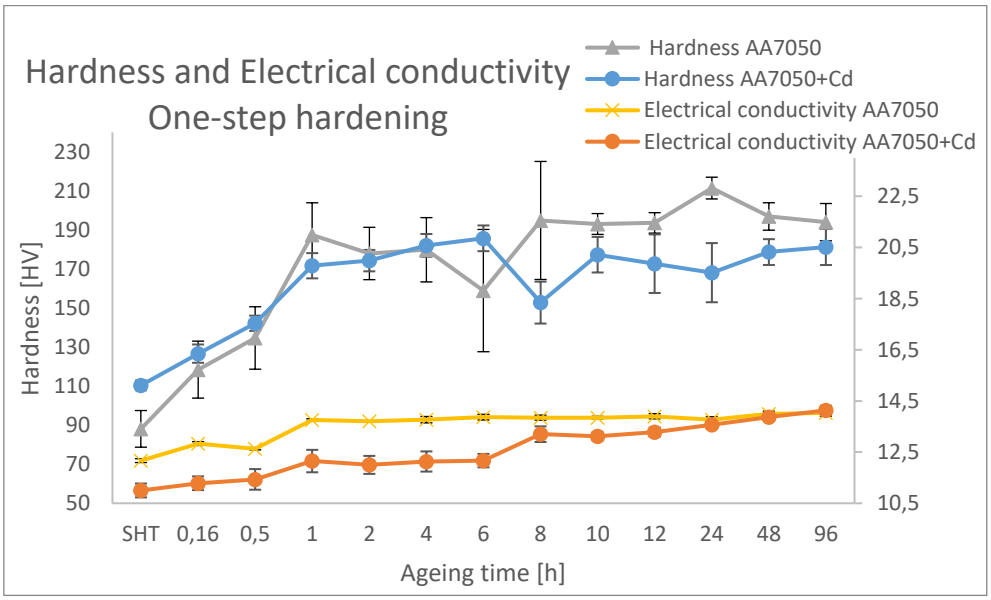

Figure 4.48: Hardness and conductivity in the AA7050 alloy heat treated at 120 °C for up to 96 hours. The first measurement is from a solid solution heat treated sample.

4.8.2 After a two-step hardening process at 120 ℃ and 165 ℃.

The results from the two-step hardening of the AA7050 and AA7050-0.28Cd alloys are found in Figure 4.49. These confirm that the Cd has a minimal result on the hardness of the alloy.

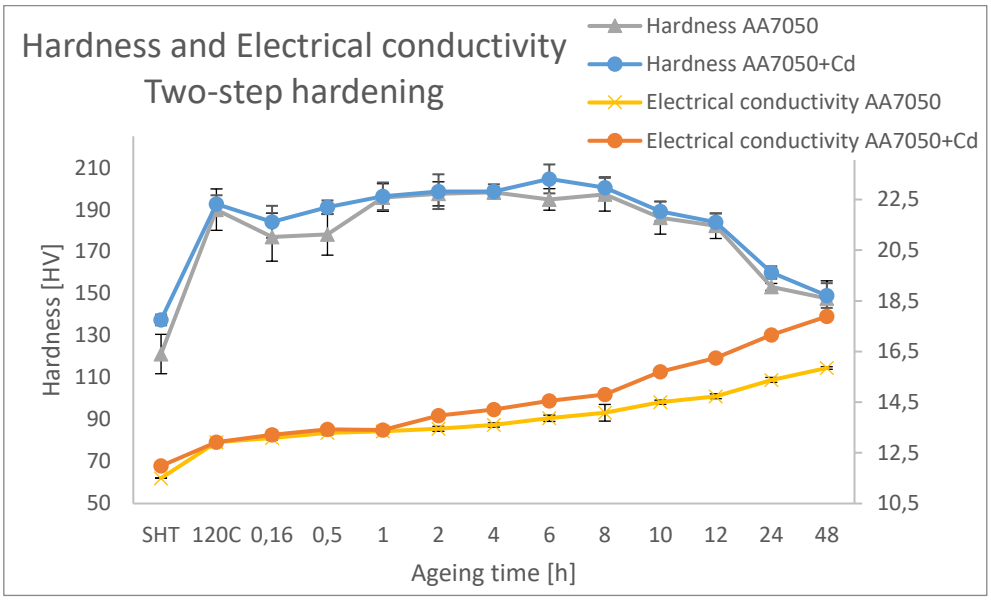

Figure 4.49 Hardness and conductivity in the AA7050 alloy heat treated at 120 ℃ for 6 hours and then 165 ℃ for up to 48 hours. The first measurement is from a solid solution heat treated sample.

Chapter 5: Discussion

5.1 Al-Zr(-Cd)

5.1.1 Hardness and electrical conductivity

Both Cd-containing alloys are much harder than the alloys without Cd after SHT. It is also worth noting that although the former contains more than twice as much Zr, the Al-0.26Zr-0.23Cd and Al-0.12Zr-0.29Cd alloys are within the same hardness range. However, as the Al-0.23Zr alloy is harder than the Al-0.16Zr and Al-0.18Zr alloys it is evident that the expected hardness increase from Zr is present. It appears that the small difference in Cd is compensating for the reduction in Zr, and that the hardness contribution from the Cd is high. All results from the hardness measurements of the five alloys after the SHT are found in Table 4.2.

Figure 4.1 presents the hardness of the five different Al-Zr(-Cd) alloys. The first thing to notice is that the two Cd-containing alloys have hardness peaks at 200 ℃, while the other alloys only have a hardness peak at a higher temperature (400 ℃ - 550 ℃). Therefore, one can assume that the first peak is only caused by the addition of Cd, and the second is controlled by both the Cd and the Zr content. This is also confirmed as the maximum hardness of the higher temperature peaks increase with an increasing Zr content. Cd has a much higher diffusivity in Al than Zr, allowing it to precipitate out earlier, which explains why the Cd-containing alloys have the low temperature peak. In the Al-0.12Zr-0.29Cd alloy there is no clear hardness peak at the higher temperature, but the hardening contribution from the Zr is most likely highest at 400 ℃. This is because the hardness at this temperature is significantly higher than what can be expected from the hardness measured at 350 ℃ and 450 ℃, but as the Zr content is very low its strengthening contribution camouflaged by the decreasing strengthening contribution of the Cd. 400 ℃ will therefore be considered the second hardness peak of the Al-0.12Zr-0.29Cd. This hardness peak is higher than any of the Al-Zr alloys, despite having significantly less Zr. This indicates that the Zr and Cd have a synergetic effect, even at these temperatures. The hardness peak of the Al-0.26Zr-0.23Cd is also substantially higher than the peak of the Al-0.23Zr alloy, even though they have comparable amounts of Zr. This confirms that the Cd plays a key role in determining the hardness of the alloy, and indicates that strengthening precipitates, which are thought to be $Al_3(Zr_xCd_{1-x})$, are more effective at hardening the alloy than Al_3Zr precipitates.

From Figure 4.2 it is clear that the Zr has a much higher influence on the conductivity than the Cd, as the two samples with the most Zr has a much lower conductivity than the others before

heating. This is also in line with the theory, as Zeng et al. (11) classifies Cd as an element with low impact on the electrical conductivity in Al, while Zr is classified as having a high impact. The Al-0.23Zr and Al-0.26Zr-0.23Cd alloys have very similar Zr contents, but the Cd containing alloy has a higher electrical conductivity, especially at temperatures of 350 ℃ and higher, which seems to be the temperature where the strengthening precipitates are precipitated. The fact that the Cd containing alloy has a higher electrical conductivity than the pure Al-Zr alloy on these temperatures might indicate that a higher volume fraction of dispersoids is precipitated with additions of Cd. This trend is also confirmed when comparing the Al-0.12Zr-0.29Cd alloy to the Al-0.16Zr alloy.

All the alloys have a conductivity peak somewhere between 400 ℃ and 550 ℃. The peak is where most of the Zr has precipitated out as dispersoids, and is neither in solid solution nor as coarsened particles that would make the resistance of the alloy increase. Cd seems to lower the temperature of the peak, which indicates that the precipitation rate is higher with additions of Cd, as the maximum amount of dispersoids is reached earlier in the heat treatment. This points to Cd lowering the nucleation energy in the alloy.

From Figure 4.1 and Figure 4.2 one can see that the conductivity peaks in the Al-0.23Zr and Al-0.26Zr-0.23Cd alloys coincide well with the hardness peak seen at the same temperature. The Al-0.12Zr-0.29Cd alloy does not have a hardness peak in this area, as the Zr content is very low. It does, however, seem like the hardness contribution from the Zr is largest at 400 ℃, which also is where the electrical conductivity peak is. For the Al-0.16Zr and Al-0.18Zr alloys, the peak in electrical conductivity is 50 ℃ after the hardness peak. This indicates that a lower amount of Zr is in solid solution 50 ℃ after the hardness peak, but as the alloy has become softer, the dispersoids might have started to coarsen, making them contribute less to the hardness. The first hardness peaks in the Al-Zr-Cd alloys is not reflected in the conductivity results at all. This is most likely because the solubility of Cd in aluminium at these temperatures is so small that it will not affect the electrical conductivity much, in addition to Cd having a low impact.

Figure 4.3 and Figure 4.4 shows the hardness and electrical conductivity results from the slower heat treatment respectively. During this heat treatment, the alloys have been heated slower at a heating rate of 25℃/h, and they were held at the temperature steps for three hours, as opposed

to one hour in the fast heat treatment. This should have given the dispersoids more time to nucleate and grow, leading to an increased hardness compared to the first heat treatment. For the second hardness peak of the Al-0.26Zr-0.23Cd and Al-0.23Zr alloys, this is confirmed to be true, as the samples subjected to the slower heat treatment are harder compared to the same temperatures by the fast heat treatment. There is also an increase in the electrical conductivity peak with the slower treatment, which indicates that more of the alloying elements have precipitated. However, for the three alloys with less Zr, a higher maximum hardness is seen during the faster treatment, even though the electrical conductivity increased more rapidly in the slower treatment. This is most likely because a higher volume fraction has precipitated out, but because the dispersoids have grown, the number density has decreased so much that the hardness also has decreased. The hardness peak in the Al-0.26Zr-0.23Cd alloy at 200 ℃ seem to not be affected by the decrease in heating rate.

The exact same heat treatment as the one with the slowest heating rate used in this thesis has been performed on Al-0.06at%Zr and Al-0.06at%Zr-0.06at%Sc alloys by K. Knipling et al. (39). The maximum hardness of the Al-Zr-Sc alloy in their paper is found at 425 ℃ and is 618 MPa, while the hardness peak of the Al-Zr alloy is 295 MPa at 475 ℃. Due to their composition, these two alloys are most comparable to the Al-0.26Zr-0.29Cd and Al-0.23Zr alloys from this thesis. The peak hardness of the Al-0.23Zr alloy is, however, much higher than in the Al-0.06at%Zr alloy, as can be seen in Table 5.1. It is also apparent that the Al-Zr-Sc alloy has a much higher maximum hardness than the Al-0.26Zr-0.29Cd alloy, even though the Zr content is lower. This indicates that the Sc is more effective at hardening the alloy than Cd. The maximum hardness in the Sc-containing alloys are also achieved at lower temperatures than in the Cd-containing alloys, indicating that Sc accelerates the precipitation kinetics more than Cd.

Table 5.1: Chemical content, peak hardness, temperature at peak hardness and change in conductivity from the as cast sample to the sample with maximum hardness for various alloys. All alloys are heated with a heating rate of 25 ℃/h, in steps of 25 ℃ and 3 hours holding time on each step.

Wt %	**At %**	**Peak hardness [MPa]**	**Temperature at peak hardness**	**Change in conductivity**
Al-0.18Zr	Al-0.053Zr	276	450 ℃	1.7 MS/m
Al-0.23Zr	Al-0.068Zr	431	450 ℃	2.5 MS/m
Al-0.26Zr-0.23Cd	Al-0.073Zr-0.055Cd	494	450 ℃	3.7MS/m
Al-0.12Zr-0.20Cd	Al-0.036Zr-0.070Cd	302	500 ℃	1.8 MS/m
-	Al-0.06Zr	295	475 ℃	2.4 MS/m
-	Al-0.06Zr-0.06Sc	618	425 ℃	4.9 MS/m
-	Al-0.1Zr	420	425 – 450 ℃	3.6 MS/m
-	Al-0.1Zr-0.1Sc	782	400 ℃	6.8 MS/m

K. Knipling et al. (14) have also investigated Al-0.1at%Zr and Al-0.1at%Zr-0.1at%Sc alloys with the same ageing method. As can be seen from Table 5.1, the concentrations of both Zr and Cd in the alloys used in the present thesis are lower than 0.1at%. The Al-0.23Zr and Al-0.26Zr-0.29Cd alloys are, however, comparable to the Al-0.1at%Zr and Al-0.1at%Zr-at%0.1Sc alloys, as the solubility of Zr in Al is below 0.23wt% at 600 ℃, and the confirmed concentrations from K. Knipling et al. are lower than the nominal concentrations of 0.1at%. This is also confirmed by the hardness peaks of the Al-0.23wt% Zr and the Al-0.1at% Zr being similar, with 431 MPa and 420 MPa respectively. These peaks are also both at the same temperature, 450 ℃. The Al-Zr-Sc peak, however, is much harder than the Al-Zr-Cd peak, with 780 MPa compared to 494 MPa. These results could be because the Sc concentration is higher than the Cd concentration by 0.035 at%, or it could confirm that the Sc is more effective at hardening the alloy than Cd.

When looking at the electrical conductivity of both the Al-0.1at%Zr-0.1at%Sc and Al-0.06at%Zr-0.06at%Sc alloys investigated by K. Knipling et al. (14, 39), one can see that the Al-Zr-Sc alloy has a larger increase in electrical conductivity than the Al-Zr-Cd. This indicates that a larger volume fraction of Zr is precipitated out in the Sc-containing alloys than in the Cd-containing alloys, meaning that Sc enhances the precipitation more than Cd.

5.1.2 The as cast structure

From Figure 4.5 and Figure 4.7, along with Table 4.5 and Table 4.6 it can be seen that the as cast structure of the Al-0.16 and Al-0.18 alloys are very similar. Both alloys contain platelets with $AlZr_x$ phase containing approximately 47wt% Zr, and clusters of Fe particles where the detected concentration is varying from 10-20wt%. Figure 4.8, however, reveals that the Al-0.23Zr alloy lacks the precipitated $AlZr_x$ phase, and have a higher number of clusters of impurity Fe-particles. This alloy was left in the mould for a while after casting, without water cooling, giving the Fe more time to precipitate out. The lack of $AlZr_x$ platelets is most likely because this alloy was produces using an Al-30Zr master alloy, while the Al-0.16 and Al-0.18 alloys were made using pure Zr. I seems like the master alloy allows for more evenly distributed Zr in the Al-Zr alloy.

Figure 4.10 shows the as cast structure of the Al-26Zr-0.23Cd alloy. The structure shows the same precipitated, Zr-containing platelets as the first two Al-Zr alloys, with around 47 wt% Zr. This alloy does, however, not have the same clusters of Fe-particles. Instead it has precipitated Fe-containing particles on the grain boundaries, that do not look like the particles in the previous alloys. These are thought the be Al_3Fe particles. The Al-0.12Zr-0.29Cd alloy is similar to the Al-0.26Zr-0.23Cd alloy, but it has significantly less particles on the grain boundaries, and it has a high number of spherical clusters of Fe-containing particles. This indicates that the Cd reduces the energy needed to precipitate on the grain boundaries. The reduced number of particles on the grain boundaries compared to the alloy with a higher Zr content could indicates that Zr enhances the precipitation of Fe on the grain boundaries.

In all alloys with $AlZr_x$ platelets it can be observed that they are not dispersed homogeneously. This is probably due to the low diffusivity of Zr, in combination with Zr segregating at the dendrite cores. The Fe particles are, however, relatively homogeneously dispersed, which fits well with the theory, as it has a higher diffusivity.

5.1.3 Analysis of the precipitates during ageing

The Al-0.26Zr-0.23Cd samples heated to 200 ℃ in the fast treatment and 450 ℃ using the slow treatment have been examined using TEM. The hardness of the sample heated to 450 ℃ is almost 10 HV harder compared to the sample heated to 200 ℃. This is explained by the TEM micrographs, as the precipitates in the 450 ℃ sample are double the size of those in the 200 ℃

sample. The 200 °C sample does, however seem to have a higher number density of precipitates. As they form at a relatively low temperature, and the diffusivity of Cd is higher than of Zr, these precipitates are thought to contain mainly Cd, but the exact content cannot be determined without use of a more advanced TEM or atom probe tomography. The precipitation of these precipitates does not lead to a significant increase in the electrical conductivity during precipitation, which further indicates that they do not contain much Zr.

Figure 5.1 shows TEM micrographs of Al-Zr alloys at maximum hardness from the literature, which are comparable to the images obtained in this thesis and repeated in Figure 5.2. From these micrographs it is apparent that the Cd-containing alloys have much finer distribution, and a higher number density of precipitates than the Al-Zr alloys have of Al_3Zr precipitates.

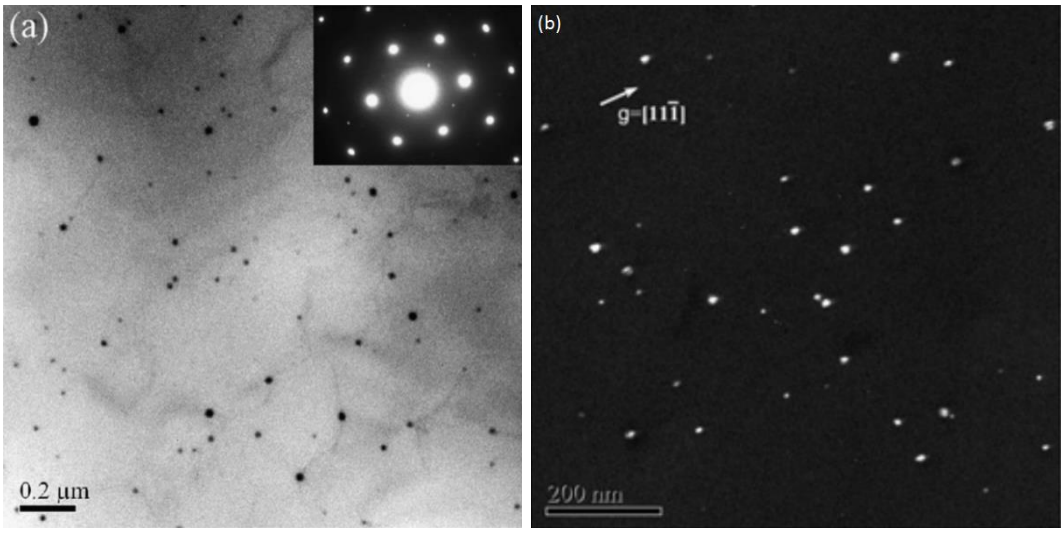

Figure 5.1: (a) is a bright field TEM micrograph of an Al-0.06at%Zr alloy at maximum hardness by H. Li et al. (40). (b) is a dark field TEM micrograph of an aged Al-0.2wt%Zr alloy from Z. Gao et al. (41). Both show the nanosized Al_3Zr precipitates.

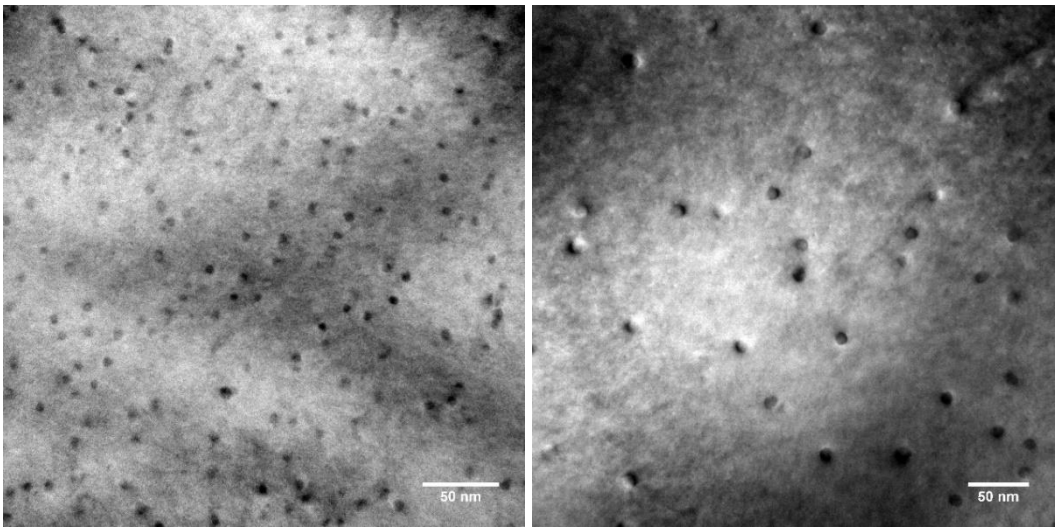

Figure 5.2: Repeated from Figure 4.15. Precipitates in Al-Zr-Cd at 450 ℃.

The diffraction pattern corresponding to the micrographs from the 450 ℃ sample can be found in Figure 4.16. It indicates that the precipitates have a metastable $L1_2$ structure, which fits well with the work of K. Knipling et al. (14), who found that the transformation of $L1_2$ to the equilibrium $D0_{23}$ structure does not happen at lower temperatures than 475 ℃.

5.1.4 Strength

From Figure 4.17, Figure 4.18 and Figure 4.20 it is apparent that in the Al-0.23Zr alloy, the slowest heat treatment, with a heating rate of 25 ℃/h and 3 hours holding time at each step, is more effective at dispersoid strengthening than the faster heat treatment. The tensile strength of the sample subjected to the slowest heat treatment is 31 MPa higher than the tensile strength of the sample heated faster. This is also the case for the yield strength, as the sample subjected to the slow heating treatment has a 28.5 MPa stronger yield strength than the sample subjected to the faster treatment. In the fastest heat treatment, the hardness peak was at 550 ℃, which is a temperature that allows the $L1_2 \rightarrow D0_{23}$ transition of the Al_3Zr precipitates to take place. Assuming that the Zr has sufficient time for diffusion, some of the precipitates may transform into the equilibrium $D0_{23}$ structure which is incoherent and has a smaller strengthening contribution. In the slowest heat treatment, the hardness peak is at 450 ℃, where all precipitates will have a coherent $L1_2$ structure. During this treatment, there is also more time for the Zr to diffuse, and for the precipitates to grow. This leads to larger precipitates that are more efficient at strengthening the alloy.

Figure 4.17, Figure 4.18 and Figure 4.22 contain the yield- and tensile strength results and the stress-strain curves for the high temperature (450 ℃ - 500 ℃) samples of the Al-0.26Zr-0.23Cd alloy. From these results, it is apparent that the slowest heat treatment is most effective at strengthening also this alloy. When looking at the maximum strength samples, which are the 450 ℃ sample subjected to the slowest heating rate for both the Al-0.26Zr-0.23Cd and Al-0.23Zr, alloys, it is evident that only a few MPa separate the yield and tensile strength of them. In these samples, it seems like the precipitates in the Cd containing sample contributes relatively more to the hardness of the alloy than the strength, compared to the Al-Zr alloy. Using the most efficient heat treatment, there is no clear strengthening effect from Cd at this temperature. Looking at the faster heat treatment, however, the Cd-containing alloy is significantly stronger than the Al-Zr alloy. This is because the Zr has had very limited time to diffuse, making the advantage of Cd more obvious.

Samples heated to 200 ℃ of the Al-Zr-Cd alloy was also tested, of which the results can be found in Figure 4.17, Figure 4.18 and Figure 4.21. These samples show an increase in yield strength of 24.5 MPa and 14.6 MPa compared to the as cast sample using the slow and fast heat treatment respectively. The strengthening contribution from the precipitates at this temperature is, therefore, evidently higher in the sample heated with a lower heating rate. The Cd-containing precipitates have probably grown larger using the slow heat treatment, explaining the increased strength contribution. As this is early in the heat treatment, such a clear difference in the strength of the samples subjected to the different treatments suggests that the Cd-containing precipitates at 200 ℃ are very sensitive to temperature and heating rate.

For the Cd-containing alloys, it is apparent that the 200 ℃ samples are stronger than the 450 ℃ samples. These also have a higher strength to hardness ratio for both yield- and tensile strength. This suggests that the Cd precipitates at 200 ℃ have a higher strength contribution than the precipitates precipitated at a higher temperature.

The difference between maximum strength and SHT or as-cast samples is larger in the Al-Zr alloy than the Al-Zr-Cd alloy, meaning that the strengthening precipitates achieved through heat treatment has less strengthening effect on the Cd-containing alloy than the Al-Zr alloy. The Al-Zr-Cd has, however, a higher maximum strength than the Al-Zr alloy, as it is also stronger in the SHT state. It is generally less difference between the yield strength of the

corresponding samples of the two alloys than the tensile strength, suggesting that the heat treatment has a higher influence on the tensile strength than the yield strength.

5.1.5 Summary

The Al-Zr alloys have a hardness peak at 400 °C - 550 °C, which is due to the Al_3Zr precipitates. The precipitation of these commences between 350 °C and 400 °C, which is in line with the literature (14). The hardness of this peak increase with an increasing Zr-content. Additions of Cd create a synergy effect at this peak, increasing the hardness significantly, as the Cd enhances the precipitation, leading to a higher number density of precipitates. When comparing the TEM micrographs from the Al-0.26Zr-0.23Cd alloy with TEM micrographs of Al-Zr alloys from the literature, it is confirmed that the number density is higher in the Cd-containing samples. The tensile tests do, however, show that additions of Cd does not have any clear strengthening effect at these temperatures when the most effective heat treatment is chosen.

Additions of Cd also allows the Al-Zr alloys to have another peak in hardness at 200 °C, which has approximately the same hardness as the previous peak. Along with a lower solubility, Cd has a much higher diffusivity than Zr, allowing it to precipitate out at lower temperatures. These precipitates are shown to be more effective than the higher temperature precipitates at strengthening the alloys. Further investigations with a more advanced TEM or atom probe tomography is needed to know the composition and structure of the precipitates.
Electrical conductivity measurements show that the Cd-containing alloys have a lower conductivity in the as cast and SHT states, but the maximum conductivity is higher in these than in the pure Al-Zr alloys. The conductivity peaks of the Cd-containing alloys are also at lower temperatures than the Al-Zr alloy. These results conclude that the Cd both enhances the precipitation with regard to volume fraction, and that it accelerates the precipitation kinetics. This points to Cd lowering the nucleation energy.

To investigate the effect of different heating rates two heat treatments were used, one with a heating rate of 50 °C/h, steps of 50 °C and a holding time of 1 hour at each step, and one with a heating rate of 25 °C/h, steps of 25 °C and a holding time of 3 hours at each step. The alloys with a lower Zr content seemed to not be affected by the change in heating rate with regard to hardness, but the alloys with a Zr content of 0.23% or higher had both a higher hardening effect and strengthening effect of the slower heat treatment. This is because Zr has a low diffusivity,

and with a slower heat treatment more Zr is allowed to diffuse into the precipitates, leading to a higher volume fraction of precipitates. In the Al-0.26Zr-0.29Cd alloy, the samples subjected to the slower heat treatment reach the maximum hardness at a lower temperature than in the faster treatment, so that the the $L1_2 \rightarrow D0_{23}$ transformation cannot happen. When comparing these heating methods is is obvious that the effect of Cd is larger using the fast heat treatment. This is because the Zr has had less time to diffuse, making the advantage of Cd clearer.

When comparing to the literature it is obvious that additions of Sc are much more effective at hardening Al-Zr alloys than additions of Cd. The $Al_3(Zr_xSc_{1-x})$ precipitates seem to have a much higher hardening contribution than the precipitates in the Cd-containing alloy. The Sc-containing alloys also has a higher volume fraction of precipitates than the Al-Zr-Cd alloy, according to the increase in electrical conductivity from as cast- to maximum hardness samples.

5.2 AA3003-Mo-Cd(-Cr)

5.2.1 Hardness and electrical conductivity

From Figure 4.23 and Figure 4.26 one can observe that both the AA3003-Mo-Cd-Cr and AA3003-Mo-Cd alloys, have two hardness peaks. The first peaks are at 200 ℃ and 250 ℃ respectively, the other peaks are at 450 ℃ in both. The first peaks are confirmed to be due to a large amount of Cd precipitates, while the second peaks are most likely from α-Al(MnFeMo)Si dispersoids. The AA3003-Mo-Cd-Cr alloy is 4.5HV harder than the AA3003-Mo-Cd alloy at the first peak. It is however, also 6HV harder as cast, meaning that the AA3003-Mo-Cd alloy without Cr has had the highest increase in hardness at the first peak, and therefore, the largest hardening effect at the first peak. This indicates that the difference in hardness between the AA3003-Mo-Cd and AA3003-Mo-Cd-Cr at 200 ℃ might be caused by other hardening mechanisms from the Cr. The Cr containing alloy has a more stable hardness, with a higher hardness than the AA3003-Mo-Cd alloy in the 300 ℃ - 350 ℃ region, but the alloy without Cd has a higher hardness at the hardness peak at 450 ℃. The AA3003-Mo-Cd has also had the highest hardening effect in this region. The addition of Cr does not seem to have the desired effect on the AA3003-Mo-Cd alloy, but as the hardness at 200 ℃ is higher in this alloy than in the one without Cr, it was further investigated with isothermal heating at 185 ℃.

Figure 4.24 shows the electrical conductivity of the two AA3003-alloys, which starts to rise at between 300 ℃ and 350 ℃ for both alloys, meaning that this is the temperature the precipitation

of dispersoids commences. The Cr-containing alloy has a conductivity peak at 500 °C, while the alloy without Cr peaks at 450 °C. This is most likely because there are still more alloying elements precipitating out at these temperatures for the Cr-containing alloy, as it contains more alloying elements, making the conductivity increase further with precipitation.

Figure 4.25 shows hardness results from an AA3003 alloy without any additions, and an AA3003 alloy with additions of 0.2wt% Cd. Figure 5.3 shows these results compared with the hardness measurements from the AA3003-Mo-Cd and AA3003-Mo-Cd-Cr alloys from Figure 4.23. It is apparent that the Mo contributes greatly to the strength of the alloys. The first peak in hardness, which is thought to be because of the Cd, is also higher relatively to the as cast sample in the Mo-containing alloys. This might indicate a synergy effect between the Mo and Cd at this temperature. The Cr-containing alloy is harder than the other alloys in the as-cast state, which shows that the Cr contributes to the hardness in the SHT-state. The AA3003-Mo-Cd alloy is not harder than the alloys without Mo in the as cast state, meaning that the hardening contribution of the Mo is most likely only in the form of dispersoids. This indicates that the α-Al(Mn,Fe,Mo)Si dispersoids are more effective at hardening the alloy than the α-Al(Mn,Fe)Si dispersoids in the AA3003 and AA3003-Cd alloys. From Figure 5.3 is can also be seen that the hardness of the AA3003-Mo-Cd alloy is stable from 450 °C to 500 °C, meaning that the addition of Mo keeps the alloy at near peak hardness for a larger temperature interval. This is most likely because the low diffusion rate of Mo in Al delays the coarsening of the dispersoids.

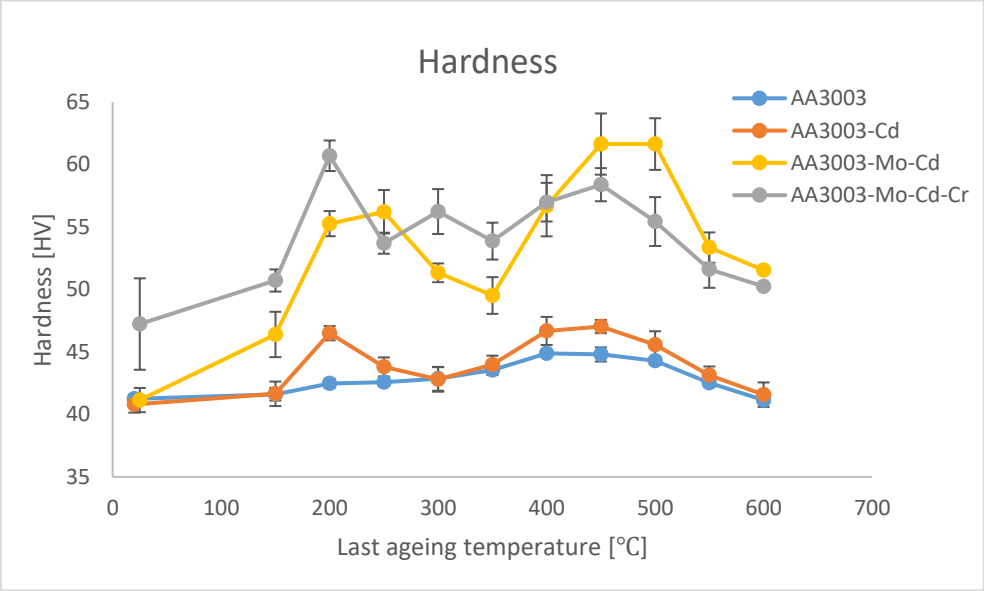

Figure 5.3: Hardness measurements of the following four alloys: AA3003, AA3003-0.2Cd, AA3003-0.15Mo-0.17Cd, AA3003-0.19Mo-0.15Cd-0.2Cr.

The AA3003-Mo-Cd-Cr alloy was isothermally aged at 185 ℃ to try to get the same hardness of 60.7HV that was reached at 200 ℃ in the isochronal experiment. From Figure 4.23 and Figure 4.28 we see that the same hardness is not reached, and that the maximum hardness achieved isothermally at 185 ℃ is 55.4HV, which is the same hardness as the AA3003-Mo-Cd alloy had in the isochronal experiment. The increase in hardness at the peak at 200 ℃ from Cr is most likely because there is still some Cr hardening in solid solution. When held at 200 ℃ for two hours, this hardening effect seems to no longer present. The results from the isothermal treatment is, therefore, assumed to be valid for the AA3003-Mo-Cd alloy as well.

The hardness does, however, increase by almost 10HV when aged at 185 ℃, which is significant for the AA3003 alloy, as is not hardenable without addition of solute elements. It also seems like the hardness produced at 185 ℃ is relatively thermally stable, as the hardness decreases very slowly, and has only decreased marginally, even when held at 185 ℃ for 100 hours. As the hardness peak at 200 ℃ in the isochronal experiment most likely is from Cd precipitates, and Cd has a very little influence on the conductivity of the alloy, the fact that the conductivity stays stable throughout the ageing process is to be expected.

5.2.2 Microstructural analysis

Figure 4.29 shows the as cast microstructure, and Figure 4.31 through Figure 4.33 show the microstructure of the AA3003-Mo-Cd-alloy after heat treatment at a low magnification. From these images, it can be observed that the microstructure contains large hexagonal particles, which are confirmed by EDS to be an Al-Mo phase. As the Mo has precipitated out, these indicate that too much Mo has been added to the alloy. The particles do, however, seem to decrease both in numbers and in size with increasing ageing temperature. On the grain boundaries, other particles can be seen, which are thought to be α-Al(Mn,Fe)Si constituent phase. These also decrease in size during the heating process, making them much finer at 550 ℃ than at 350 ℃. At the same time, one can through TEM analysis see that the strengthening dispersoids are growing. It is therefore reasonable to assume that the elements from the particles visible at low magnification diffuse into the material to form dispersoids.

The strengthening dispersoids in the AA3003-Mo-Cd-alloy can be seen in Figure 4.35 through Figure 4.37, which are SEM images obtained using a higher magnification. From these images,

it seems like the dispersoids are homogeneously dispersed after aging at 450 ℃, except for around the constituent particles, where we have a depleted zone. This might be because certain elements that are needed to nucleate dispersoids, such as Fe and Mn, have diffused into the constituent particles, leaving the area around it depleted. This is likely, as the constituent particles contain Fe and Mn. It could also be that the zone near the particles were depleted of Mn from before the heat treatments, as Mn and Fe containing aluminium alloys tend to have a lot of segregation of Mn in the dendrite arms during solidification. This often lead to a strong Mn depletion on the periphery of the dendrite arms, making it hard to form dispersoids in these zones, as Mn has a very low diffusivity. This could be a problem, as a structure that is not uniform may influence the recrystallization kinetics and texture during rolling or other mechanical treatments(10).

From Figure 4.36 it is evident that the dispersoids are homogeneously dispersed independent of the Cd particles. It is proposed that the Cd particles provide heterogeneous nucleation sites for the dispersoids, meaning that dispersoids should be in the vicinity of them. As can be seen in Table 4.16, Cd precipitates are present in the samples with a last ageing temperature of 200 ℃ - 450 ℃, but at higher temperatures they seem to have mostly dissolved. The particles grow rapidly, and the number density decreases dramatically after 300 ℃. The number density of the particles in very high at 200 ℃, which explains the increase in hardness at this temperature.

From the TEM micrographs in Figure 4.39 the evolution of the dispersoids in the AA3003-Mo-Cd alloy during heating can be seen. A large number of precipitates are seen already at 350 ℃, which fits well with the electrical conductivity measurements seen in Figure 4.24, as they indicate that precipitation starts between 300 ℃ and 350 ℃. From Figure 4.43 one can see that there is no dispersoids present in the alloy at 300 ℃. It is apparent from the images in Figure 4.39 that the dispersoids grow with the increase in temperature, which is as expected. From only a few nanometers at 350 ℃, they grow to be almost 80 nm at 600 ℃. At 350 ℃ and 400 ℃ they are approximately cubic, while at higher temperatures they have grown to form more plate like shapes. According to Y.J. Li et al. this is due to the low interface energy of the habit plane, making the dispersoid grow in directions parallel to this plane (7).

The AA3003 alloy has been studied without addition of any impurity elements by Y.J. Li and L. Arnberg(10), showing a major drop in the number density of dispersoids between 450 ℃

and 500 °C. The same can be observed in the AA3003-Mo-Cd alloy, meaning that the dispersoids will not be thermally stable at higher temperatures with additions of Mo and Cd in the levels tested in this thesis. The hardness is, however, quite stable at these temperatures in the AA3003-Mo-Cd alloy, which is promising for the stability. The dispersoids seem to precipitate out faster with additions of Mo and Cd, as the number density of the dispersoids has its peak at 350 °C, as opposed to 400 °C for the pure AA3003 alloy, as can be seen in Figure 5.4. The equal circle diameter of the dispersoids in the Mo- and Cd-containing alloy is larger than in the pure AA3003 alloy at every temperature, and it generally has a higher number density, which could be a reason for its increased hardness compared to the AA3003 alloy. In Figure 4.40 and Figure 4.41 it is seen that the size distribution of the dispersoids in the AA3003-Mo-Cd alloy gets much wider, and it is confirmed that the dispersoids get much larger with increasing temperatures. As the number density starts to decrease already at 350 °C growth and coarsening of the precipitates seem to be the dominating mechanism after this temperature, but the fact that the size distribution gets wider with increasing temperatures could indicate that new grains are nucleated even at higher temperatures. I could also mean that some precipitates grow slower than others.

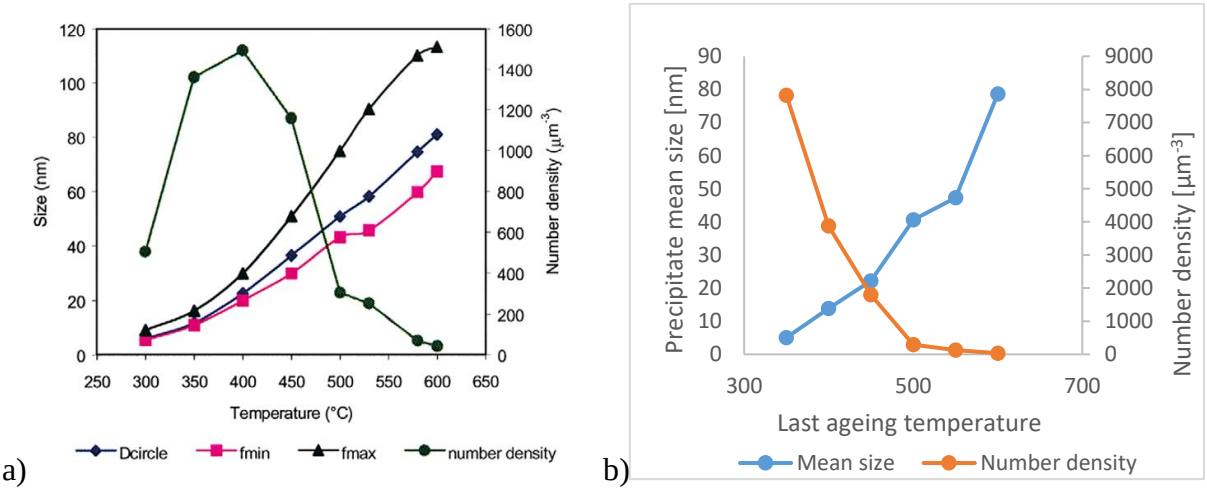

Figure 5.4: a) Fig. 5 from Y.J. Li and L. Arnberg, showing number density, maximum- and minimum ferret diameter, and equal circle diameter of the dispersoids in a pure AA3003 alloy. b) Number density and mean size of the dispersoids in the present AA3003-Mo-Cd alloy repeated from Figure 4.41.

From Figure 4.41 it is apparent that the number density of the Al-Mo-Cd alloy decreases with increasing temperatures, and it is very low already at 500 °C. The maximum strength and hardness of the alloy should be seen at the temperature where the density of dispersoids is the highest, which is not the case for this alloy. This might be because the dispersoids are so small

at 350 ℃-400 ℃ that the hardening contribution is insignificant. It might also be because the dispersoids are not homogeneously dispersed at the low temperatures, with some areas having less than 1600 dispersoids per μm^3 in the 350 ℃ sample. From
Table 4.15 it is also seen that the volume fraction of dispersoids is higher at 450 ℃ than at 350 ℃ and 400 ℃, which helps explain why the alloy is hardest when heated to 450 ℃.

5.2.3 Tensile strength and dispersoid strength contribution

For the AA3003-Mo-Cd alloy, the ultimate tensile strength is about the same in the samples heated to 450 ℃ and 200 ℃. The yield stress, on the other hand, is much higher in the 450 ℃, showing that the strengthening contribution from the dispersoids is larger than from the Cd-particles. The as cast sample is slightly harder than the SHT sample with regard to both yield- and tensile strength.

The strength contribution from the dispersoids can be found by comparing the strength of two samples where the solid solution strengthening is the same, and only the dispersoids differ. From Figure 4.24 it can be seen that the as cast sample and the sample heated to 200 ℃ have the same electrical conductivity, indicating that they have the same levels of elements in solid solution. Therefore, it is reasonable to think that the increase in yield strength is only from the mechanism of dispersoid strengthening. The electrical conductivity of the 450 ℃ sample is 4.2MS/m higher than the as cast sample, which means it contains significantly lower levels of elements in solid solution. The sample heated to 600 ℃ was held there for 24 hours before water quenching, meaning it was homogenized. Y.J. Li et al. have investigated the AA3003 alloy before, and as Mo and Cd have a very little solubility in solid Al, the data from their experiments can be used for this alloy as well (7). According to them, the electrical conductivity of AA3003 heated at 600 ℃ for 24 hours is 21.2MS/m, which is similar to the 450 ℃ sample which has a conductivity of 22.4MS/m. The 600 ℃ sample is therefore thought to have the same levels of elements in solid solution, therefore it is used as a reference sample to determine the contribution from the dispersoids. The increase in yield strength from the respective reference samples to the dispersoid or cadmium particle containing samples can be found in Table 5.2.

From equations (2.2) and (2.6), data from the tensile testing and the image analysis, the strength contribution from the dispersoids or cadmium particles can also be calculated. This has been

done for the 200 ℃ and 450 ℃ sample from the AA3003-Mo-Cd alloy, and the results can be found in Table 5.2. As can be seen, the calculated results are significantly higher than the measures results. This is most likely because areas with a high particle density were preferred when obtaining the images the calculations are based on. This means that the calculated number density, and therefore also the volume fraction, might be unrealistically high. As Equation (2.2) is very sensitive to the volume fraction, this will have a large impact on the calculated strength contribution of the particles or dispersoids. There might also still be some dispersoids left in the homogenized sample, making the increase in yield strength smaller than the actual contribution of the dispersoids. The calculations are based on the assumption that the dislocations do not cut through the particles, that they only bypass them by looping. This is a safe assumption for the dispersoids, but as the Cd precipitates are much smaller, one cannot be sure that no cutting takes place. Therefore, the margin of error in the results for the 200 ℃ sample is large.

Table 5.2: Strength contributions from the Cd-particles and dispersoids in the 200 and 400 samples respectively. The reference samples are the as cast and solid solution heat treated samples respectively.

Temperature	Yield strength in reference sample	Yield strength after heat treatment	Increase in yield strength	Dispersoid/Particle contribution to yield strength
200 ℃	66.8 MPa	77.4 MPa	10.6	29.2
450 ℃	62.6 MPa	96.5 MPa	34.0	56.1

5.3 AA7050(-Cd)

5.3.1 Hardness and electrical conductivity

In Figure 4.48 one can see that the standard deviations on some of the hardness measurements done on the AA7050 alloy without Cd are very high. This might be because the sample was porous, and the pores were not homogeneously dispersed. The sample with Cd was significantly less porous, which made the hardness measurements more stable. There is also a much higher standard deviation on the samples heated in one step than the samples heat treated at two temperatures. This could be due to variations in the samples, as the AA7050 ingot was relatively porous.

In Figure 4.48 it can be seen that in the one-step hardening of the alloys, the alloy without Cd is slightly harder than the one with Cd, even though it was softer after the SHT. In Figure 4.49 it is seen that the Cd containing alloy was, however, harder in the two-step aging treatment. This is to be expected, as it was also harder after the SHT. The alloy without Cd had the highest increase in strength in both heat treatments. Therefore, it is apparent that additions of 0.28wt% of Cd will not make the alloy harder using this heat treatment, it is rather the opposite. In the two-step hardening it is notable that the hardness only increases slightly, by around 10HV, after the initial 6 hours at 120 ℃. This can also be seen in the one-step treatment at 120 ℃, as the hardness does not increase significantly after the initial 6 hours. This can indicate either that 120 ℃ for 6 hours is optimal parameters for age hardening this alloy, or that 165 ℃ is not the right temperature to continue hardening. The higher temperature is used to make the precipitates nucleated at 120 ℃ grow. In Figure 4.49 it is shown that the electrical conductivity increases, which means that either the precipitates grow, or new ones are made.

It seems like the Cd precipitates at a lower temperature than the other elements in the alloy, as the electrical conductivity in the Cd-containing alloy keeps increasing after one hour at 120 ℃, while the conductivity in the alloy without Cd stabilizes, and does not increase until the temperature is increased. This is in line with theory, as Cd has a very high diffusivuty. This stabilization indicates that the maximum volume fraction of precipitates nucleated has been reached at around one hour of heating at 120 ℃ for the AA7050 alloy, as the concentration in solid solution is stable.

The electrical conductivity of the samples increases throughout the heat treatment, and it increases very rapidly when the samples start to lose their strength, as can be seen in Figure 4.49. The alloys start to lose their strength when the precipitates start to coarsen into larger particles. In these alloys, it seems like the rate of precipitation increases in the coarsening process.

Chapter 6: Conclusions

Several alloys have been investigated with regard to hardness, electrical conductivity, strength and microstructure. The conclusions from these investigations are as follows:

6.1 Al-Zr alloys

According to electrical conductivity measurements, additions of Cd to an Al-Zr alloy both enhances the volume fraction of precipitates at the peak hardness, and accelerates the precipitation kinetics. This points to Cd lowering the nucleation energy, and explains that the precipitates in Al-Zr-Cd alloys have a higher hardening effect than the Al_3Zr precipitates at 400 ℃ - 550 ℃. If a faster heat treatment is chosen, additions of Cd are very beneficial to the yield strength. When using the most efficient heat treatment, it does, however, not seem to have any clear strengthening effect at these temperatures

Additions of Cd also allows the Al-Zr alloys to have another peak in hardness at 200 ℃. Using the faster heat treatment, this peak has approximately the same hardness as the higher temperature peak, but it is lower than the 400 ℃ - 550 ℃ peak if the Zr gets more time to diffuse. The precipitates at 200℃ are also shown to be effective at strengthening the alloys. Further investigations with a more advanced TEM or atom probe tomography is needed to know the composition and structure of the precipitates at both peaks.

When comparing to the literature it is obvious that addition of Sc is much more effective at hardening the alloy than Cd, when similar amounts are added. Cd is, therefore, not suitable as a direct substitute for Sc. The effect of Cd in Al-Zr alloys seems promising, and further investigation into different amounts is recommended.

6.2 AA3003 alloys

All alloys reach a hardness peak after heating to 450 ℃, which is due to precipitation of dispersoids. The precipitation of the α-Al(MnFe)Si commences at 300 ℃ - 350 ℃ in the AA3003-Mo-Cd alloy. The dispersoids grow with increasing temperature from 5 nm at 350 ℃ to almost 80 nm at 600 ℃. The dispersoids peak in number density at 350 ℃, but as the dispersoids are very small and inhomogeneously dispersed, the maximum hardening contribution is not reached until 450 ℃.

The addition of Cd to an AA3003 alloy creates an additional hardness peak at 200 ℃ - 250 ℃ due to precipitation of a high number of Cd-containing precipitates. The addition of Cd also significantly increases the peak hardness of the AA3003 alloy achieved by heating to 450 ℃, which is due to the formation of much higher number density dispersoids in the alloy.

Additions of Cr to an AA3003-Mo-Cd alloy most likely decrease the hardening contribution from the dispersoids. Addition of the tested amount of Cr to the AA3003-Mo-Cd alloy is therefore not beneficial.

Additions of Mo to an AA3003-Cd alloy increases the hardness of the alloy substantially, which is assumed to be due to the formation of α-Al(Mn,Fe,Mo)Si dispersoids. As Mo has a much lower diffusion rate than Mn and Fe in Al, the formation of α-Al(Mn,Fe,Mo)Si dispersoids has also reduced the coarsening rate of the dispersoids. As both hardness peaks are further increased with Mo, a synergy effect between the Mo and Cd and is likely.

The ultimate tensile strength in the AA3003-Mo-Cd samples aged at 200 ℃ and 450 ℃ is very similar, but the yield strength of the 450 ℃ sample is notably higher. Both the calculated and real increase in tensile strength due to dispersoids or Cd-containing precipitates is higher in the 450 ℃ than the 200 ℃, meaning that the dispersoids gives a higher strength contribution than the Cd-particles, which is in line with the hardness results.

6.3 AA7050 alloys

With the heat treatments selected in this work, the AA7050 alloy cannot be further strengthened by adding 0.28wt% Cd. As the electrical conductivity increases more in the Cd-containing alloy than in the regular AA7050-alloy a higher volume fraction of the solutes most likely precipitates out, but the hardness of the alloy is not affected by this.

Bibliography

1. Aluminium H. [Online]. Available: http://www.hydro.com/en/About-aluminium/Why-aluminium/Physical-properties/. [Accessed 23 April 2017]. .

2. Askeland DR, Fulay PP. The science and engineering of materials. 5th ed. ed. Toronto, Ont: Thomson; 2006.

3. Callister WD, Rethwisch DG. Materials science and engineering : an introduction. 7th ed. ed. New York: Wiley; 2007.

4. Mørtsell EA, Holmestad R, Marioara C, Røyset J. Precipitation in multicomponent, lean, Al-Mg-Si alloys: A transmission electron microscopy study. NTNU; 2016.

5. Dieter GE, Bacon D. Mechanical metallurgy. SI metric ed. ed. London: McGraw-Hill; 1988.

6. Muggerud AMF, Mørtsell EA, Li Y, Holmestad R. Dispersoid strengthening in AA3xxx alloys with varying Mn and Si content during annealing at low temperatures. Materials Science & Engineering A. 2013.

7. Li YJ, Muggerud AMF, Olsen A, Furu T. Precipitation of partially coherent α-Al(Mn,Fe)Si dispersoids and their strengthening effect in AA 3003 alloy. Acta Materialia. 2012;60(3):1004-14.

8. Altenpohl D. Aluminium und Aluminiumlegierungen. Berlin: Springer-Verlag; 1965.

9. Trømborg E. Phase transformations during homogenization of commercial AlMn-alloys. Trondheim: Universitetet i Trondheim, Norges tekniske høgskole, Metallurgisk institutt; 1994.

10. Li YJ, Arnberg L. Quantitative study on the precipitation behavior of dispersoids in DC-cast AA3003 alloy during heating and homogenization. Acta Materialia. 2003;51(12):3415-28.

11. Zeng Y, Mu S, Wu P, Ong KP, Zhang J. Relative effects of all chemical elements on the electrical conductivity of metal and alloys: An alternative to Norbury–Linde rule. Journal of Alloys and Compounds. 2009;478(1):345-54.

12. Knipling KE, Dunand DC, Seidman DN. Precipitation evolution in Al–Zr and Al–Zr–Ti alloys during isothermal aging at 375–425 °C. Acta Materialia. 2008;56(1):114-27.

13. Knipling KE, Dunand DC, Seidman DN. Precipitation evolution in Al–Zr and Al–Zr–Ti alloys during aging at 450–600 °C. Acta Materialia. 2008;56(6):1182-95.

14. Knipling KE, Karnesky RA, Lee CP, Dunand DC, Seidman DN. Precipitation evolution in Al–0.1Sc, Al–0.1Zr and Al–0.1Sc–0.1Zr (at.%) alloys during isochronal aging. Acta Materialia. 2010;58(15):5184-95.

15. Emmanuel C, Ludovic L, Thierry É, Williams L, Maylise N, Alexis D. Complex precipitation pathways in multicomponent alloys. Nature Materials. 2006;5(6):482.

16. Forbord B, Lefebvre W, Danoix F, Hallem H, Marthinsen K. Three dimensional atom probe investigation on the formation of Al 3(Sc,Zr)-dispersoids in aluminium alloys. Scripta Materialia. 2004;51(4):333-7.

17. Fuller CB, Murray JL, Seidman DN. Temporal evolution of the nanostructure of Al(Sc,Zr) alloys: Part I – Chemical compositions of Al 3(Sc 1− x Zr x) precipitates. Acta Materialia. 2005;53(20):5401-13.

18. Fuller CB, Seidman DN, Dunand DC. Mechanical properties of Al(Sc,Zr) alloys at ambient and elevated temperatures. Acta Materialia. 2003;51(16):4803-14.

19. Solberg JK, Norges teknisk-naturvitenskapelige universitet Institutt for m. Teknologiske metaller og legeringer. Trondheim: Institutt for materialteknologi, Norges teknisk-naturvitenskapelige universitet; 2008.

20. Precipitation of Dispersoids in DC-Cast AA 31 O 3 Alloy during Heat Treatment. Hoboken, NJ, USA: Hoboken, NJ, USA: John Wiley & Sons, Inc.; 2013. 1021-7 p.

21. Liu K, Chen XG. Development of Al–Mn–Mg 3004 alloy for applications at elevated temperature via dispersoid strengthening. Materials & Design. 2015;84:340-50.

22. Liu K, Ma H, Chen XG. Enhanced elevated-temperature properties via Mo addition in Al-Mn-Mg 3004 alloy. Journal of Alloys and Compounds. 2017;694:354-65.

23. Solberg JK, Hansen V. Innføring i transmisjon elektronmikroskopi. S.l.: s.n.; 2007.

24. Nuyten JBM. Quenched structures and precipitation in Al-Cu alloys with and without traceadditions of Cd. Acta Metallurgica. 1967;15(11):1765-70.

25. Sankaran R, Laird C. Effect of trace additions Cd, In and Sn on the interfacial structure and kinetics of growth of θ′ plates in Al・Cu alloy. Materials Science and Engineering. 1974;14(3):271-9.

26. Noble B. Theta-prime precipitation in aluminium-copper-cadmium alloys. Acta Metallurgica. 1968;16(3):393-401.

27. Kanno M, Suzuki H, Kanoh O. The precipitation of theta-prime phase in an Al-4% Cu-0. 06% In alloy. Japan Institute of Metals, Journal. 1980;44:1139-45.

28. Ringer S, Hono K, Sakurai T. The effect of trace additions of sn on precipitation in Al-Cu alloys: An atom probe field ion microscopy study. Metallurgical and Materials Transactions A. 1995;26(9):2207-17.

29. Hardy HK. J Inst Metals. 1951-52:80, 483.

30. Silcock J. Intermediate Precipitates in Aged Binary Alloys of Aluminium with Cadmium, Indium, or Tin. J Inst Metal. 1955;84:19-22.

31. Silcock J, Heal T, Hardy H. The structural ageing characteristics of ternary aluminium-copper alloys with cadmium, indium, or tin. Journal of the Institute of Metals. 1955;84(1):23-&.

32. Hjelen J. Scanning elektron-mikroskopi. 1986.

33. University P. [Online] Available: https://physik.uni-paderborn.de/en/lindner/research/temstem/ [Accessed 10 February 2017]. .

34. Egerton RF, SpringerLink. Electron Energy-Loss Spectroscopy in the Electron Microscope: Springer US; 2011.

35. Fultz B, Howe J, SpringerLink. Transmission Electron Microscopy and Diffractometry of Materials. 4th ed. ed: Springer Berlin Heidelberg : Imprint: Springer; 2013.

36. Iakoubovskii K, Mitsuishi K, Nakayama Y, Furuya K. Thickness measurements with electron energy loss spectroscopy. Microscopy Research and Technique. 2008;71(8):626-31.

37. Hibbeler RC, Fan SC. Mechanics of materials. SI 2nd ed. ed. Singapore: Pearson Prentice Hall; 2005.

38. Archives E. [Online] Available: http://www.engineeringarchives.com/les_mom_tensiletest.html. [Accessed 14 Mars 2017].

39. Knipling KE, Seidman DN, Dunand DC. Ambient- and high-temperature mechanical properties of isochronally aged Al–0.06Sc, Al–0.06Zr and Al–0.06Sc–0.06Zr (at.%) alloys. Acta Materialia. 2011;59(3):943-54.

40. Li H, Bin J, Liu J, Gao Z, Lu X. Precipitation evolution and coarsening resistance at 400°C of Al microalloyed with Zr and Er. Scripta Materialia. 2012;67(1):73-6.

41. Gao Z, Li H, Lai Y, Ou Y, Li D. Effects of minor Zr and Er on microstructure and mechanical properties of pure aluminum. Materials Science & Engineering A. 2013;580:92.

Appendix A: XRF Results

XRF results of all the as cast alloys.

Table 0.1: XRF measurements of the as-cast alloys. AA3003 is here used to refer to the AA3003-Mo-Cd alloy. AA3003+Cr is AA-Mo-Cd-Cr.

	Si	Mn	Mg	Zn	Fe	Ti	Cr	Zr	Cd	Cu	Mo
Al-Zr 1	<0.006	0.006	<0.21	0.025	0.072	<0.004	0.006	0.16	-	-	-
Al-Zr 1	0.042	-	<0.09	0.020	0.070	<0.004	0.011	0.16	-	-	-
Average	**0.024**	**0.006**	**<0.15**	**0.023**	**0.071**	**<0.004**	**0.009**	**0.16**	**-**	**-**	**-**
Al-Zr 2	<0.005	-	<0.086	0.017	0.069	0.021	0.006	0.17	-	-	-
Al-Zr 2	<0.006	0.012	0.13	0.024	0.067	<0.004	<0.003	0.18	-	-	-
Average	**<0.006**	**0.012**	**0.108**	**0.021**	**0.068**	**0.013**	**0.005**	**0.18**	**-**	**-**	**-**
Al-Zr 3	<0.002	<0.001	<<0.12	0.03	0.084	0.018	<0.003	0.23	-	-	-
Al-Zr 3	<0.003	<0.002	<<0.12	0.011	0.067	0.015	0.012	0.23	-	-	-
Average	**0.003**	**<0.002**	**<<0.12**	**0.021**	**0.076**	**0.017**	**0.08**	**0.23**	**-**	**-**	**-**
Al-Zr-Cd 1	0.020	0.007	<<0.14	0.19	0.11	0.021	0.003	0.24	0.23	-	-
Al-Zr-Cd 1	0.038	0.007		0.02	0.11		0.011	0.28	0.23	-	-
Average	**0.029**	**0.007**	**<<0.14**	**0.11**	**0.11**	**0.021**	**0.007**	**0.26**	**0.23**	**-**	**-**
Al-Zr-Cd 2	<0.12	0.005	<<0.15	0.025	0.082	<0.004	0.007	0.14	0.28	-	-
Al-Zr-Cd 2	<0.10	0.004	<<0.16	0.021	0.077	<0.004	0.008	0.10	0.30	-	-
Average	**0.011**	**0.005**	**<<0.155**	**0.023**	**0.080**	**<0.004**	**0.008**	**0.12**	**0.29**	**-**	**-**
AA3003	1.07	1.02	<0.099	0.016	0.56	0.023	0.007	0.013	0.17	0.065	0.14
AA3003	1.34	1.04	<0.098	0.018	0.53	0.027	<0.001	0.015	0.17	0.062	0.19
AA3003	>1.23	1.01	<0.099	0.017	0.55	0.022	0.013	0.014	0.16	0.064	0.13
Average	**1.21**	**1.02**	**<0.099**	**0.017**	**0.55**	**0.024**	**0.007**	**0.014**	**0.17**	**0.064**	**0.15**
AA3003+Cr	0.35	0.99	0.11	0.017	0.55	<0.005	0.17	0.015	0.16	0.057	0.14
AA3003+Cr	2.82	1.06	<0.096	0.017	0.58	<0.005	0.21	0.017	0.15	0.062	0.18
AA3003+Cr	>1.42	1.08	<0.099	0.018	0.55	0.024	>0.23	0.014	0.15	0.062	0.22
Average	**1.53**	**1.04**	**<0.098**	**0.017**	**0.56**	**0.011**	**0.20**	**0.015**	**0.15**	**0.60**	**0.19**
AA7050	0.28	0.29	2.03	5.10	0.27	-	0.21	0.02	-	1.25	-
AA7050	0.21	0.30	1.89	4.97	0.27	-	0.21	0.02	-	1.14	-
AA7050	0.28	0.28	2.38	5.11	0.26	-	0.21	0.02	-	1.28	-
Average	**0.26**	**0.29**	**2.10**	**5.06**	**0.27**	**-**	**0.21**	**0.02**	**-**	**1.22**	**-**
AA7050+Cd	0.13	0.27	2.08	5.11	0.34	0.10	0.16	0.02	0.29	1.36	-
AA7050+Cd	0.15	0.27	1.96	5.04	0.34	0.12	0.16	0.018	0.26	1.31	-
Average	**0.14**	**0.27**	**2.02**	**5.08**	**0.34**	**0.11**	**0.16**	**0.019**	**0.28**	**1.34**	**-**

Appendix B: Full EDS results

B.1 Al-Zr(-Cd) alloys

Al-0.16Zr as cast:

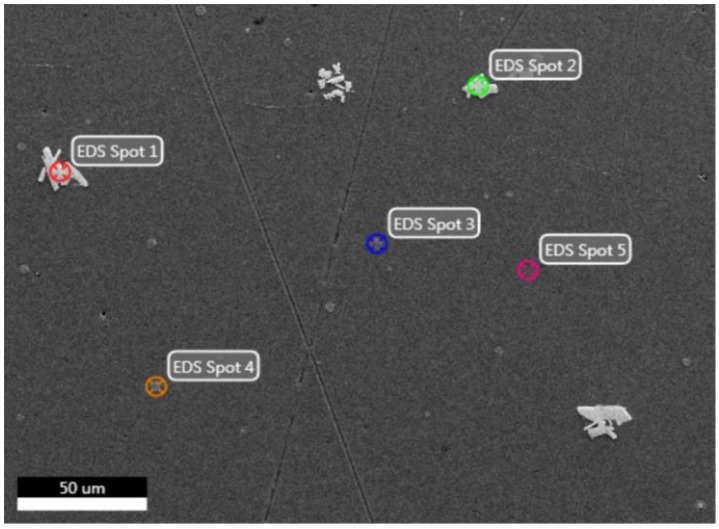

EDS spot 1:

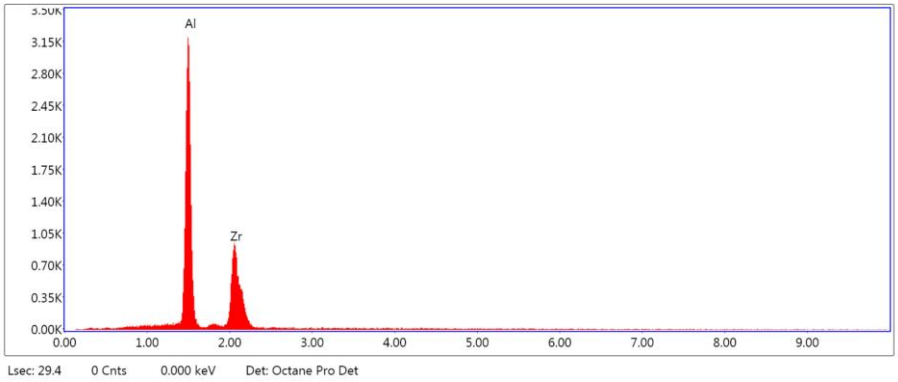

Element	Weight %	Atomic %	Error %
Al	52.55	78.92	3.72
Zr	47.45	21.08	4.75

EDS spot 2:

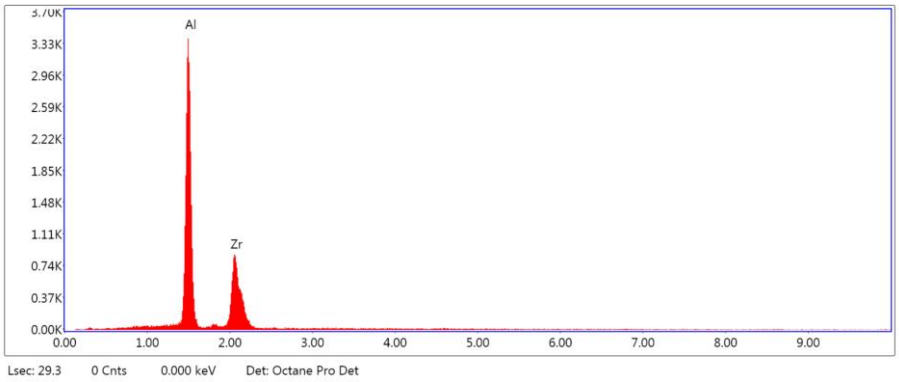

Element	Weight %	Atomic %	Error %
Al	55.16	80.62	3.61
Zr	44.84	19.38	5.06

EDS spot 3:

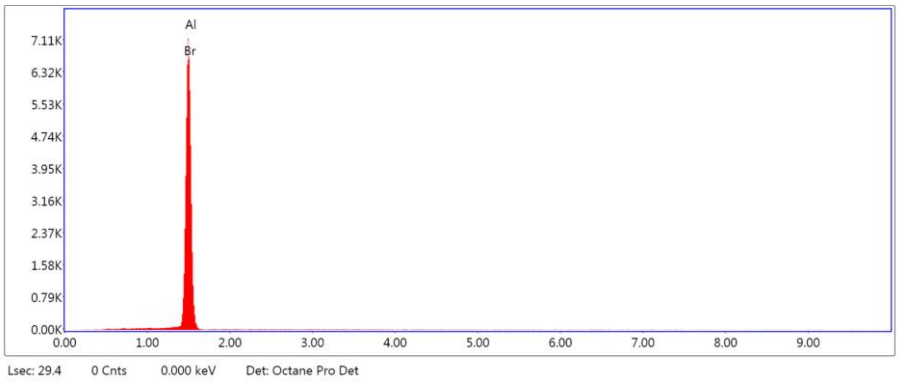

Element	Weight %	Atomic %	Error %
Al	100	100	2.75

EDS spot 4:

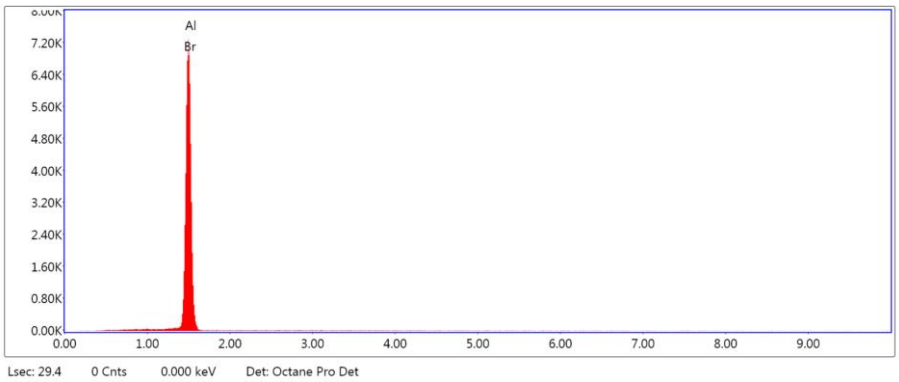

Element	Weight %	Atomic %	Error %
Al	100	100	2.75

EDS spot 5:

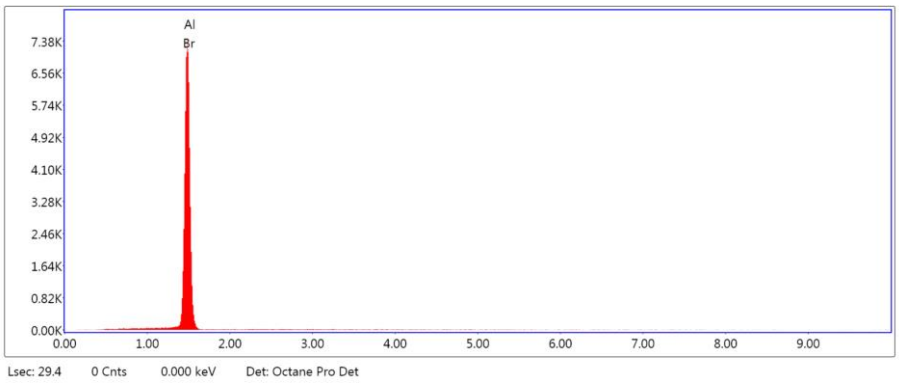

Element	Weight %	Atomic %	Error %
Al	100	100	2.76

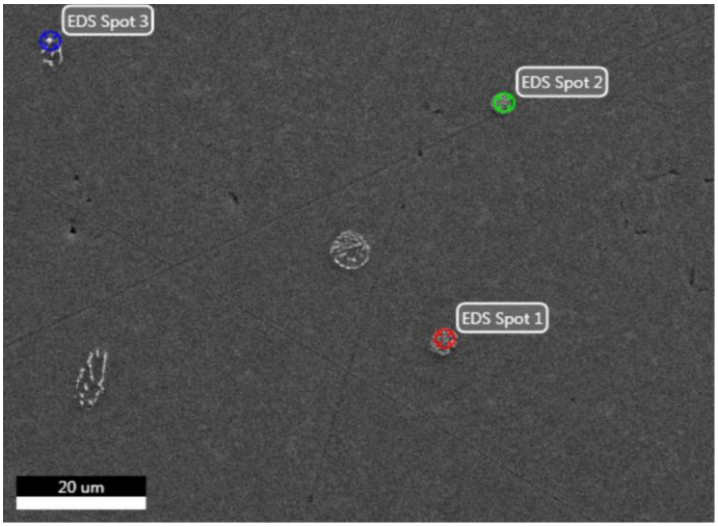

EDS spot 1:

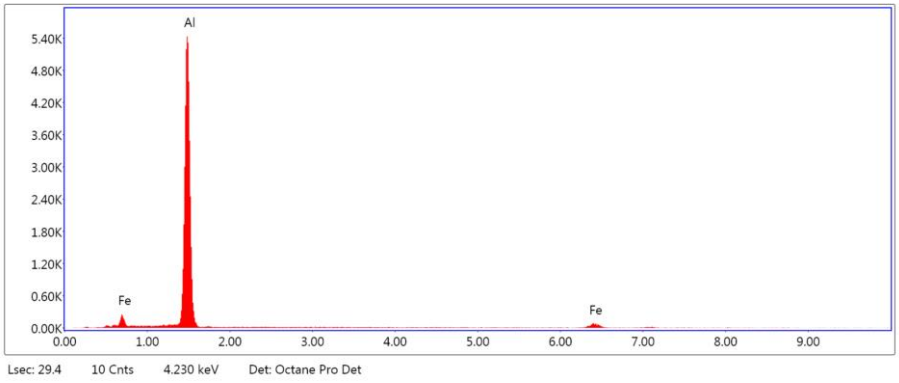

Element	Weight %	Atomic %	Error %
Al	86.21	92.82	3.08
Fe	13.79	7.18	8.14

EDS spot 2:

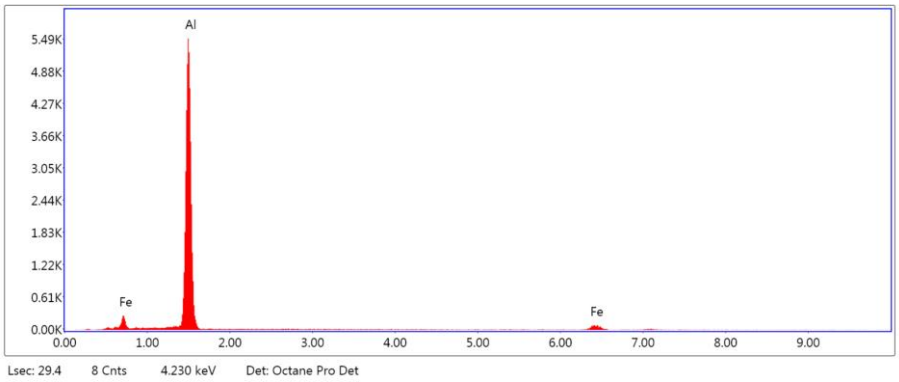

Element	Weight %	Atomic %	Error %
Al	85.04	92.17	3.18
Fe	14.96	7.83	8.36

EDS spot 3:

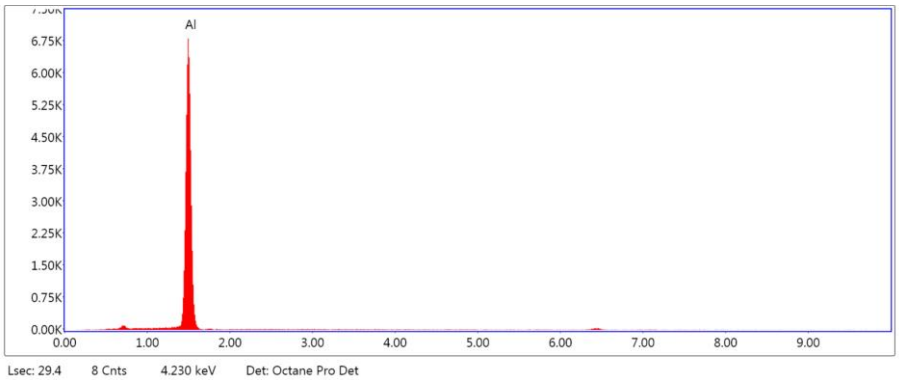

Element	Weight %	Atomic %	Error %
Al	100	100	2.76

Al-0.18Zr as cast:

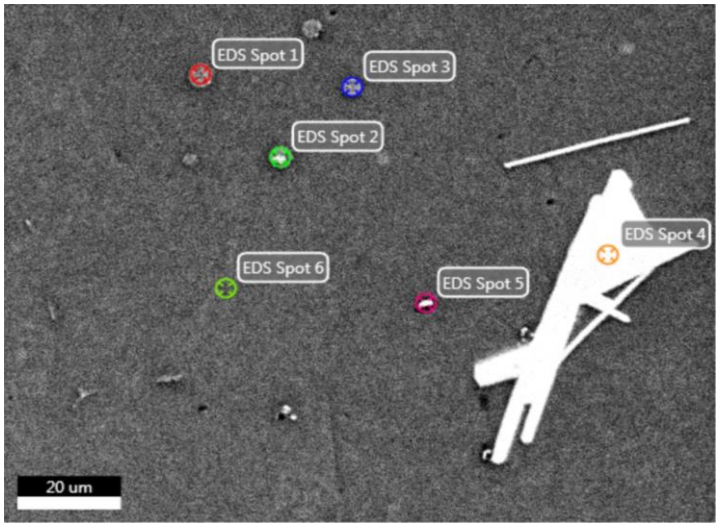

EDS spot 1:

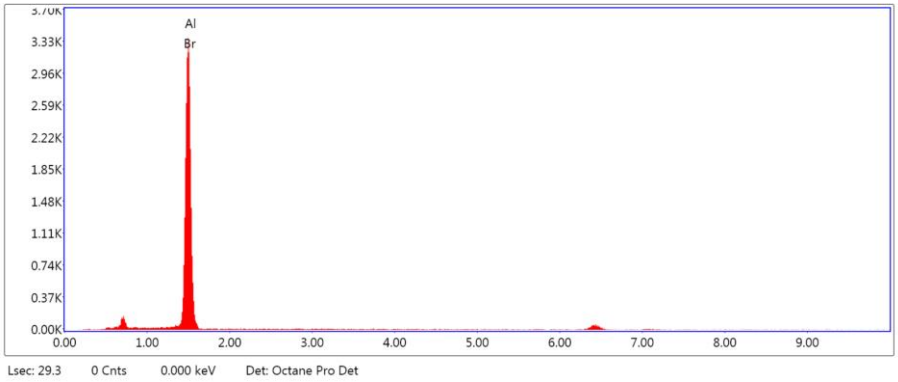

Element	Weight %	Atomic %	Error %
Br	35.41	15.62	4.69
Al	64.59	84.38	3.00

EDS spot 2:

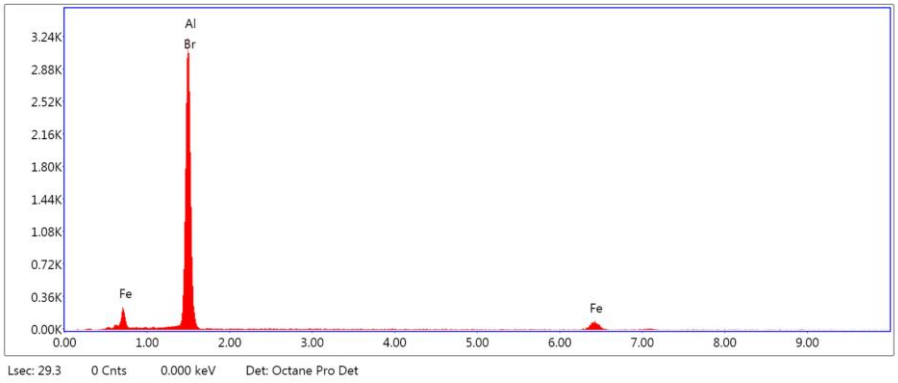

Element	Weight %	Atomic %	Error %
Br	29.08	13.92	3.79
Al	51.20	72.58	4.45
Fe	19.72	13.50	8.31

EDS spot 3:

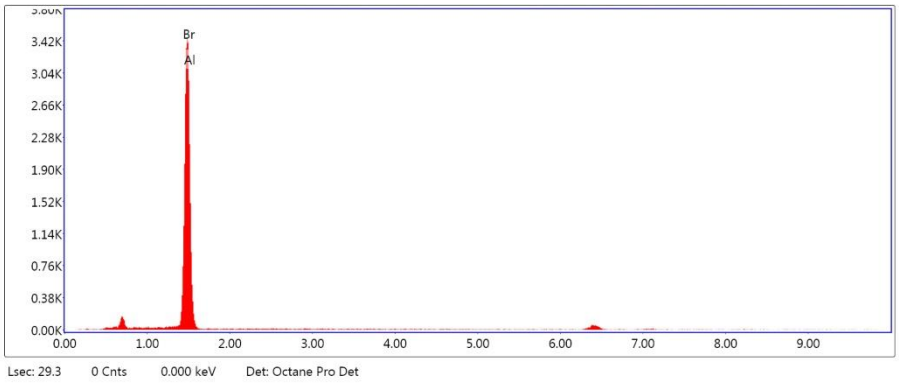

Element	Weight %	Atomic %	Error %
Br	30.47	12.89	5.15
Al	69.53	87.11	2.85

EDS spot 4:

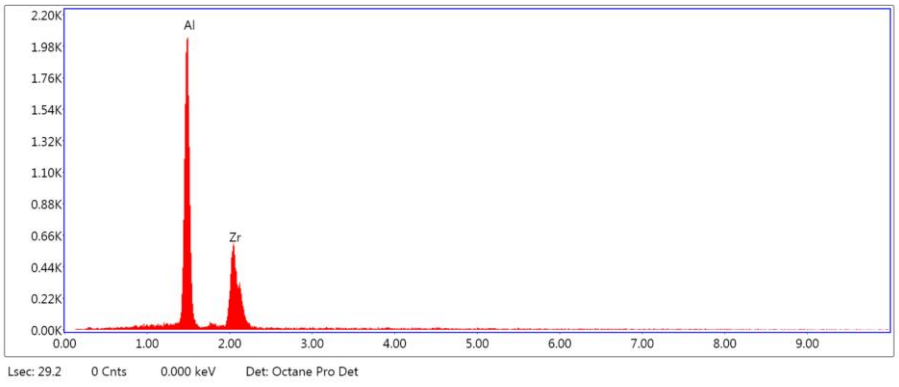

Element	Weight %	Atomic %	Error %
Al	53.25	79.38	3.88
Zr	46.75	20.62	5.17

EDS spot 5:

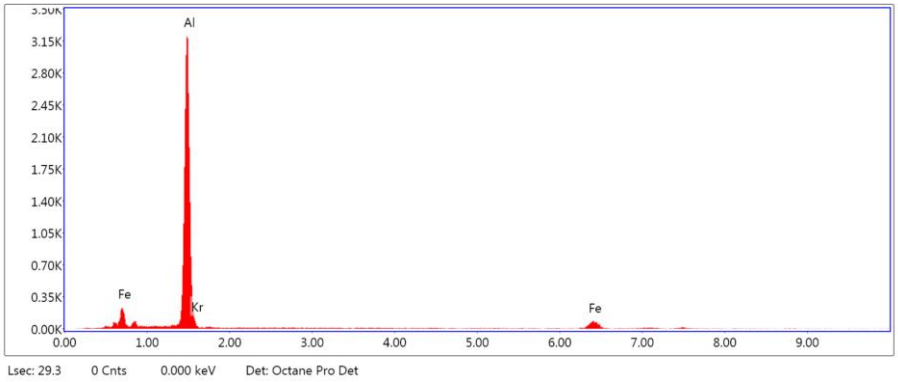

Element	Weight %	Atomic %	Error %
Al	76.48	87.52	3.81
Kr	2.83	1.04	17.03
Fe	20.69	11.44	8.09

EDS spot 6:

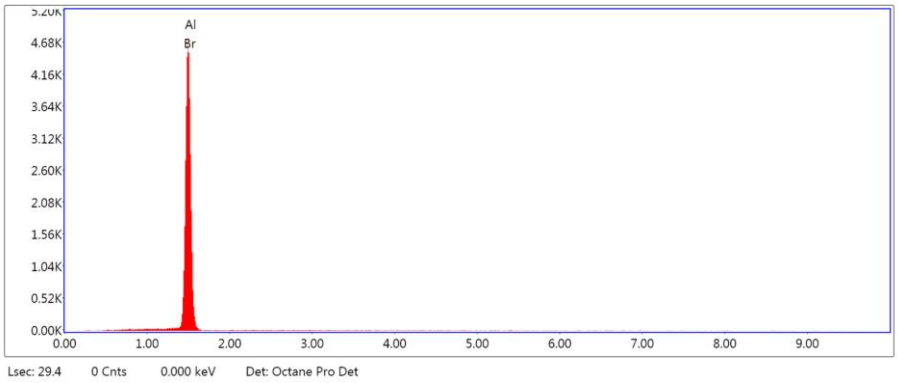

Element	Weight %	Atomic %	Error %
Al	100	100	2.79

Al-0.23Zr as cast:

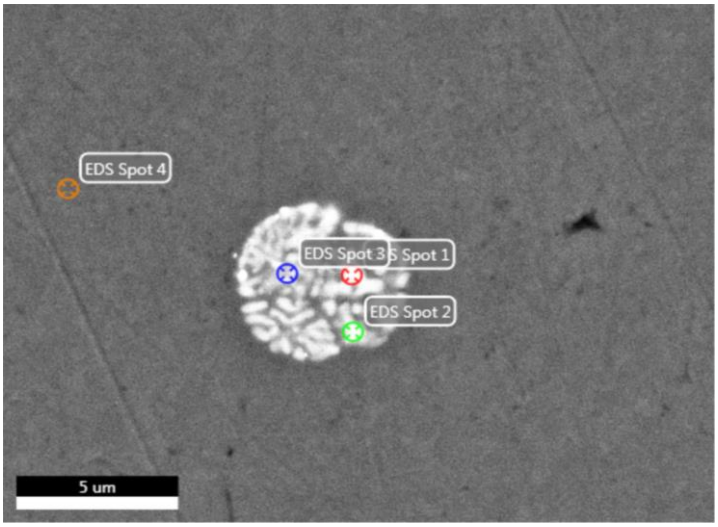

EDS spot 1:

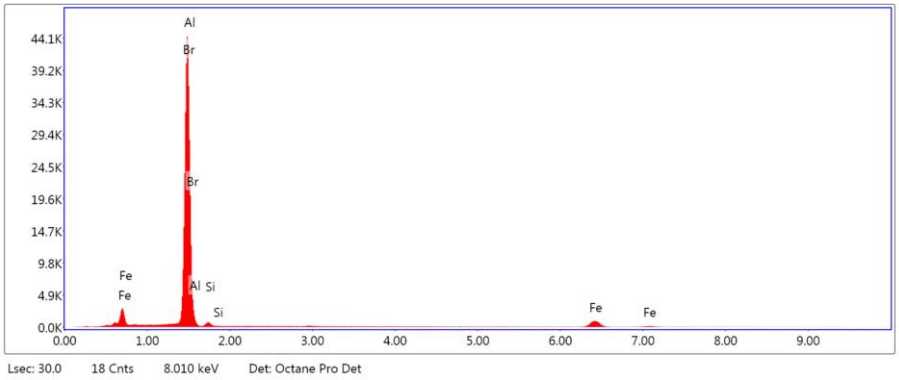

Element	Weight %	Atomic %	Error %
Br	31.69	15.22	1.92
Al	49.81	70.84	3.34
Si	1.80	2.46	8.77
Fe	16.70	11.48	3.99

EDS spot 2:

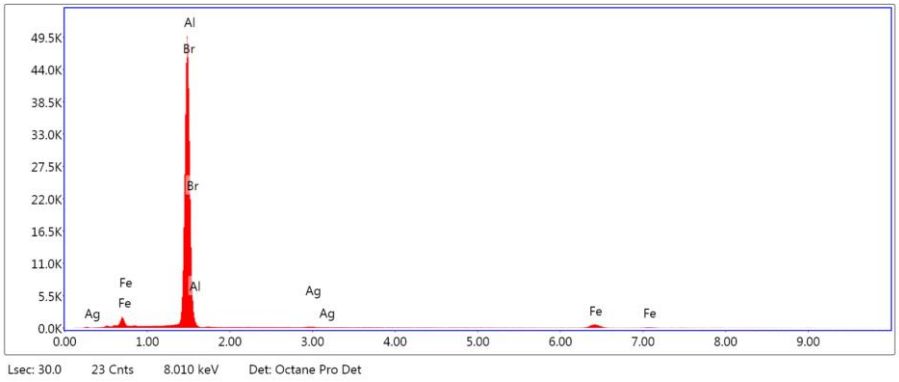

Element	Weight %	Atomic %	Error %
Br	33.10	15.53	1.94
Al	55.50	77.09	2.98
Ag	0.84	0.29	24.53
Fe	10.56	7.09	4.78

EDS spot 3:

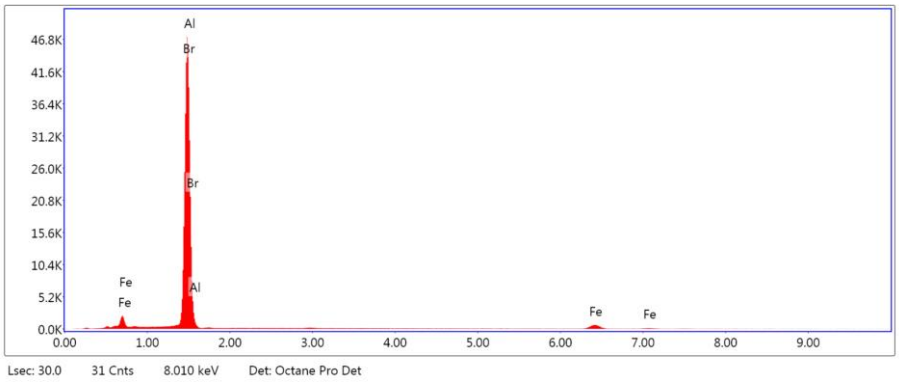

Element	Weight %	Atomic %	Error %
Br	34.57	16.45	1.86
Al	53.58	75.49	3.05
Fe	11.85	8.06	4.50

EDS spot 4:

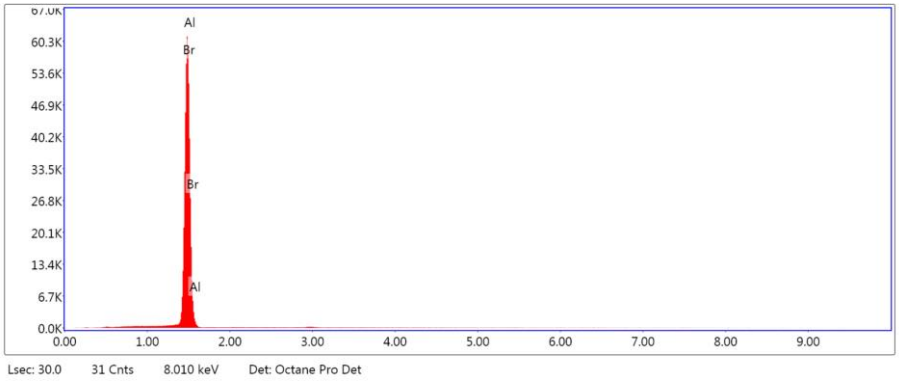

Element	Weight %	Atomic %	Error %
Al	100	100	2.23

Al-0.26Zr-0.23Cd as cast:

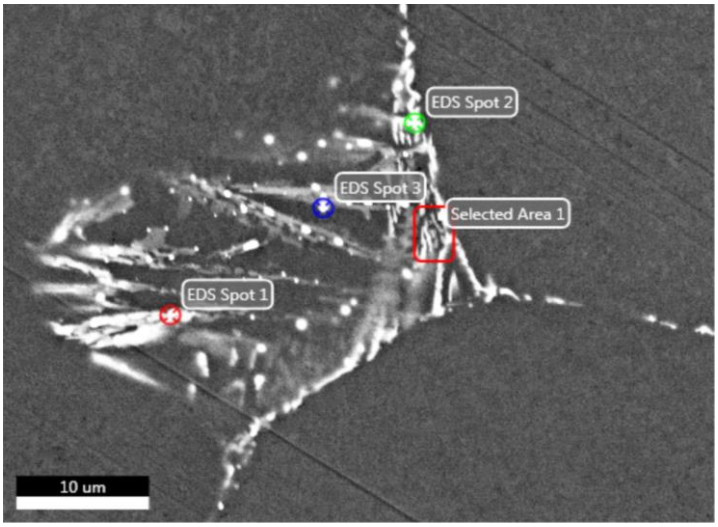

EDS spot 1:

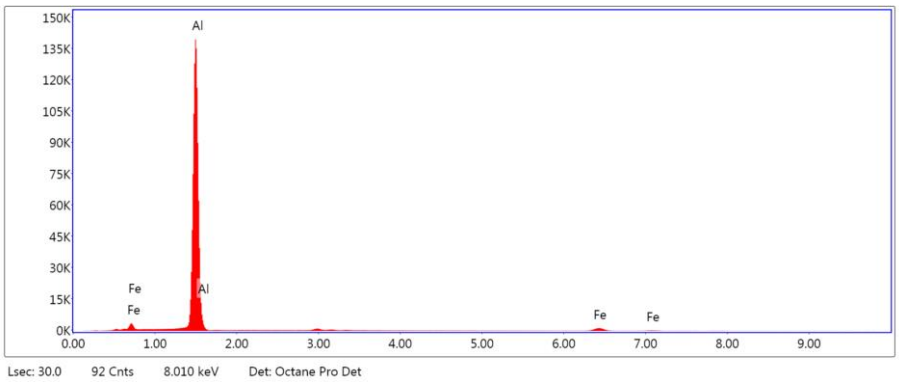

Element	Weight %	Atomic %	Net Int.	Error %
Al	89.87	94.84	33913.77	2.25
Fe	10.13	5.16	591.09	3.98

EDS spot 2:

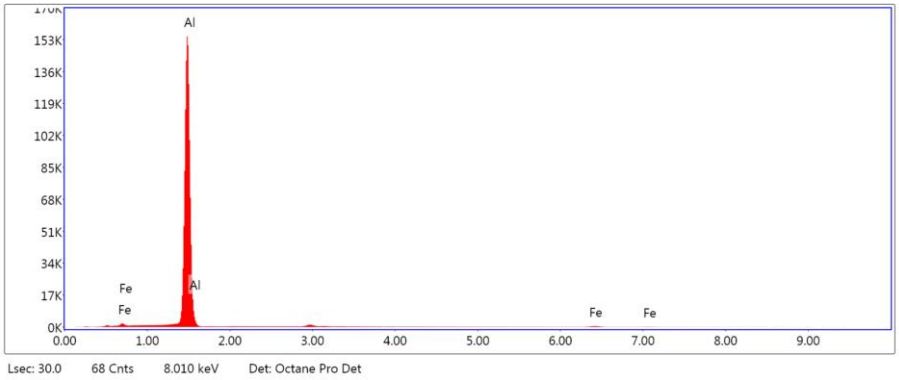

Element	Weight %	Atomic %	Net Int.	Error %
Al	97.01	98.53	37595.29	1.66
Fe	2.99	1.47	171.14	6.94

EDS spot 3:

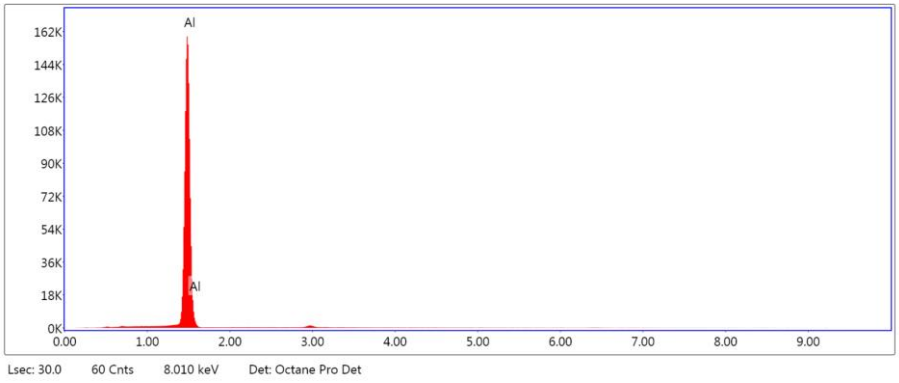

Element	Weight %	Atomic %	Error %
Al	100	100	1.35

Selected area 1:

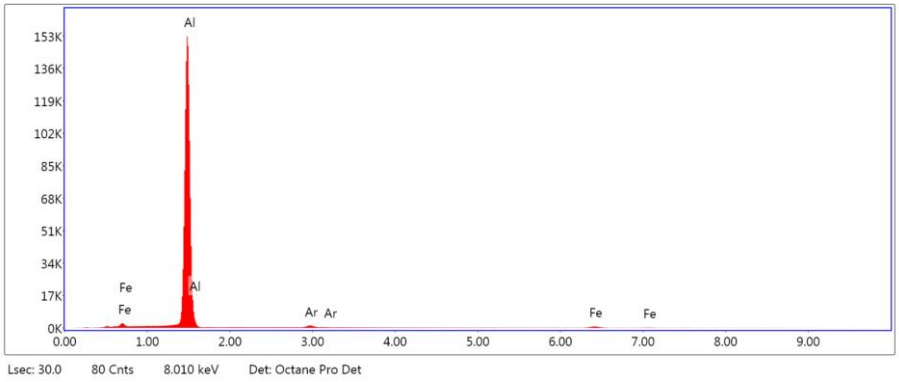

Element	Weight %	Atomic %	Error %
Al	93.22	96.27	1.87
Ar	1.79	1.25	5.57
Fe	4.99	2.49	5.19

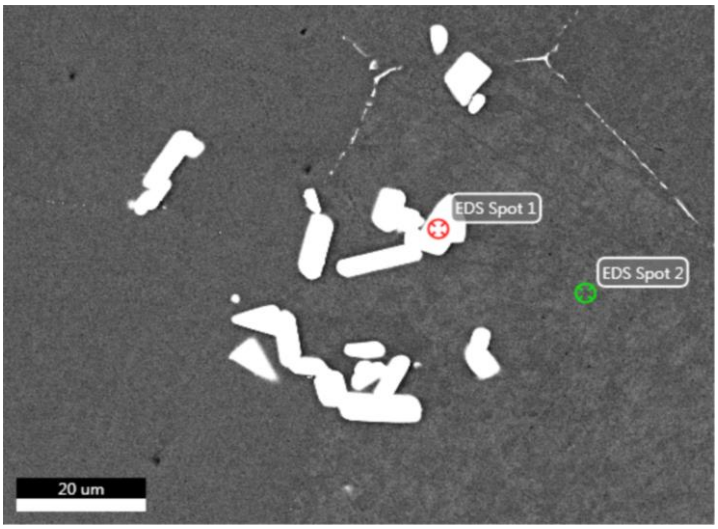

EDS spot 1:

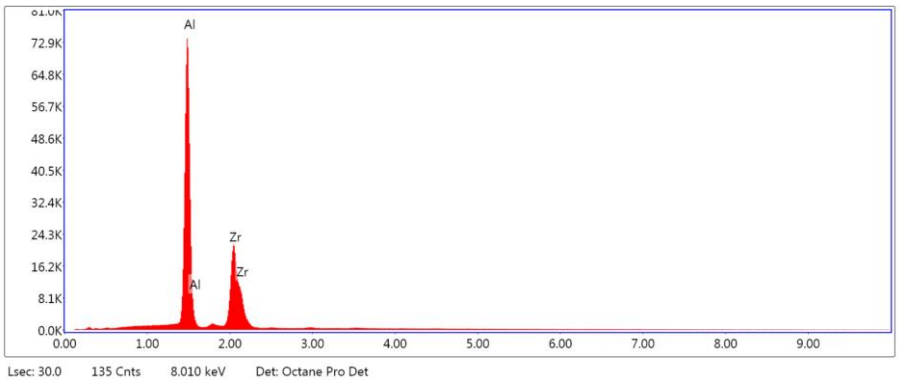

Element	Weight %	Atomic %	Error %
Al	53.11	79.30	2.96
Zr	46.89	20.70	3.32

EDS spot 2:

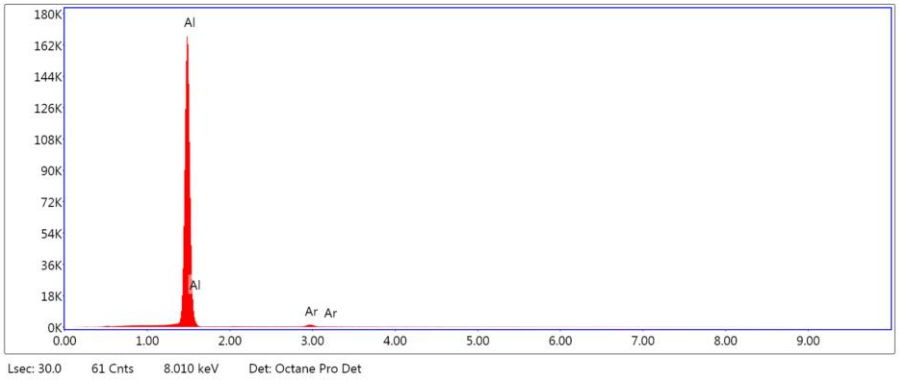

Element	Weight %	Atomic %	Error %
Al	97.94	98.60	1.43
Ar	2.06	1.40	6.04

Al-0.12Zr-0.29Cd as cast:

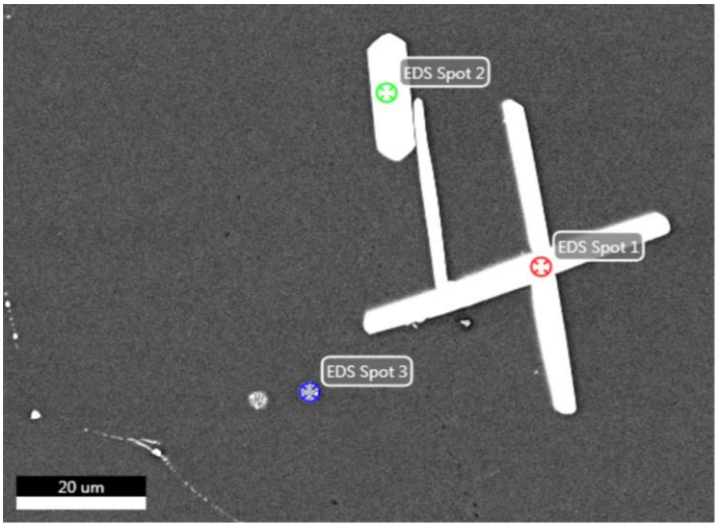

EDS spot 1:

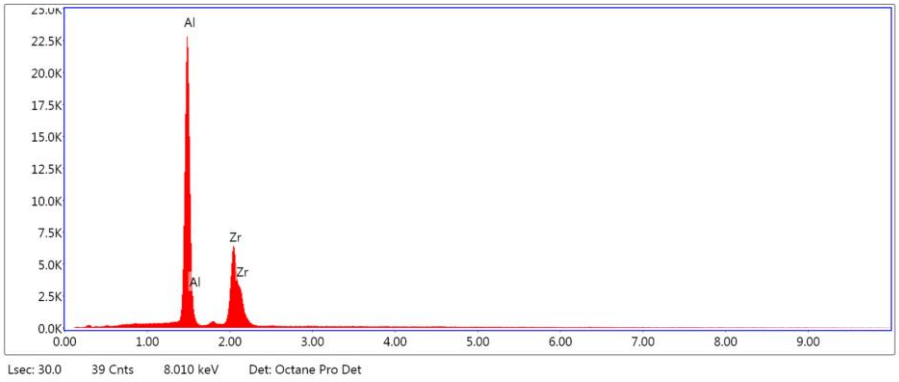

Element	Weight %	Atomic %	Error %
AlK	54.26	80.04	2.98
ZrL	45.74	19.96	3.62

EDS spot 2:

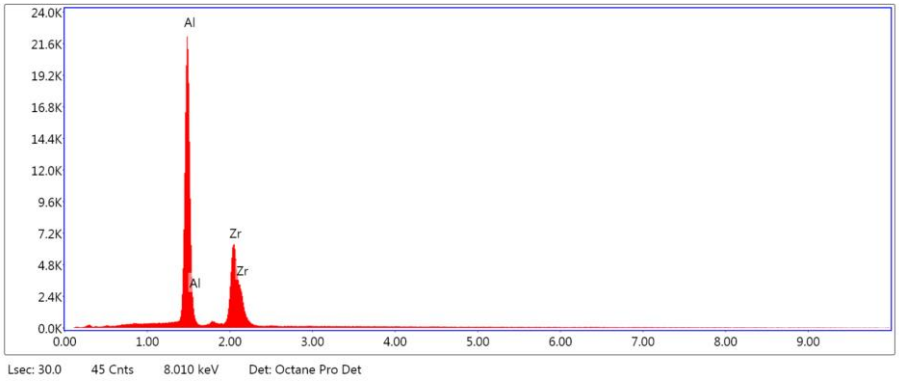

Element	Weight %	Atomic %	Net Int.	Error %
AlK	52.92	79.17	5260.46	3.02
ZrL	47.08	20.83	1592.83	3.57

EDS spot 3:

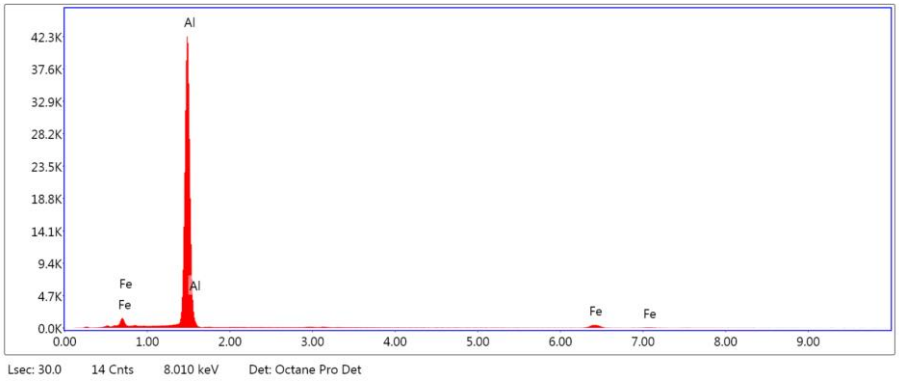

Element	Weight %	Atomic %	Error %
Al	89.15	94.45	2.35
Fe	10.85	5.55	5.20

B.2 AA3003-Mo-Cd

As cast:

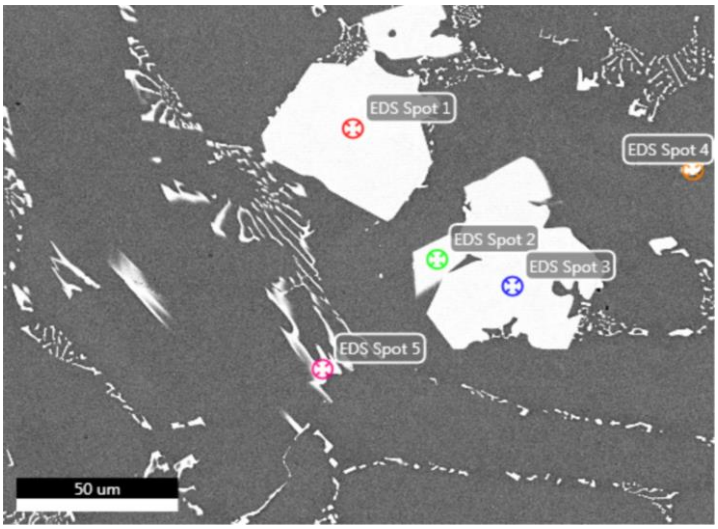

EDS spot 1:

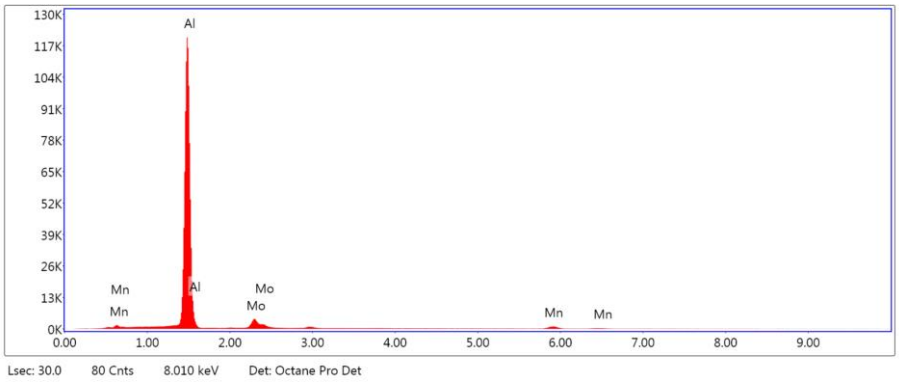

Element	Weight %	Atomic %	Error %
Al	84.30	93.70	2.25
Mo	9.72	3.04	4.52
Mn	5.98	3.26	4.38

EDS spot 2:

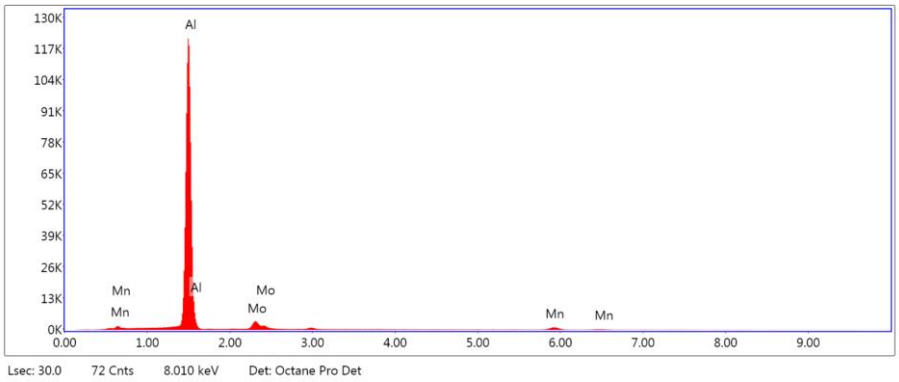

Element	Weight %	Atomic %	Error %
Al	84.57	93.63	2.26
Mo	8.69	2.71	4.14
Mn	6.74	3.67	4.07

EDS spot 3:

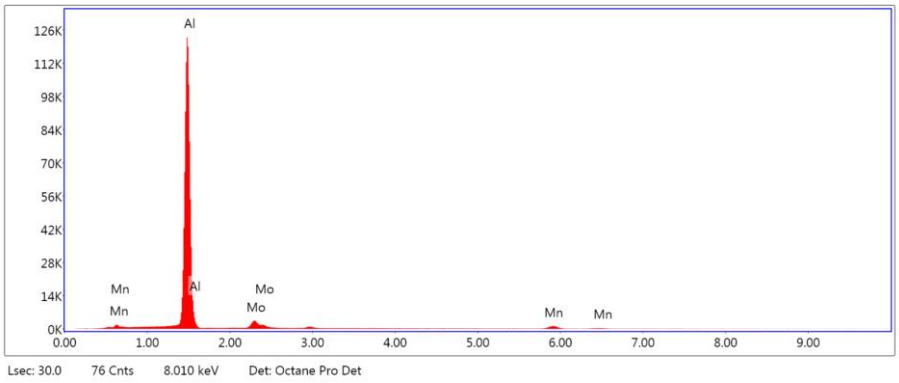

Element	Weight %	Atomic %	Error %
Al	84.68	93.58	2.27
Mo	8.17	2.54	4.66
Mn	7.15	3.88	4.05

EDS spot 4:

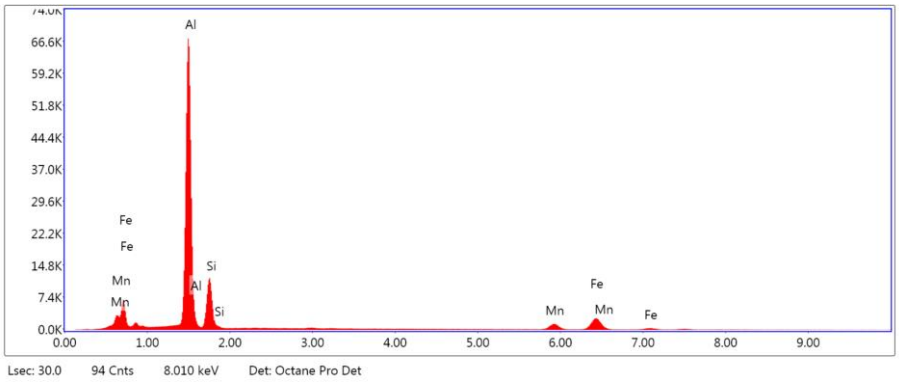

Element	Weight %	Atomic %	Error %
Al	55.93	66.60	3.65
Si	13.99	16.01	5.92
Mn	8.74	5.11	3.84
Fe	21.35	12.28	3.23

EDS spot 5:

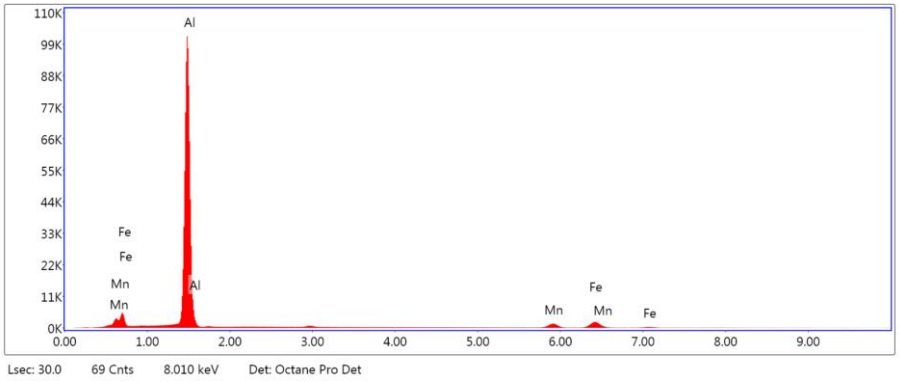

Element	Weight %	Atomic %	Error %
Al	76.21	86.82	3.18
Mn	8.93	5.00	3.77
Fe	14.86	8.18	3.53

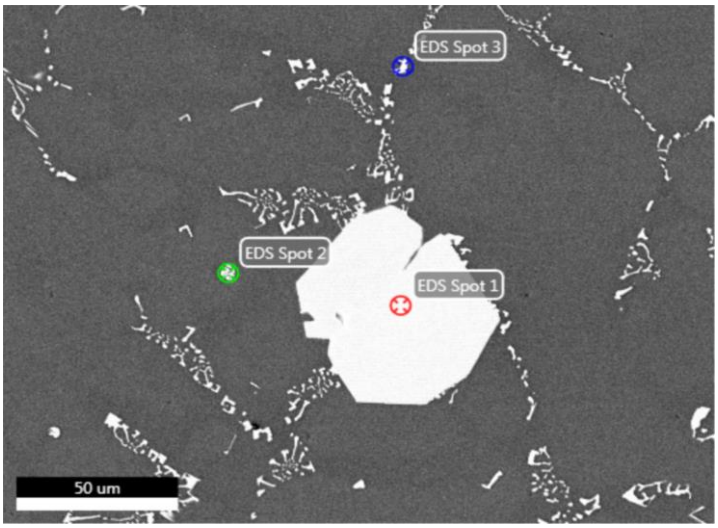

EDS spot 1:

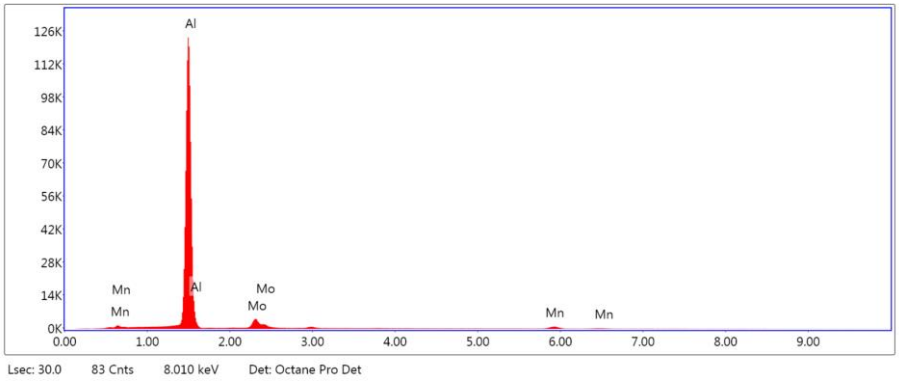

Element	Weight %	Atomic %	Error %
Al	84.24	93.73	2.25
Mo	10.01	3.13	4.11
Mn	5.75	3.14	4.39

EDS spot 2:

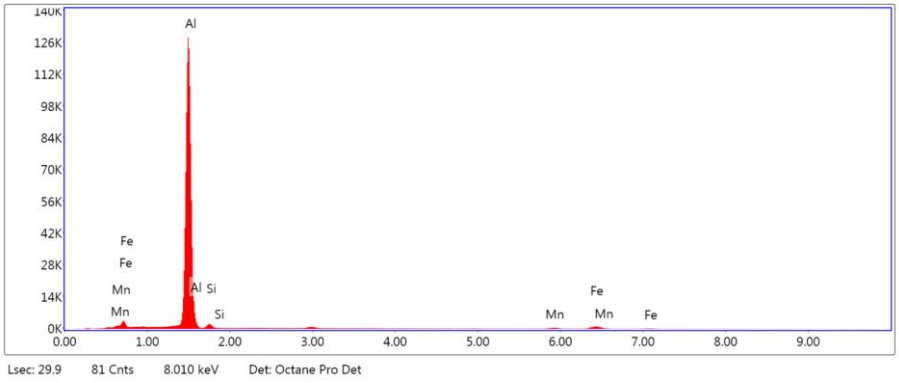

Element	Weight %	Atomic %	Error %
Al	87.33	92.29	2.25
Si	2.42	2.46	7.63
Mn	2.36	1.22	7.12
Fe	7.89	4.03	4.37

EDS spot 3:

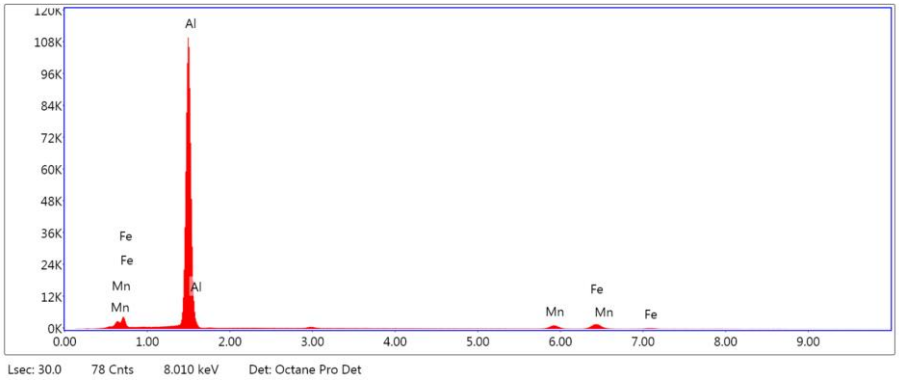

Element	Weight %	Atomic %	Error %
Al	79.19	88.67	2.98
Mn	7.99	4.39	3.81
Fe	12.82	6.93	3.59

Heated to 450 °C:

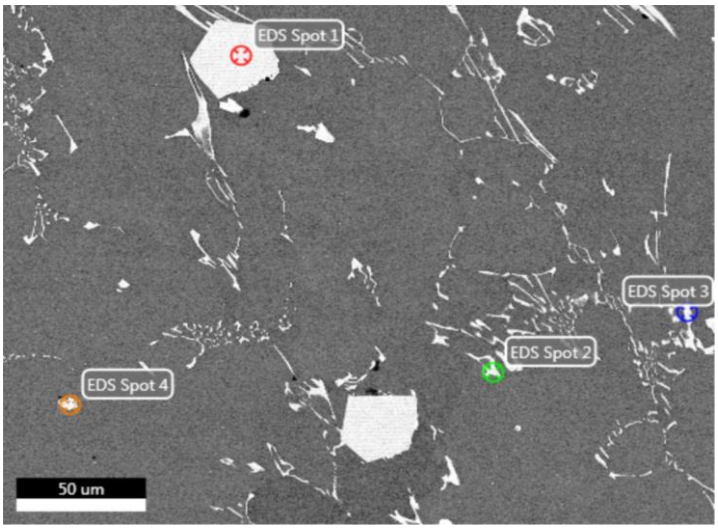

EDS spot 1:

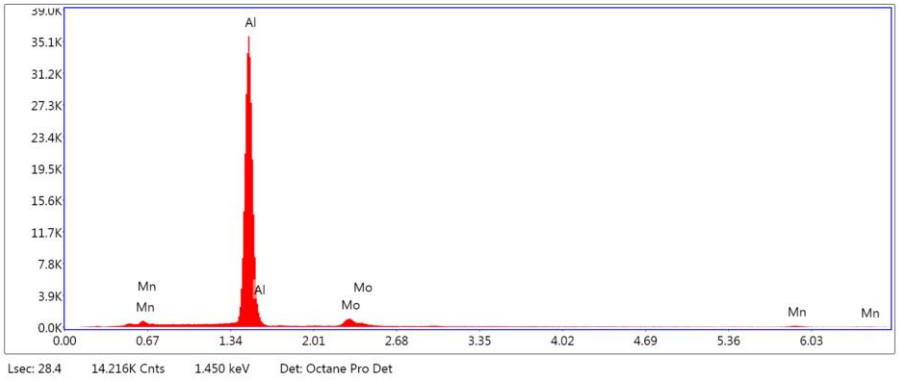

Element	Weight %	Atomic %	Error %
Al	83.33	92.94	2.81
Mo	8.85	2.78	7.11
Mn	7.82	4.28	11.53

EDS spot 2:

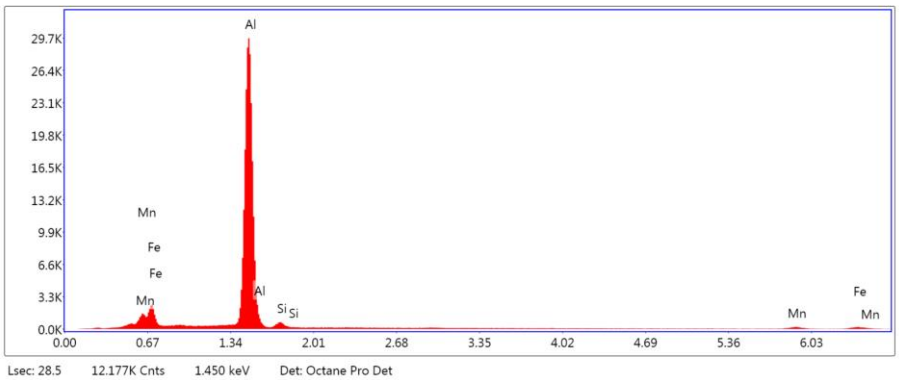

Element	Weight %	Atomic %	Error %
Fe	9.13	4.92	4.38
Al	77.77	86.80	3.18
Si	2.10	2.25	9.77
Mn	11.00	6.03	11.14

EDS spot 3:

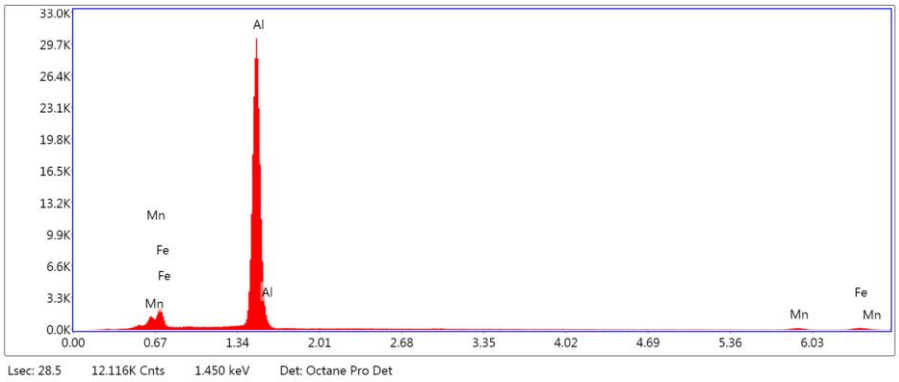

Element	Weight %	Atomic %	Error %
Fe	8.59	4.61	4.76
Al	80.79	89.61	3.14
Mn	10.62	5.78	11.43

EDS spot 4:

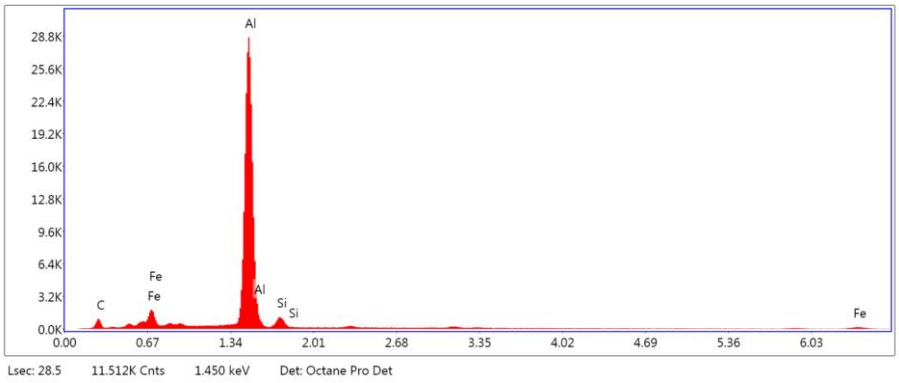

Element	Weight %	Atomic %	Error %
C	15.49	30.08	12.03
Fe	6.76	2.82	3.62
Al	74.16	64.11	2.69
Si	3.59	2.98	7.19

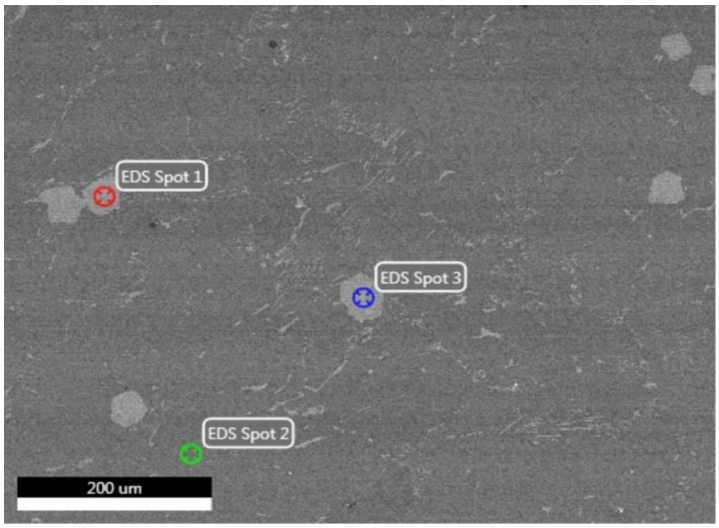

EDS Spot 1:

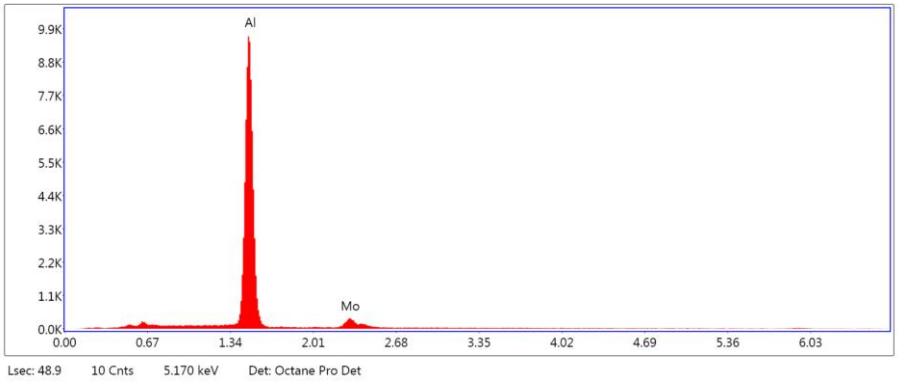

Element	Weight %	Atomic %	Error %
Al	88.90	96.61	2.72
Mo	11.10	3.39	9.49

EDS spot 2:

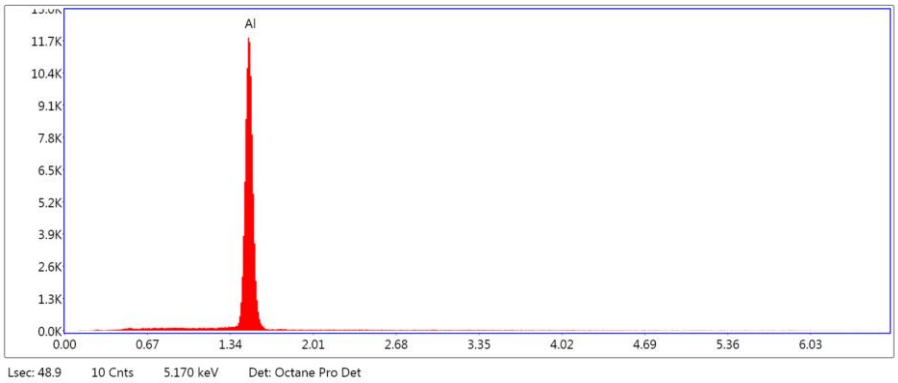

Element	Weight %	Atomic %	Error %
Al	100.00	100.00	2.36

EDS spot 3:

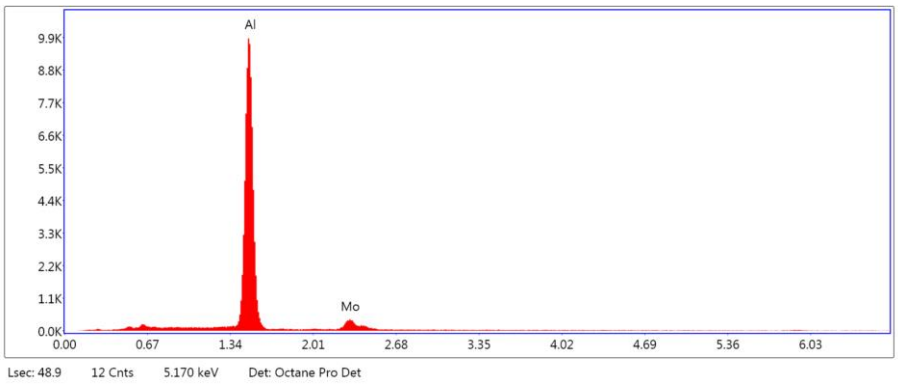

Element	Weight %	Atomic %	Error %
Al	87.65	96.19	2.73
Mo	12.35	3.81	9.31

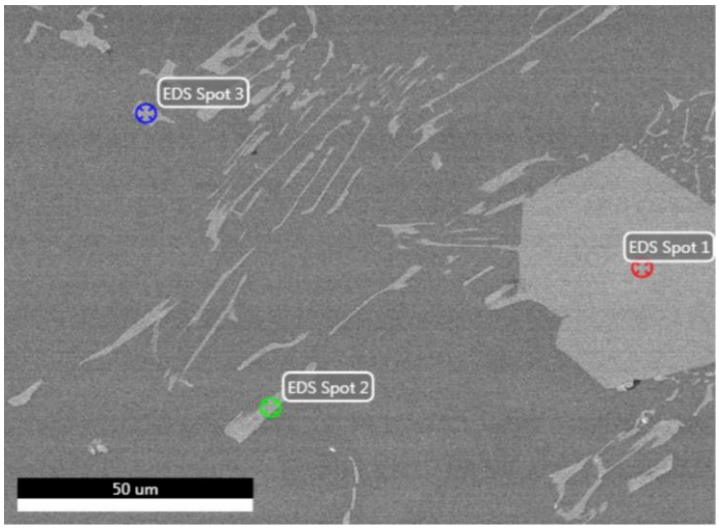

EDS spot 1:

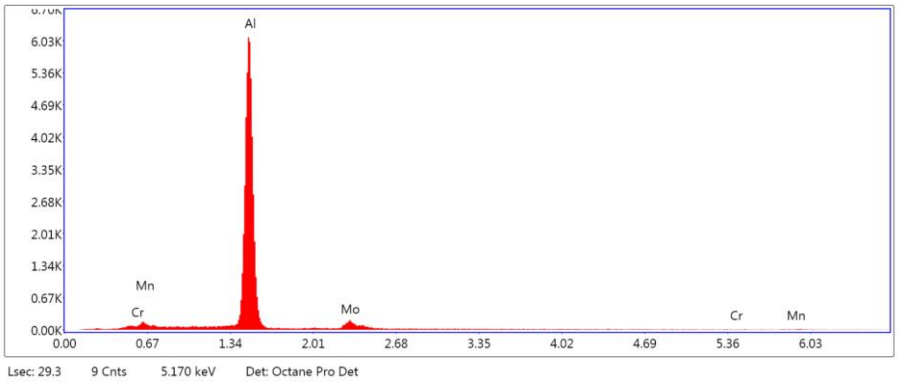

Element	Weight %	Atomic %	Error %
Al	88.29	95.82	2.88
Mo	9.13	2.79	12.04
Cr	0.61	0.34	72.48
Mn	1.97	1.05	67.31

EDS spot 2:

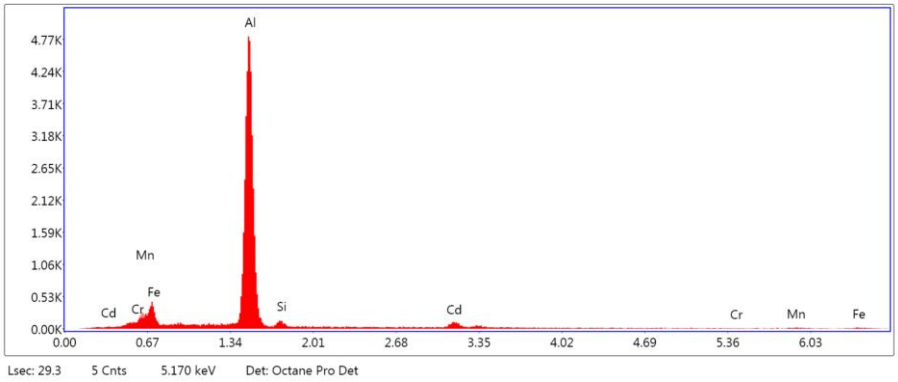

Element	Weight %	Atomic %	Error %
Fe	9.63	5.41	7.71
Al	75.00	87.22	3.60
Si	2.10	2.34	16.29
Cd	8.77	2.45	18.84
Cr	0.36	0.22	78.10
Mn	4.13	2.36	40.53

EDS spot 3:

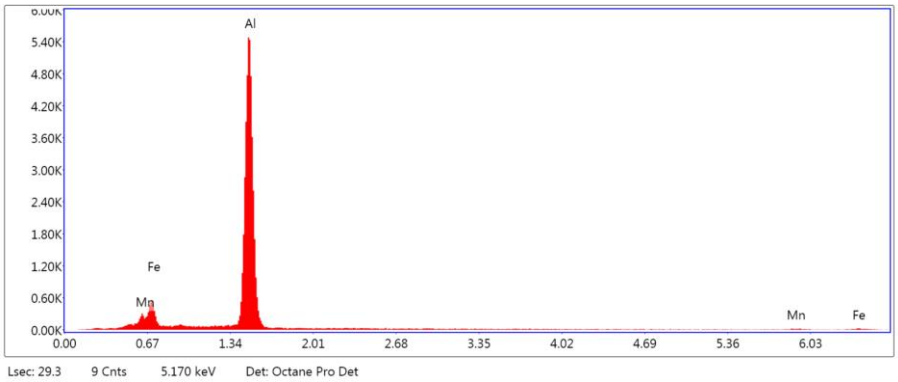

Element	Weight %	Atomic %	Error %
Fe	11.68	6.20	4.93
Al	82.50	90.66	3.37
Mn	5.81	3.14	30.29